INFRARED STARK AND ZEEMAN SPECTROSCOPY OF COMPLEXES FORMED FROM SEQUENTIAL CAPTURE IN HELIUM NANODROPLETS

by

JOSEPH BRICE

(Under the Direction of Gary E. Douberly)

ABSTRACT

Helium nanodroplet isolation is used to facilitate the formation of van der Waals complexes *in situ*. Complexes are interrogated with infrared Stark, and Zeeman spectroscopies. Complexes are formed from sequential capture of gas phase transient radicals and stable species. Transient radicals in these complexes are atomic oxygen, $O(^3P)$, or the hydroxyl radical, ·OH. The complexes form along the ground vibronic surface and are trapped in shallow wells due to barriers for reaction. The complex formed between $O(^3P)$ and HCN is exclusively hydrogen bound despite there being a small well on the potential in which a nitrogen bound isomer could exist. The complexes formed from the hydroxyl radical are OH-CO, and OH-C_2H_2, which have a linear and T-shaped geometry respectively. The large amplitude zero point motion of the OH-CO complex leads to a reduction in the measured dipole moment from Stark spectroscopy. Eighty percent of the reduction can be accounted for via vibrational averaging along the large amplitude motion. Zeeman Spectroscopy of the hydroxyl radical and its complexes exhibit phenomenon not well understood. The linear OH-CO was easily modeled through

a gas phase effective Hamiltonian, but both the OH radical and the OH-acetylene complex were perturbed significantly from gas phase predictions. As of yet, there is no theoretical understanding to which these perturbations can be attributed.

INDEX WORDS: Helium Nanodroplet Isolation, Infrared Spectroscopy, Stark Spectroscopy, Zeeman Spectroscopy, van der Waals Complexes, Pyrolysis, Hydroxyl Radical, Atomic Oxygen

INFRARED STARK AND ZEEMAN SPECTROSCOPY OF COMPLEXES FORMED FROM SEQUENTIAL CAPTURE IN HELIUM NANODROPLETS

by

JOSEPH BRICE

BS, University of West Florida, 2013

A Dissertation Submitted to the Graduate Faculty of The University of Georgia in Partial Fulfillment of the Requirements for the Degree

DOCTOR OF PHILOSOPHY

ATHENS, GEORGIA

2019

INFRARED STARK AND ZEEMAN SPECTROSCOPY OF COMPLEXES FORMED FROM SEQUENTIAL CAPTURE IN HELIUM NANODROPLETS

by

JOSEPH BRICE

Major Professor:	Gary E. Douberly
Committee:	Michael A. Duncan
	Melanie A. Reber

Electronic Version Approved:

Suzanne Barbour
Dean of the Graduate School
The University of Georgia
May 2019

ACKNOWLEDGEMENTS

First and foremost, I must thank my parents, Tom and Allison. Without you both, I would not have made it this far. Thank you for supporting, rooting, visiting and checking in on me now and then. You can't imagine how helpful it was to hear your voice and know that I could count on you through it all. Thank you.

To Gary: thank you for letting me loose in your lab. The space you gave me to learn and grow on my own was invaluable. My skills, critical thinking, and problem-solving abilities are a direct result of your tutelage and your passion for science. I am thankful that our personalities were compatible because it made my research and classes enjoyable and fruitful. So thanks for everything, dood.

To Melissa and Alaina: thanks for all of the birthday shenanigans, corn maze trips, Mexican nights, free cone days, and listening ears. Without you two, I definitely would have gone insane. Destressing conversations and the fun times made the journey easier and more enjoyable along the way.

To Peter: thanks for all the tea, and may your coffee be ever great.

To the rest of the Douberly Group: Grayg, Kale, Travis (and you too Ronald). Thanks for being so willing to endure my training and mentorship. Remember to keep your boss in line and get graduated!

To the Snark Trio/Quartet: lunch was always a much-needed relief. I looked forward to those days all week. (Still lookin' for that lemon in my water). To the Johnson

Ladies: thanks for the laughs! I seriously don't think anyone else could make me laugh quite as much as y'all managed to do. Thanks!

Ben, Josie, Hunter, Hayley, Liz and Vince: Thanks for all of the great tailgates, board games, D&D, and Fantasy Football fun. You guys reminded me how important it was to not sit cooped up in my lab all the time.

To the "Throuple," you know who you are. Thanks for giving me a reason to leave lab at a reasonable hour and for all of the lunch dates. Walking to Tate may not have been the best way to spend your time, but I certainly needed the companionship and you never complained (too loud).

To David and Michelle, thanks for getting our group together over board games. We started a tight-knit group of friends that first semester and now we're friends for life. We have you to thank for it! Also, thank you for being there for me, a concerned eye always ready to lend a hand or a helpful word of advice, even if it wasn't what I wanted to hear. You both care a lot about me, and I couldn't ask for more compassionate friends.

To Abby (That's right Tim, you're last and least.): I kid, I kid. Abby, thank you for all of the great wine and cheese time and family dinners! I can't wait to continue this tradition in Portland. Tim, I don't know how you managed to get your PhD on our group couch, but I am glad to be moving to Portland to enjoy the West with you and your family. Despite the blatant lies you spread about my life for your own amusement, I have grown fond of your company; therefore, I hereby declare that you are safe from my murderous rampage……at least for now.

TABLE OF CONTENTS

Page

CHAPTER 1

INTRODUCTION

1.1 Helium Droplets as a Spectroscopy Medium

In 1992, the Scoles group published[1] the first spectroscopic investigation utilizing helium droplet beams as a matrix. Although they improperly assigned the droplet-SF_6 interaction to have been on the surface, Fröchtenicht, Tonnies, and Vilesov[2] later reinvestigated SF_6 in helium droplets and found the rovibrational band structure that suggested the SF_6 was solvated inside the droplet. Since these seminal experiments, helium droplets have evolved to become an indispensable matrix for spectroscopy. They can be used to trap transient species that are otherwise hard to isolate;[3-7] they have been used to facilitate reactions *in situ*,[8-12] and can be used to investigate shallow wells along potential energy surfaces[13-19] *via* their ability to remove energy from solvated species.

In experiments with OCS as a dopant, Tonnies and Vilesov[20] highlighted one major benefit of ^{4}He droplets as a matrix: superfluidity. They showed that droplets of ^{3}He did not preserve the rotational fine structure of vibrational bands for solvated molecules. To further test this hypothesis, they doped a ^{3}He droplet with ^4He_n and an OCS molecule. Due to the higher zero-point energy of ^{3}He, they anticipated ^{4}He clustering around the OCS, and found that the rotational substructure of the vibrational transition began to return with as few as 60 ^{4}He atoms, motivating further that dopants have minimal interaction with the superfluid behavior of a ^{4}He droplet. ^{4}He droplets are not completely free of interaction with the dopant, however. In the SF_6 experiment,[2] the rotational profile

of the ν_3 vibrational band was fit to a model which required the reduction of the rotational constant by a factor of 3. This reduction was attributed to helium atoms rotating along with the solvated species, increasing the moment of inertia. Furthermore, this experiment provided an approximation for the temperature of the droplet environment of ~0.37 K. Although this is just a rotational temperature, it suggests that the droplet-dopant coupling is strong enough to facilitate the dissipation of the dopant's excess thermal energy and equilibrate to the droplet temperature.

1.2 Stabilizing Highly Reactive Species and Complexes

The dissipative nature of the ^{4}He droplet provides a useful way to stabilize highly reactive systems for interrogation. Thermal dissipation is often efficient enough to trap non-equilibrium complexes, such as the case with water clusters,[21] as well as "freeze out" populations of rotamers that correspond to higher temperature equilibria.[22-23] Furthermore, the weakly perturbing matrix environment allows highly reactive species, e.g. the OH radical, to live long enough to perform investigations of the electronic structure.

It has been estimated[24] that the thermal dissipation rate of a ^{4}He droplet is on the order of 10^{12} K/s, and further this value predicts a cooling timescale for dopants to be on the order of nanoseconds. Therefore, sequential doping of the droplet ensemble is expected to lead to interactions between dopants along the ground rovibronic surface. Unless the potential energy surface (PES) lacks a barrier to reaction, this rapid cooling serves to prevent reactions. If this part of the potential was repulsive, then one would expect the dopants to remain separated. However, if there is a potential energy well

before the barrier to reaction, then droplets could stabilize a prereactive complex. Also known as entrance channel complexes, these complexes are typically stabilized by van der Waals interactions. Helium droplets are especially suited to study such elusive complexes, as binding energies are typically very low, making it difficult to trap with other methods. With such low binding energies, the importance of such features of a potential energy surface are often questioned. However, there have been experiments that reinforce their importance.[25-26] In these cases, the van der Waals region of the potential modifies long range behavior that preferentially enhances some reaction channels over others such as through stabilized complexes which can tunnel to reaction. A further motivation to studying entrance channel complexes is a benchmark for theoretical pursuits. Indeed, the region dominated by long range interactions is difficult to model and predict, especially if the potential energy surface is particularly shallow, as is often the case.

1.3 Probing Fundamental Interactions

The equilibrium temperature of the droplet also provides a degree of control in the investigation of fundamental molecular interactions. At 0.4 K, very few rovibrational levels are populated. This simplifies the spectra collected, especially in the case of small molecules and complexes, as anharmonic resonances are less prevalent than in larger systems. The simple spectra provide a sensitive probe to the environment in which the system resides, as subtle changes in the geometric structure are more easily identifiable. These perturbations include the droplet environment itself. In measurements of the hydroxyl radical[3] in helium droplets, it was observed that the Λ-doubling increased

relative to the gas phase separation. It was rationalized as a solvation effect that depends on the parity of the solvated electronic state. Therefore, the nearly electronic degenerate states were further separated by their solvation energies in the helium bath. Both ground and excited (v=1) vibrational levels were affected, though the excited state was affected by a factor of two more.

Such fundamental interactions are of great interest as they improve understanding of the quantum mechanics at play in molecular interactions. Of particular interest to this work is the molecular Zeeman effect. The molecular Zeeman effect has been thoroughly studied in two broad classifications: diatomic molecules or radicals and closed shell molecules. There has been very little investigation on the molecular Zeeman effect in nonlinear radicals. The molecular Zeeman effect perturbs energy levels based on angular momentum-derived magnetic fields generated by the molecule or complex, which makes it especially suited to investigate electronic structure of van der Waals complexes. If a gas phase comparison exists within the literature, we have the added capability to investigate the extent that solvation affects such interactions.

In addition to the Zeeman effect, the Stark effect provides a useful probe of the electronic structure. The Stark effect facilitates the experimental determination of the equilibrium dipole moment of the molecule or complex, as Stark simulations are extremely sensitive to the value of the dipole moment in both the ground and excited vibrational states. The helium bath does not perturb these equilibrium dipole moments, as they tend to be within 5% of their gas phase values.[27] The dipole moments further serve as a benchmark for computational endeavors on these species.

The remainder of this dissertation will focus on the infrared investigations of small molecules and complexes doped into helium droplets, specifically the Stark and Zeeman effects in open shell species.

1.4 References

(1) Goyal, S.; Schutt, D. L.; Scoles, G., Vibrational Spectroscopy of Sulfur-Hexafluoride Attached to Helium Clusters. *Phys. Rev. Lett.* **1992**, *69*, 933-936

(2) Frochtenicht, R.; Toennies, J. P.; Vilesov, A., High-Resolution Infrared-Spectroscopy of SF_6 Embedded in He Clusters. *Chem. Phys. Lett.* **1994**, *229*, 1-7

(3) Raston, P. L.; Liang, T.; Douberly, G. E., Anomalous Lambda-Doubling in the Infrared Spectrum of the Hydroxyl Radical in Helium Nanodroplets. *J. Phys. Chem. A* **2013**, *117*, 8103-8110

(4) Leavitt, C. M.; Moradi, C. P.; Stanton, J. F.; Douberly, G. E., Communication: Helium Nanodroplet Isolation and Rovibrational Spectroscopy of Hydroxymethylene. *J. Chem. Phys.* **2014**, *140*, 4171102.

(5) Raston, P. L.; Liang, T.; Douberly, G. E., Observation of the Q(3/2) Lambda-Doublet Transitions for $X^2\prod_{3/2}$ OD in Helium Nanodroplets. *Mol. Phys.* **2014**, *112*, 301-303

(6) Broderick, B. M.; McCaslin, L.; Moradi, C. P.; Stanton, J. F.; Douberly, G. E., Reactive Intermediates in ^{4}He Nanodroplets: Infrared Laser Stark Spectroscopy of Dihydroxycarbene. *J. Chem. Phys.* **2015**, *142*, 144309

(7) Broderick, B. M.; Moradi, C. P.; Douberly, G. E., Infrared Laser Stark Spectroscopy of Hydroxymethoxycarbene in ^{4}He Nanodroplets. *Chem. Phys. Lett.* **2015**, *639*, 99-104

(8) Morrison, A. M.; Agarwal, J.; Schaefer, H. F., 3rd; Douberly, G. E., Infrared Laser Spectroscopy of the CH_3OO Radical Formed from the Reaction of CH_3 and O_2 within a Helium Nanodroplet. *J. Phys. Chem. A* **2012**, *116*, 5299

(9) Raston, P. L.; Liang, T.; Douberly, G. E., Infrared Spectroscopy of HOOO and DOOO in ^{4}He Nanodroplets. *J. Chem. Phys.* **2012**, *137*, 184302

(10) Leavitt, C. M.; Moradi, C. P.; Acrey, B. W.; Douberly, G. E., Infrared Laser Spectroscopy of the Helium-Solvated Allyl and Allyl Peroxy Radicals. *J. Chem. Phys.* **2013**, *139*, 234301

(11) Moradi, C. P.; Morrison, A. M.; Klippenstein, S. J.; Goldsmith, C. F.; Douberly, G. E., Propargyl + O_2 Reaction in Helium Droplets: Entrance Channel Barrier or Not? *J. Phys. Chem. A* **2013**, *117*, 13626

(12) Liang, T.; Douberly, G. E., On the Al + HCN Reaction in Helium Nanodroplets. *Chem. Phys. Lett.* **2012**, *551*, 54-59

(13) Douberly, G. E.; Raston, P. L.; Liang, T.; Marshall, M. D., Infrared Rovibrational Spectroscopy of OH-C_2H_2 in ^{4}He Nanodroplets: Parity Splitting Due to Partially Quenched Electronic Angular Momentum. *J. Chem. Phys.* **2015**, *142*, 134306

(14) Hernandez, F. J.; Brice, J. T.; Leavitt, C. M.; Liang, T.; Raston, P. L.; Pino, G. A.; Douberly, G. E., Mid-Infrared Signatures of Hydroxyl Containing Water Clusters: Infrared Laser Stark Spectroscopy of OH-H_2O and OH-$(D_2O)_n$ (n=1-3). *J. Chem. Phys.* **2015**, *143*164304.

(15) Hernandez, F. J.; Brice, J. T.; Leavitt, C. M.; Pino, G. A.; Douberly, G. E., Infrared Spectroscopy of OH•••CH_3OH: Hydrogen-Bonded Intermediate along the Hydrogen Abstraction Reaction Path. *J. Phys. Chem. A* **2015**, *119*, 8125-8132

(16) Moradi, C. P.; Douberly, G. E., Infrared Laser Spectroscopy of the L-Shaped Cl-HCl Complex Formed in Superfluid ^{4}He Nanodroplets. *J. Phys. Chem. A* **2015**, *119*, 12028-12035

(17) Brice, J. T.; Liang, T.; Raston, P. L.; McCoy, A. B.; Douberly, G. E., Infrared Stark and Zeeman Spectroscopy of OH-CO: The Entrance Channel Complex along the OH + CO → *trans*-HOCO Reaction Pathway. *J. Chem. Phys.* **2016**, *145*, 10124310.

(18) Moradi, C. P.; Xie, C. J.; Kaufmann, M.; Guo, H.; Douberly, G. E., Two-Center Three-Electron Bonding in $ClNH_3$ Revealed *via* Helium Droplet Infrared Laser Stark Spectroscopy: Entrance Channel Complex along the Cl + NH_3 → $ClNH_2$ + H Reaction. *J. Chem. Phys.* **2016**, *144*, 8164301.

(19) Brice, J. T.; Franke, P. R.; Douberly, G. E., Sequential Capture of O(^{3}P) and HCN by Helium Nanodroplets: Infrared Spectroscopy and *ab Initio* Computations of the $^3\sum$ O-HCN Complex. *J. Phys. Chem. A* **2017**, *121*, 9466-9473

(20) Grebenev, S.; Toennies, J. P.; Vilesov, A. F., Superfluidity within a Small ^{4}He Cluster: The Microscopic Andronikashvili Experiment. *Science* **1998**, *279*, 2083-2086

(21) Douberly, G. E.; Miller, R. E.; Xantheas, S. S., Formation of Exotic Networks of Water Clusters in Helium Droplets Facilitated by the Presence of Neon Atoms. *J. Am. Chem. Soc.* **2017**, *139*, 4152-4156

(22) Leavitt, C. M.; Moore, K. B.; Raston, P. L.; Agarwal, J.; Moody, G. H.; Shirley, C. C.; Schaefer, H. F.; Douberly, G. E., Liquid Hot NAGMA Cooled to 0.4 K: Benchmark Thermochemistry of a Gas-Phase Peptide. *J. Phys. Chem. A* **2014**, *118*, 9692-9700

(23) Franke, P. R.; Douberly, G. E., Rotamers of Isoprene: Infrared Spectroscopy in Helium Droplets and *Ab Initio* Thermochemistry. *J. Phys. Chem. A* **2018**, *122*, 148-158

(24) Scheidemann, A.; Schilling, B.; Toennies, J. P., Anomalies in the Reactions of He^+ with SF_6 Embedded in Large ^{4}He Clusters. *J. Phys. Chem.* **1993**, *97*, 2128-2138

(25) Skouteris, D.; Manolopoulos, D. E.; Bian, W. S.; Werner, H. J.; Lai, L. H.; Liu, K. P., van der Waals Interactions in the Cl+HD Reaction. *Science* **1999**, *286*, 1713-1716

(26) Nguyen, T. L.; Xue, B. C.; Weston, R. E.; Barker, J. R.; Stanton, J. F., Reaction of HO with CO: Tunneling Is Indeed Important. *J. Phys. Chem. Lett.* **2012**, *3*, 1549-1553

(27) Stiles, P. L.; Nauta, K.; Miller, R. E., Dipole Moments of Molecules Solvated in Helium Nanodroplets. *Phys. Rev. Lett.* **2003**, *90*, 4135301.

CHAPTER 2

EXPERIMENTAL METHODS

2.1 Helium Nanodroplet Formation and Instrumental Consideration

A rendering of the helium nanodroplet instrument is reproduced in Figure 2.1. The apparatus comprises three main regions: droplet formation, droplet doping, and detection. In the droplet formation region, helium gas thermally sunk to a cryostat is allowed to expand into vacuum through a pinhole nozzle. In the droplet doping region, molecular species are introduced to the droplet ensemble via gas phase collisions. Finally, in the detection region, droplets are ionized and resultant ions are analyzed with a quadrupole mass spectrometer.

Droplet formation can proceed either through homogeneous nucleation or through liquid droplet fragmentation depending on the conditions of the expansion.[1-2] Liquid fragmentation refers to a liquid jet of helium that fragments into droplets after exiting the nozzle, whereas homogeneous nucleation is a gaseous aggregation mechanism involving sufficient three-body collisions to facilitate coalescence of the helium into droplets. Temperature of the nozzle, stagnation pressure behind the orifice, and orifice diameter determine not only the type of formation mechanism, but also the size distribution of the droplets produced.[3] Practically, temperature and stagnation pressure are the only feasible adjustable parameters to influence the droplet size distribution. The experiments presented herein were performed within the homogeneous nucleation regime of

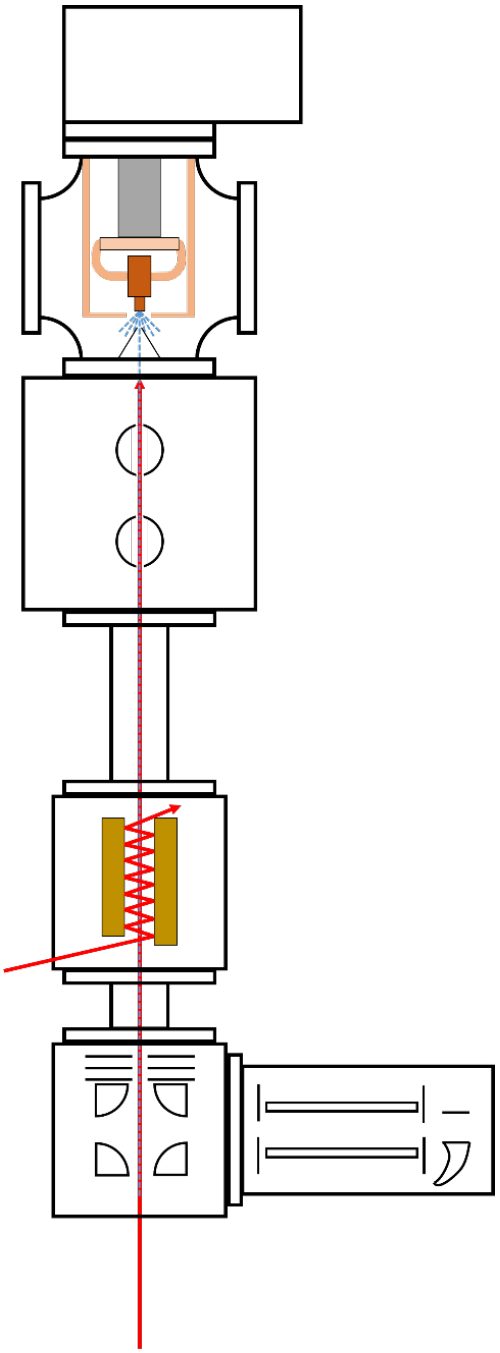

Figure 2.1: The experimental apparatus used in the current work. From top to bottom: helium cryostat, expansion chamber, doping chamber, Stark/Zeeman chamber, quadrupole mass spectrometer. The droplet beam is visualized by a dashed light blue line. The red lines represent the two arrangements for laser irradiation. Collinear travels from right to left counter-propagating to the beam, and multipass arrangement is through the Stark/Zeeman chamber.

droplet formation and a 5 μm nozzle. The droplet size distribution for the nucleation mechanism can be modeled using a log-normal distribution according to the following equation:

$$P(N) = \frac{1}{N\sigma\sqrt{2\pi}} e^{-\frac{(\ln N - \bar{N})^2}{2\sigma^2}}, \quad (2.1)$$

where $\bar{N}$ is the average and σ is the standard deviation of the natural logarithm distribution.[4]

Droplet formation dies off rapidly as the gas moves away from the nozzle. The droplets experience no further collisions after traveling on the order of 10^3 times the nozzle diameter and begin to evaporatively cool to a final temperature around 0.4 K. The droplets formed are skimmed into a beam using a 400 μm skimmer.

After passing through the skimmer, droplets enter the doping region, which is comprised of "pick-up cells." These are areas in the vacuum system where the local pressure is raised with the species of interest in the gas phase, facilitating collisions with the droplets. Collisions typically result in solvation of the species, and it is rapidly equilibrated to the droplet temperature. The collision frequency is statistical; that is, it is dependent on the physical cross section of the droplets, the partial pressure of the species, and the length of the gas-droplet beam interaction space. The statistical nature of the doping process can be modeled using a Poisson distribution[5]

$$P(n) = \frac{(\rho\sigma L)^n}{n!} e^{-\rho\sigma L}, \quad (2.2)$$

where n is the average number of dopants per droplet, ρ is the number density of the dopant, σ is the cross section of the droplet, and L is the distance over which the droplet encounters the dopant vapor. Because pick-up is statistical, each pick-up event is

independent of any previous pick up events, and thus it is true, on average, that the partial pressure which optimizes the doping of one dopant per droplet can be doubled to obtain the pressure that will optimize the doping of a second dopant per droplet. In addition, multiple pick-up cells can be used to dope a single droplet with two different dopants, which affords the ability to study complex formation and reactions.

After the doping process is complete, the droplets are irradiated with the tunable idler output of a continuous wave Aculight Argos optical parametric oscillator (OPO). There are two OPO cavities that together provide tunable infrared light from 2500 to 4000 cm^{-1} at greater than 1 W of idler output.[6] There are two configurations for the laser droplet interaction region: collinear and multipass. In the collinear mode, light is focused into the apparatus coaxially and antiparallel to the droplet beam. This provides the most droplet beam-laser overlap. The alternative multipass arrangement involves two 15 cm plane mirrors which allow the beam to make approximately 20 to 30 passes over the 15cm. This arrangement is a fairly small interaction length, and as such signals will be diminished from their collinear counterparts. However, the benefit to the multipass arrangement is the ability to confine the entire laser-droplet interaction region entirely within an electric or magnetic field, facilitating the collection of Stark and Zeeman spectra.

Finally, the droplet beam enters the quadrupole mass spectrometer (QMS) chamber. The droplet beam is detected by electron ionization of the helium bath. The ionization of the helium droplet generates a He^+ within the droplet. Because of the bulk nature of the droplet, the hole can begin to move within the droplet. In the case of a dopant-free droplet, the movement of the hole stops as He_2^+ is formed from the droplet.

The formation of the dimer cation releases a significant amount of energy, which subsequently evaporates the rest of the droplet. This phenomenon manifests itself in the mass spectrometer as a progression of He_n^+ peaks. If, however, the droplet contains an impurity, the moving hole abstracts an electron from the dopant, given that the ionization potential difference between most organic molecules and He is around 12 to 15 eV. The charge transfer ionization process generates an impurity cation with the excess energy in excited internal degrees of freedom, which quickly evaporates the rest of the droplet. The bare ion is then detected by the mass spectrometer.

The method of collecting spectra is a type of action spectroscopy that relies upon the dependence of the ionization/detection scheme on the physical droplet cross section of a helium droplet. Upon vibrational excitation of a dopant within a droplet, the energy is coupled to the droplet modes and subsequent helium atom evaporation from the surface of the droplet removes excess energy. A single evaporating helium atom carries with it approximately 5 cm^{-1}.[7] Thus, the removal of energy from a 3000 cm^{-1} photon will require the evaporation of ~600 helium atoms. Evaporation reduces the cross section of the droplet and lowers the probability of ionization and its subsequent detection in the QMS. Any signal in the mass spectrometer that derives from the charge transfer ionization (and possible post-ionization fragmentation) of a dopant will have its intensity reduced when the laser is on resonance with a transition of the dopant. Thus, when the QMS is set to pass a specific mass-to-charge ratio, and the laser is modulated mechanically with a chopper, the current on the detector in the QMS will oscillate at the chopper frequency. The oscillating signal is processed *via* a lock-in amplifier using a reference signal from

the chopper. A spectrum is collected by monitoring the amplitude of the lock-in signal as a function of idler frequency.

2.2 Radical Generation

Two methods were used to generate radicals for the experiments detailed in subsequent chapters. The first source generates the hydroxyl radical from the pyrolytic decomposition of *tert*-butyl hydroperoxide. The second source generates oxygen atoms from molecular oxygen using thermal catalytic dissociation.

Hydroxyl radicals are formed using a quartz pyrolysis source.[8] The source consists of water cooled electrodes, which are connected through a Ta/W filament which is coiled around the tip of a 0.25 in. quartz tube with 0.125 in. inner diameter. Wall power, 120 VAC, is modulated by a Variac and then through a 10:1 step-down transformer to increase the current supplied to the filament. Typically operated between 20 and 40 A of current, the filament resistively heats the quartz tube, and collisions of the pyrolysis precursor with the tube walls results in decomposition of the precursor into the desired product and any pyrolytic contaminants. In the case of the hydroxyl radical, the precursor *tert*-butyl hydroperoxide decomposes according to the following chemical equation

$$(CH_3)_3COOH \overset{\Delta}{\Rightarrow} (CH_3)_2CO + \cdot CH_3 + \cdot OH$$

The end of the quartz tube is then oriented perpendicular to the droplet beam path so as to limit the length of the pyrolytic product droplet interaction. Due to the low effusive pressure of the precursor flow, it is expected that pyrolytic products will not likely collide

with one another to form secondary pyrolysis products. Though not specifically investigated, this assumption seems to be valid based on empirical evidence.

The thermal catalytic cracker is a commercial product from Mantis Sigma Ltd. The MGC-75 consists of an iridium tube secured in a molybdenum collar. The collar is sunk thermally to a beryllium oxide insulator which in turn is in thermal contact with a water cooled copper base. The BeO insulator allows the biasing of the tube to 2 kV while still allowing significant heat conduction from the collar to the copper base. Set into a copper shield that has been secured to the water cooled base, filaments are operated between 3.5 and 4.5 A. The extraction potential generated by biasing the iridium tube attracts electrons to the tube. The resultant electron bombardment heats up the iridium tube, and when molecular oxygen collides with the inner walls, it is catalytically dissociated into atomic oxygen, $O(^3P)$. When operating at peak efficiency, the iridium tube sources approximately 50 mA, which gives a "power" reading of 100 W. The efficiency of molecular oxygen dissociation is estimated at 60% through mass spectrometer ion yield, though no direct measurement has been performed. The resulting droplet beam doping efficiency, assuming optimal single doping conditions, is 25%.[9-10] A 3D CAD image of the thermal gas cracker can be seen in Figure 2.2.

2.3 Stark and Zeeman Cells

In the laser interaction region of the apparatus, the Stark cell is a removable set of stainless steel electrodes suspended between the gold plane mirrors of the laser multipass arrangement. These electrodes are separated by 3.10(4) mm and one electrode is typically

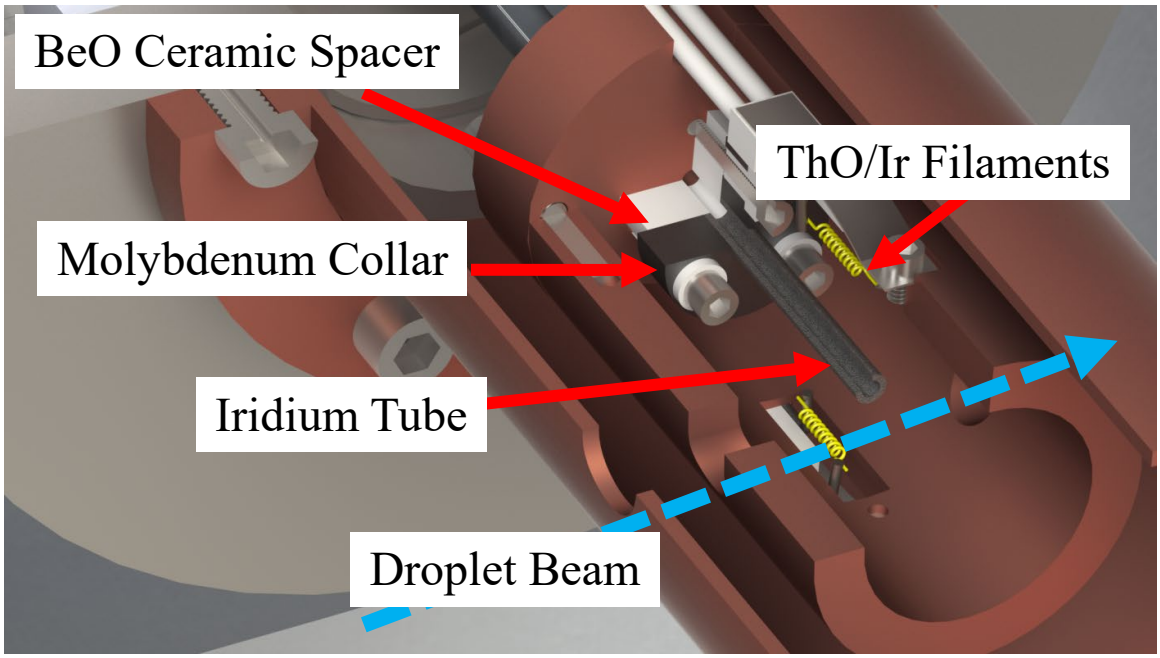

Figure 2.2: The Mantis Sigma Ltd. MGC-75 thermal gas cracker. The cutaway view visualizes the important components discussed in the text.

biased between 0 and 10 kV, giving field strengths up to about 30 kV/cm. Further information about the stark cell can be found in Ref. 8.

The Zeeman cell was assembled from two commercially available 1 T Nd rare-earth magnets. These two magnets are connected together with a steel frame to improve the strength and homogeneity of the field between the two magnetic faces. The faces are separated by 0.5 in. This was designed to provide 0.5 T field strength in the center of the two magnet faces. A commercial Hall probe was used to calibrate the field strength. Averaging several measurements conducted by multiple persons to remove measurement bias, the field strength was measured to be 0.425(2) T. The value was later corroborated from spectroscopic measurements and a theoretical simulation program written in LabVIEW.

2.4 References

(1) Jiang, T.; Northby, J. A., Fragmentation Clusters Formed in Supercritical Expansions of ^{4}He. *Phys. Rev. Lett.* **1992**, *68*, 2620-2623

(2) Knuth, E. L.; Henne, U., Average Size and Size Distribution of Large Droplets Produced in a Free-Jet Expansion of a Liquid. *J. Chem. Phys.* **1999**, *110*, 2664-2668

(3) Northby, J. A., Experimental Studies of Helium Droplets. *J. Chem. Phys.* **2001**, *115*, 10065-10077

(4) Harms, J.; Toennies, J. P.; Knuth, E. L., Droplets Formed in Helium Free-Jet Expansions from States Near the Critical Point. *J. Chem. Phys.* **1997**, *106*, 3348-3357

(5) Choi, M. Y.; Douberly, G. E.; Falconer, T. M.; Lewis, W. K.; Lindsay, C. M.; Merritt, J. M.; Stiles, P. L.; Miller, R. E., Infrared Spectroscopy of Helium Nanodroplets: Novel Methods for Physics and Chemistry. *Int. Rev. Phys. Chem.* **2006**, *25*, 15-75

(6) Morrison, A. M.; Liang, T.; Douberly, G. E., Automation of an "Aculight" Continuous-Wave Optical Parametric Oscillator. *Rev. Sci. Instrum.* **2013**, *84*, 013102.

(7) Brink, D. M.; Stringari, S., Density of States and Evaporation Rate of Helium Clusters. *Z. Phys. D: At., Mol. Clusters* **1990**, *15*, 257-263

(8) Raston, P. L.; Liang, T.; Douberly, G. E., Anomalous Lambda-Doubling in the Infrared Spectrum of the Hydroxyl Radical in Helium Nanodroplets. *J. Phys. Chem. A* **2013**, *117*, 8103-8110

(9) Brice, J. T.; Franke, P. R.; Douberly, G. E., Sequential Capture of $O(^3P)$ and HCN by Helium Nanodroplets: Infrared Spectroscopy and *ab Initio* Computations of the $^3\sum$ O-HCN Complex. *J. Phys. Chem. A* **2017**, *121*, 9466-9473

(10) Stiles, P. L.; Nauta, K.; Miller, R. E., Dipole Moments of Molecules Solvated in Helium Nanodroplets. *Phys. Rev. Lett.* **2003**, *90*, 4, 135301.

CHAPTER 3

SEQUENTIAL CAPTURE OF O(^{3}P) AND HCN BY HELIUM NANODROPLETS: INFRARED SPECTROSCOPY AND *AB INITIO* COMPUTATIONS OF THE $^3\sum$ O–HCN COMPLEX

Catalytic thermal cracking of O_2 is employed to dope helium droplets with O(^{3}P) atoms. Mass spectrometry of the doped droplet beam reveals an O_2 dissociation efficiency larger than 60%; approximately 26% of the droplet ensemble is doped with single oxygen atoms. Sequential capture of O(^{3}P) and HCN leads to the production of a hydrogen-bound O−HCN complex in a $^3\Sigma$ electronic state, as determined *via* comparisons of experimental and theoretical rovibrational Stark spectroscopy. *Ab initio* computations of the three lowest lying intermolecular potential energy surfaces reveal two isomers, the hydrogen-bound ($^3\Sigma$) O−HCN complex and a nitrogen-bound ($^3\Pi$) HCN−O complex, lying 323 cm^{-1} higher in energy. The HCN−O to O−HCN interconversion barrier is predicted to be 42 cm^{-1}. Consistent with this relatively small interconversion barrier, there is no experimental evidence for the production of the nitrogen-bound species upon sequential capture of O(^{3}P) and HCN.

3.1 Introduction

Reactions involving atomic oxygen are ubiquitous in both terrestrial combustion environments[1] and in the chemistry of the interstellar medium.[2,3] For example, O(^{3}P)

electrophilic addition initiates the consumption of acetylene in flames.[1, 4-5] However, reaction intermediates of $O(^3P) + C_mH_n$ chemistry have not been characterized spectroscopically, owing to the difficulty associated with producing large abundances of these species. In this report, the weakly bound, $^3\Sigma$, O–HCN complex is characterized with infrared (IR) laser Stark spectroscopy. The complexation between $O(^3P)$ and HCN occurs following the sequential capture of reactants by nanoscopic liquid helium droplets. The results presented herein demonstrate the feasibility for spectroscopic studies that probe either pre-reactive complexes or reaction intermediates of $O(^3P) + C_mH_n$ reactions carried out *within* the dissipative environment of a helium nanodroplet.[6,7]

$O(^3P)$ + HCN is of significance to combustion chemistry.[8] HCN is a critical intermediate in the combustion of nitrogen-containing fuels,[9] and it is consumed primarily *via* its reaction with $O(^3P)$. The reaction has two exothermic channels and one endothermic hydrogen-abstraction channel, which is regarded as being accessible above 1500 K.[10] The primary exothermic pathway involves $O(^3P)$ addition to the C-N π-system, which leads to the production of an H atom and the NCO radical.[8, 10-12] However, the barrier to insertion is predicted to be ~10 kcal/mol,[11] and it is unlikely that it can be overcome when $O(^3P)$ and HCN combine within a 0.4 K helium nanodroplet. Instead, it is expected that energy dissipation *via* He atom evaporation will produce a long-range O−HCN complex stabilized by electrostatic interactions.

In a solid-Argon matrix isolation study, in which ozone was photolyzed in the presence of HCN, Mielke and Andrews[13] attributed a feature at 3263.3 cm^{-1} to the CH stretch vibration of a "weakly bound O–HCN complex". The spectral assignment was based on the band's disappearance upon matrix annealing; however, the structure of this

postulated species was not discussed. The helium droplet spectrum reported herein contains a band centered at 3285.89 cm^{-1}, and *via* an analysis of rotational fine structure and comparison to *ab initio* computations, this band is assigned to the linear, $^3\Sigma$, O–HCN species. In addition to this spectroscopy, we present a detailed non-relativistic *ab initio* characterization of the long-range O(^{3}P) + HCN interaction potential.

3.2 Experimental Methods

The helium nanodroplet apparatus has been described in detail previously,[14] thus only a discussion of relevant modifications related to the oxygen atom source and important experimental parameters is given here. Helium nanodroplets are continuously generated from the supersonic expansion of helium through a 5 μm diameter nozzle (15 K, 35 bar). The droplet expansion is skimmed into a beam using a 400 μm skimmer cone. The beam passes into a second differentially pumped chamber that contains separate sources for doping droplets with either O(^{3}P) or HCN. A molecule (or atom) of interest is introduced to a droplet *via* a statistical "pick-up" process.[7] Given the number densities of the species contained in these pick-up cells (PUC), Poisson statistics can be used to estimate the composition of the doped droplet beam.[15]

HCN is added to a differentially pumped PUC, isolated from the oxygen atom source, and the pressure is optimized for the production of droplets doped with single HCN molecules. Downstream from the HCN source, O(^{3}P) atoms are generated from a commercially available molecular gas cracker (MGC-75, Mantis-Sigma Ltd). The MGC is comprised of an iridium tube held at positive high voltage, which is heated through electron bombardment generated by hot filament emission. Molecular collisions with the

hot iridium tube catalytically dissociate the O_2 gas passing through it. The O_2 pressure within the Iridium tube is approximately 10^{-6} Torr. The cracker is situated in the instrument such that the droplet beam passes very close to the opening of the iridium tube. Power is the quantity used to experimentally optimize O_2 dissociation. It is a measure of the current collected on the iridium tube, thus it is related to the temperature of the tube (~1500 K at the highest powers, according to vendor specifications).

Upon pick-up, the dopant/helium internal degrees of freedom are brought into equilibrium at 0.4 K *via* the thermal evaporation of He atoms. Each evaporating He atom removes ~0.014 kcal/mol (5 cm^{-1});[16] therefore, the droplets used here (4000-6000 atoms) are capable of dissipating ~75 kcal/mol of internal energy, which is sufficient to remove both the internal energy of the "reactants" and the complexation energy associated with O–HCN production.

Ancilotto *et al.*[17] proposed a dimensionless parameter that we use to assess the solvation state of a captured O(^{3}P) atom. The *Ancilotto Parameter* (λ) is a measure of the ratio of dopant−helium attraction to the energy cost associated with forming a helium surface upon solute solvation. It has been shown that a λ value greater than about 1.9 is necessary for solvation.[17] From computations of the He−O(^{3}P) potentials (see Figure A3.1 in the appendix), we find Ancilotto parameters of $\lambda = 6.5$ and $\lambda = 3.4$ for Σ and Π potentials, respectively. Accordingly, we expect captured O(^{3}P) atoms to become solvated and reside, on average, *inside* the helium droplets, as opposed to being located on the surface.

Detection of molecules or complexes trapped within helium droplets is achieved through electron impact ionization and quadrupole mass spectrometry.[18] A continuous

wave, narrow linewidth (< 10 MHz) optical parametric oscillator is used to vibrationally excite the helium-solvated O–HCN complex.[19] Vibrational excitation is followed by energy transfer to the droplet, leading to the evaporation of ~650 He atoms. Evaporation reduces both the droplet's geometric and ionization cross section, which manifests as a depletion in the ion current detected by the mass spectrometer. By mechanically chopping the laser (80 Hz) and processing the mass spectrometer signal using a lock-in amplifier, an IR spectrum is generated as a background free depletion spectrum. Moreover, the recorded spectrum is made quasi-species-selective through a judicious choice of mass channel on which the depletion is detected.[20] The laser is overlapped with the droplet beam in either a collinear, counter-propagating configuration (for survey spectra) or in a two-mirror multipass arrangement (for Stark spectra); in the multipass configuration, the laser-droplet interaction region is confined within the electrodes of a Stark cell. Electric fields in the Stark cell are calibrated *via* measurements of the Stark spectrum of HCN.[21]

3.3 Theoretical Methods

Minimum energy structures for OHCN complexes were optimized at the CCSD(T)/ANO1 level of theory with subsequent harmonic frequency computations at the same level of theory using the CFOUR computational package.[22-27] The potential energy surface was computed with NEVPT2, as implemented in ORCA 4.0.[28] The reference wavefunctions were CASSCF[29-31] having 8 electrons in 7 orbitals. The active space orbitals were the three 2p orbitals of oxygen and the doubly-degenerate HOMO and LUMO orbitals of HCN. The CASSCF orbitals were averaged[32] over the lowest three

triplet electronic states. State-averaging allows for a more streamlined computation of the specific electronic states. The internal coordinates of HCN were constrained to those of the NEVPT2(4,4)/aug-cc-pVTZ[33-38] optimized structure. The effect of geometry relaxation was investigated, but it was deemed to be insignificant for this system.

3.4 Results and Discussion

3.4.1 Mass Spectrometry and Thermal Gas Dissociation

Figure 3.1 shows mass spectra of an HCN/O_2-doped droplet beam for various gas cracker powers (CP). The peaks observed every 4 u are due to the well-known $(He)_n^+$ distribution associated with the ionization of neat helium droplets.[39] The peaks observed at 27 u (HCN^+) and 28 u ($HCNH^+$) are due to droplets containing either HCN or $(HCN)_2$, respectively.[6] Ionization of helium-solvated HCN occurs *via* the $He^+ + HCN \rightarrow He + HCN^+$ charge transfer mechanism, as the probability for direct HCN ionization by electron impact is far lower than the probability for ionizing the helium droplet.

The largest change observed in the mass spectrum upon O_2 doping is an increase in m/z = 32 u, along with small increases on some of the weaker channels. For example, an increase on channel 29 u (HCO^+) is found (*vide infra*) to be due to droplets containing both HCN and O_2. Ionization of droplets containing O_2−HCN complexes leads to nascent $OOHCN^+$ ions having ~14 eV of internal energy, which is derived from the ionization energy difference between the molecular complex and liquid helium. Fragmentation of the nascent molecular ion apparently leads to the production of HCO^+ (among other ions), which is desolvated/ejected into the gas phase and detected with the mass spectrometer.

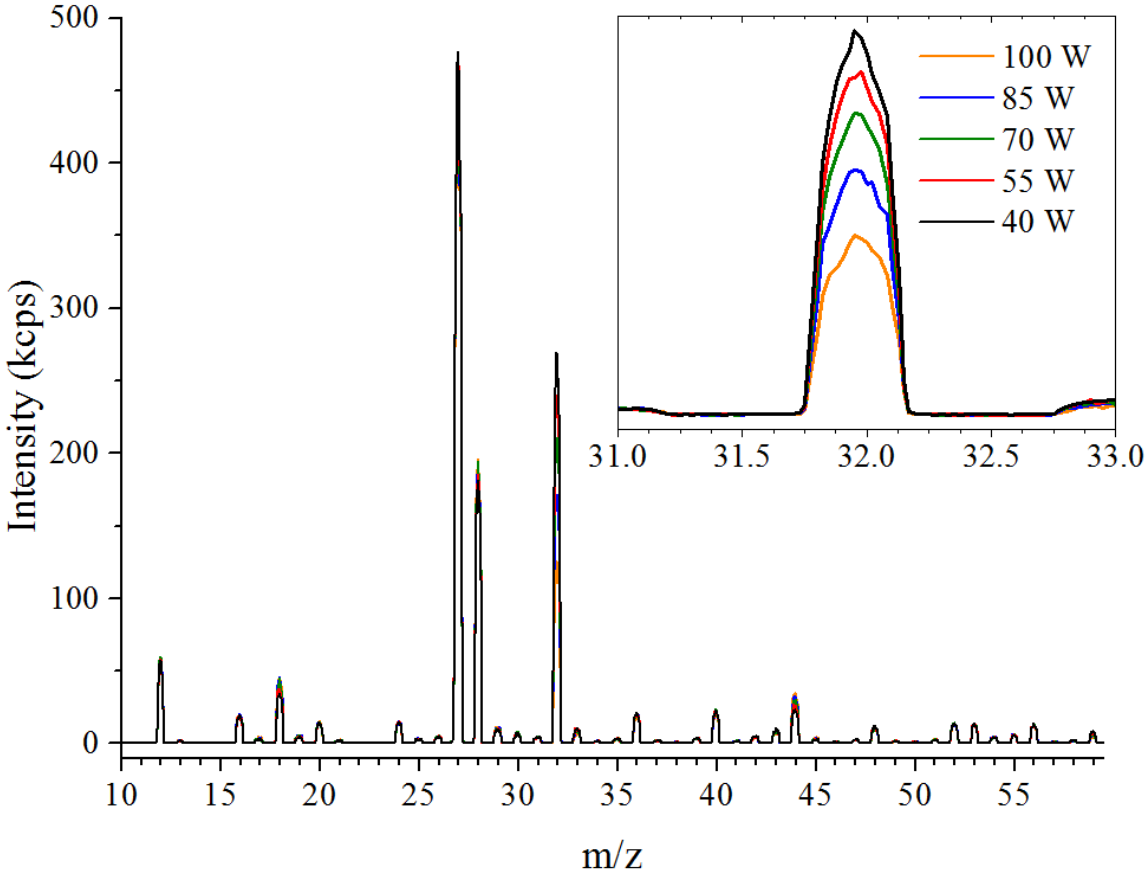

Figure 3.1: Overlaid mass spectra taken with experimental conditions optimized to dope droplets with one HCN and one O_2 molecule. Peaks at 27 and 32 u are HCN^+ and O_2^+, respectively. Inset enlarges m/z = 32 u, which shows the dependence of the ion signal on molecular gas cracker power (Watts).

Upon turning the MGC to about CP = 40 W, no change is observed in the mass spectrum. As the CP increases beyond 40 W, ion signal at mass 32 u decreases, and integrated ion signals indicate that O_2 dissociation can be made to be over 60% efficient (CP = 100 W). Signals in mass channels 18, 28, and 44 u increase by ~10% in going from 40 W to 100 W, presumably due to baking of H_2O, CO, and CO_2 from the iridium tube and gas-cracker assembly.

We note that a significant change with increasing CP is not observed on mass channel 16 u. We postulated that this could be due to the production of $^{16}O^+(He)_n$ ions, the distribution of which is mass-coincident with $(He)^+_{n+4}$ cluster ions. Helium-solvated atomic ion distributions, $Atom^+(He)_n$, have been observed in previous electron ionization measurements of atom-doped helium droplets, *e.g.* for Al-[14], Ne-[40], and Ar-doped[41] droplets. We measured similar mass spectra using $^{17}O_2$ in the MGC, and again we found no evidence for atomic oxygen ions or a distribution of $^{17}O^+(He)_n$ ions. The cross-section for $He^+ + O \rightarrow He + O^+$ charge transfer ionization in the gas phase is on the order of 10^{-14} $cm^3\ s^{-1}$ (*i.e.* five orders of magnitude slower than the typical Langevin rate).[42] As discussed in detail below, we have convincing spectroscopic evidence that we are producing $O(^3P)$-doped helium droplets, and therefore we are left to conclude from the mass spectrometry results that, for droplets containing only $O(^3P)$ atoms, $He^+ + O \rightarrow He + O^+$ charge transfer cannot compete with the production of neat helium cluster ions $(He)_n^+$.[40,41,43]

On the basis of the observed 60% O_2 dissociation at CP = 100W, we can use the well-known Poisson capture statistics[15] to estimate the composition of the droplet beam with the HCN pressure set to zero. Under these conditions, we estimate that 26% of the

droplet ensemble is doped with single oxygen atoms; approximately 8% of the beam is doped with O_2, and the remaining droplets are either devoid of dopants (42%) or are doped with more than one species (24%), *i.e.* with either $(O_2)_2$, $O–O_2$, or $(O)_2$, where the latter two pick-up events likely lead to reaction and dissipation of the entire droplet. We benefit from the fact that O_2 dissociation produces *two* oxygen atoms. Indeed, the estimated $O(^3P)$ doping fraction is substantially larger than what we obtain with pyrolysis sources designed to dope droplets with molecular radicals, for which doping fractions are typically less than 10%, given the available organic precursors.[44] By optimizing the pressure of HCN, 34% of all droplets are doped with single HCN molecules; therefore, under optimal conditions, ~9% of droplets capture both one $O(^3P)$ atom and one HCN molecule.

3.4.2 Survey Infrared Spectra

Figure 3.2 contains survey spectra from 3235 to 3315 cm^{-1}, collected under three different sets of experimental conditions. The black trace is a scan using mass 28 u ($HCNH^+$), which selects for features that derive from HCN dimer or larger clusters. The experimental partial pressure of HCN was optimized to favor the doping of two HCN molecules, and the effusive O_2 flow through the MGC was turned off .[7] The features found at 3237.6 cm^{-1} and 3308.1 cm^{-1} correspond to the H-bonded and "free" CH stretches of the linear HCN–HCN hydrogen-bonded complex, respectively.[45] The small feature at 3313.56 cm^{-1} is the HCN monomer $R(0)$ transition, which is observable on most mass channels due to it being an intense depletion that indirectly causes a depletion of all droplets in the beam.

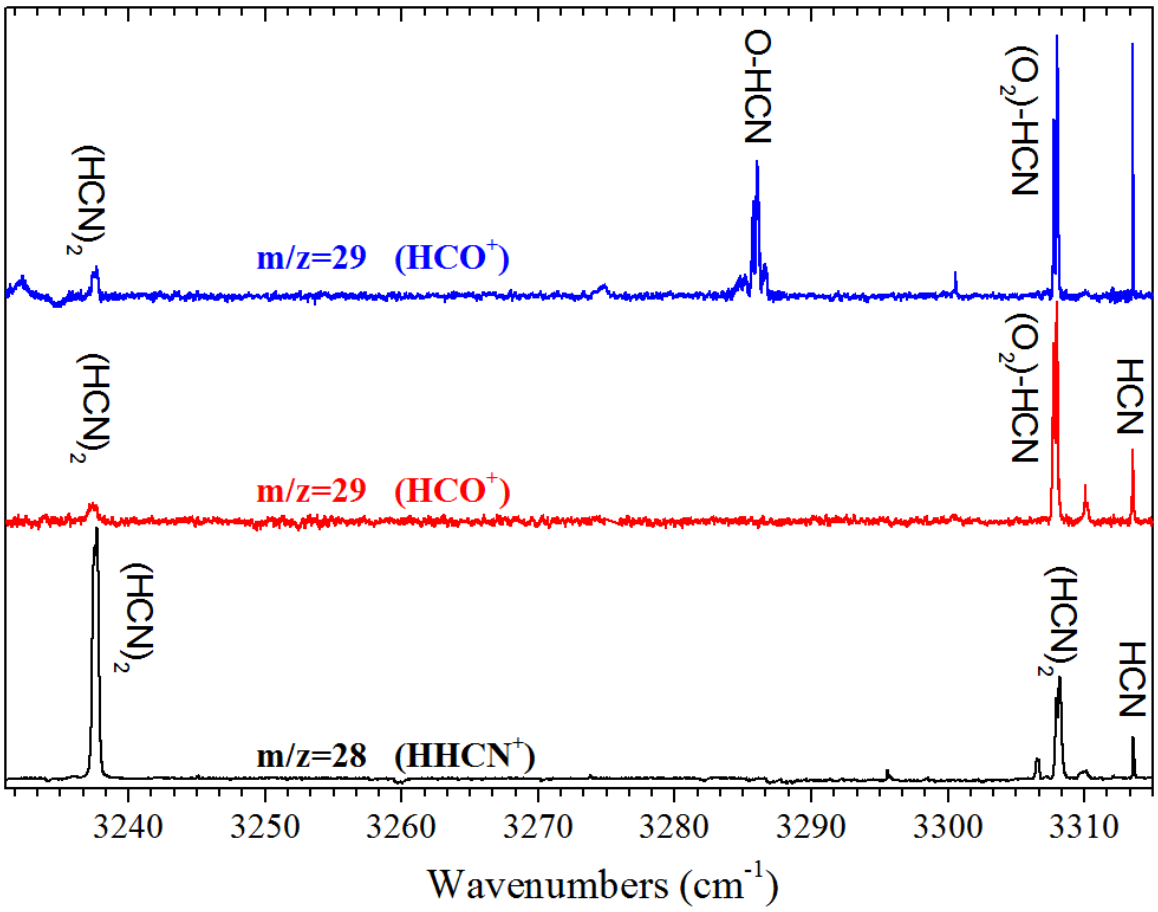

Figure 3.2: Three survey spectra in the CH stretching region of the HCN monomer and dimer. The black trace is a spectrum collected when experimental conditions favored dimer formation within the droplets, and no O_2 was present in the droplet beam. This scan illustrates which features belong to clusters containing primarily $(HCN)_n$ or complexes with impurities in the droplet beam. The red trace is a spectrum collected with experimental conditions that optimize doping of one HCN and O_2 with the molecular gas cracker off (cracker power = 0 Watts). The peaks near 3308 and 3310 cm^{-1} are signatures of the O_2–HCN complex formed in the droplets. The blue trace was collected with the same experimental parameters as the red trace except the molecular gas cracker was turned to 100 W. The feature near 3286 cm^{-1} is very sensitive to cracker power, and the effusive pressure of O_2.

The red trace was recorded with O_2 flowing through the room temperature MGC. The experimental partial pressures of O_2 and HCN were optimized to maximize the probability associated with the sequential capture of monomers (*i.e.* one of each O_2 and HCN). The spectrum corresponds to the depletion signal recorded in mass channel 29 u, which is likely the HCO^+ ion. The largest feature in the spectrum is observed in the vicinity of the free stretch of the HCN dimer; however, upon closer inspection, this feature is clearly different, and it is assigned to the CH stretch of a linear O_2–HCN complex. The band origin is centered at 3307.9 cm^{-1}, which is 0.2 cm^{-1} to the red of the $(HCN)_2$ band. The feature found near 3310 cm^{-1} is assigned to a second isomer of the O_2–HCN van der Waals complex. High resolution scans of the two HCN–O_2 bands are shown in Figure A3.2 in the appendix.

The blue trace was recorded with the same experimental conditions used for the red trace (depletion in m/z = 29 u); the only difference being that the MGC was heated to CP = 100 W. The most notable change in the survey spectrum upon heating the MGC is the new group of features located near 3286 cm^{-1}. It is important to note that we have previously measured high resolution spectra of the helium-solvated HCN–CO, HCN–CO_2, and HCN–H_2O binary complexes.[46] We have confirmed that the newly observed features near 3286 cm^{-1} do not correspond to any of these molecular complexes. Moreover, the 3286 cm^{-1} feature disappears upon turning off the O_2 flow through MGC.

3.4.3 High Resolution Spectra

A higher resolution scan of the features near 3286 cm^{-1} reveals partially-resolved rotational structure, as shown in Figure 3.3. The black trace is a spectrum recorded with

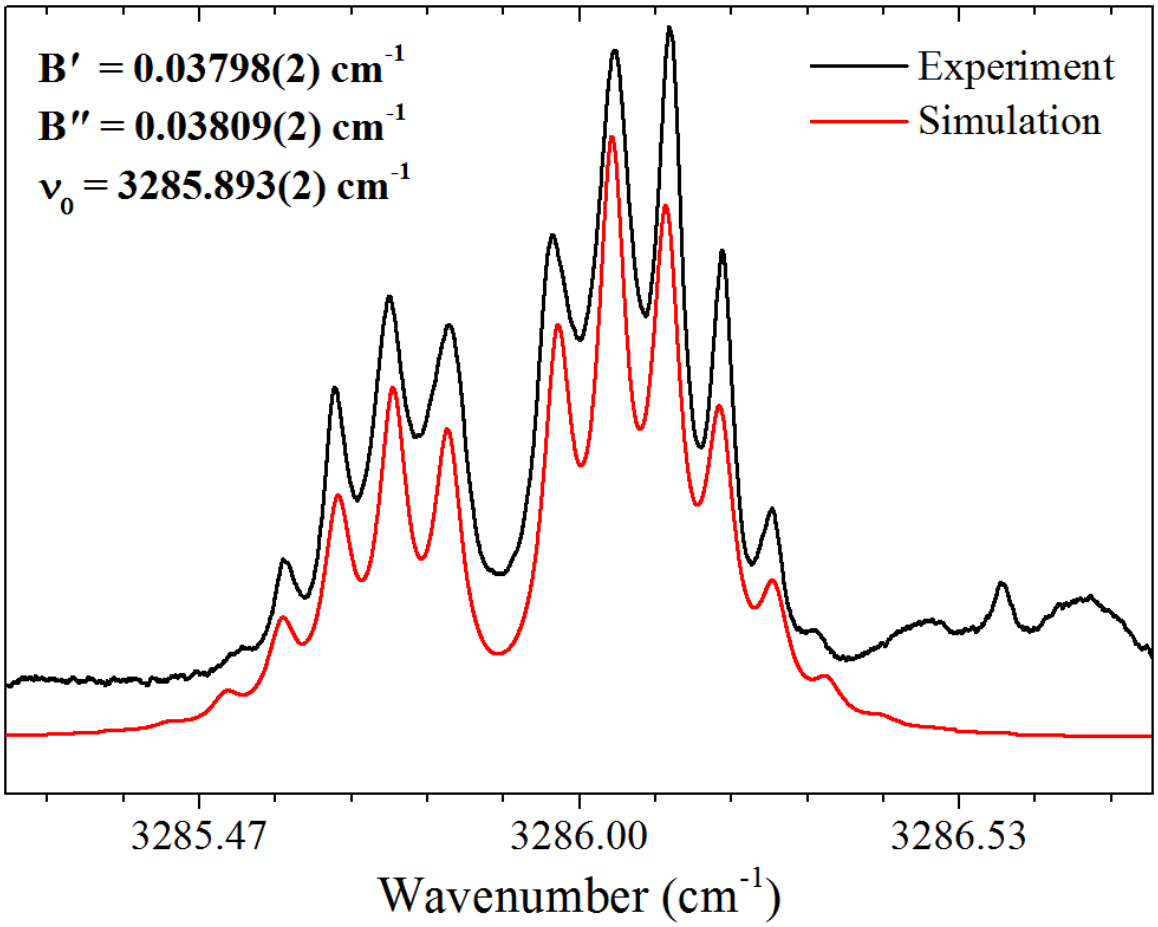

Figure 3.3: The black trace is a high resolution scan of the feature near 3286 cm^{-1}. The red trace is a simulation using PGOPHER of a linear rotor with three parameters: band origin, the ground, and vibrationally-excited rotational constants. A fit to the rotational substructure using a linear least squares method determined the parameter values listed in the inset. Nine rovibrational lines were used in the fit. The simulation used a rotational temperature of 0.4 Kelvin and convoluted each transition with a Lorentzian line shape with 0.08 cm^{-1} linewidth. Uncertainties given in the last digit of each fitted parameter are the standard deviations of the fit. The unresolved P-Q-R contour to the blue of the main band is likely due to a complex containing multiple HCN molecules, for example, O-HCN-HCN.

parameters similar to those used to obtain the blue survey scan in Figure 3.2; however, the signal in Figure 3.3 corresponds to depletion on mass channel 42 u (CNO^+). It was found through *difference mass spectrometry* that the 3285.89 cm^{-1} band also appears as a depletion signal on channel 42 u, which provides somewhat higher signal to noise, in comparison to 29 u and other channels. The observation of large depletions on mass channels 29 u and 42 u is consistent with a spectral carrier having both HCN and oxygen atom or oxygen-containing constituents. The absence of a *Q*-branch implies a spectral carrier with a linear structure. The rotational substructure was fit to a linear rotor Hamiltonian using PGOPHER,[47-49] in which the band origin and the rotational constants in the ground and excited vibrational states were optimized *via* a least squares fitting algorithm. In total, nine rovibrational lines were used in the fit; the line centers were determined from Lorentzian line shape fits. The constants obtained from the linear rotor fit are given in Table 3.1 and shown as an inset to Figure 3.3.

When compared to the rotational constant of the linear, hydrogen-bound (H-bound) O−HCN ($^3\Sigma$) complex computed at the CCSD(T)/ANO1 level of theory, the experimental ground state constant is smaller by a factor of 2.5. For similarly-sized helium-solvated systems,[6,7] indeed, the average effect of helium solvation is to reduce the rotational constant by a factor of approximately 2.5. We have also computed the frequency shift of the CH stretch upon complexation (-28.3 cm^{-1}) for the H-bound species, and this compares favorably to the 25.4 cm^{-1} red shift observed experimentally (Table 3.1). In contrast, the shift predicted for the nitrogen-bound (N-bound) complex is significantly smaller (~0.5 cm^{-1}); an additional band near the free HCN band origin is not observed in the survey spectrum when the MGC is turned on. In combination with its

Table 3.1: Experimental and Computed Properties of the Linear, Triplet Complexes between O(^{3}P) and HCN.

	O···HCN[a]		HCN···O[a]		Experiment
SCF Reference	ROHF	UHF	ROHF	UHF	---
C-H Bond Distance (Å)	1.0690	1.0690	1.0668	1.0668	---
C-N Bond Distance (Å)	1.1606	1.1606	1.1602	1.1602	---
O···H Distance (Å)	2.4004	2.4002	---	---	---
O···N Distance (Å)	---	---	3.0496	3.0500	---
Rotational Const. B″(cm^{-1})	0.0965	0.0965	0.1161	0.1161	0.0381[b]
Dipole Moment (Debye)	3.23	3.23	3.09	3.09	3.24
ω_{CH} (cm^{-1})	3423.4	3423.4	3451.1	3451.1	---
ω_{HCN}[c] - ω_{CH} (cm^{-1})	28.3	28.3	0.6	0.6	25.6[d]

[a] Computed parameters are from a CCSD(T)/ANO1 optimization with subsequent harmonic frequency computation at the same level of theory.
[b] For comparison to computed values, average reduction of rotational constants is by a factor of 2.5 due to helium solvation.
[c] HCN CH harmonic frequency (3451.7 cm^{-1}) computed at CCSD(T)/ANO1
[d] Measured with respect to helium droplet HCN band origin reported by Nauta and Miller[50]

dependence on MGC power and HCN/O_2 pick-up conditions, the comparison of experiment to theory motivates an assignment of the 3285.89 cm^{-1} feature to the CH stretch of a linear O–HCN ($^3\Sigma$) van der Waals complex, whose *ab initio* optimized geometric parameters are given in Table 3.1.

To further explore the new spectroscopic feature, Stark field dependence of the band structure was exploited. It has been shown[21] that dipole moments of helium-solvated molecules are similar to the corresponding gas-phase values, differing by less than a few percent when comparisons are available. Stark spectra recorded with four field strengths (including 0 kV/cm) are shown in Figure 3.4. The evolution of the rotational structure with electric field strength was simulated to determine a dipole moment for the complex (red traces in Figure 3.4).[47-49] The resulting ground state dipole moment (3.24(3) D) is comparable to predictions at the CCSD(T)/ANO1 level of theory for the H-bound O–HCN isomer in the ground $^3\Sigma$ electronic state (3.23 D). The dipole moment of the N-bound isomer is predicted to be 3.09 D, well outside the experimental error bar. For comparison, the dipole moment of helium-solvated HCN is 2.95 D.[21]

3.4.4 *Ab Initio* Potential Energy Surface Computations

To supplement the experimental data, a theoretical investigation involving high-level single reference geometry optimization and harmonic frequency analysis was carried out. Two isomers of the O + HCN system were identified as minima, both linear structures. The energy difference between the linear isomers is 291 cm^{-1} with the H-bound isomer being the global minimum. CCSD(T) harmonic frequencies with both ROHF and UHF references are presented in Table 3.1. The lack of reference dependence

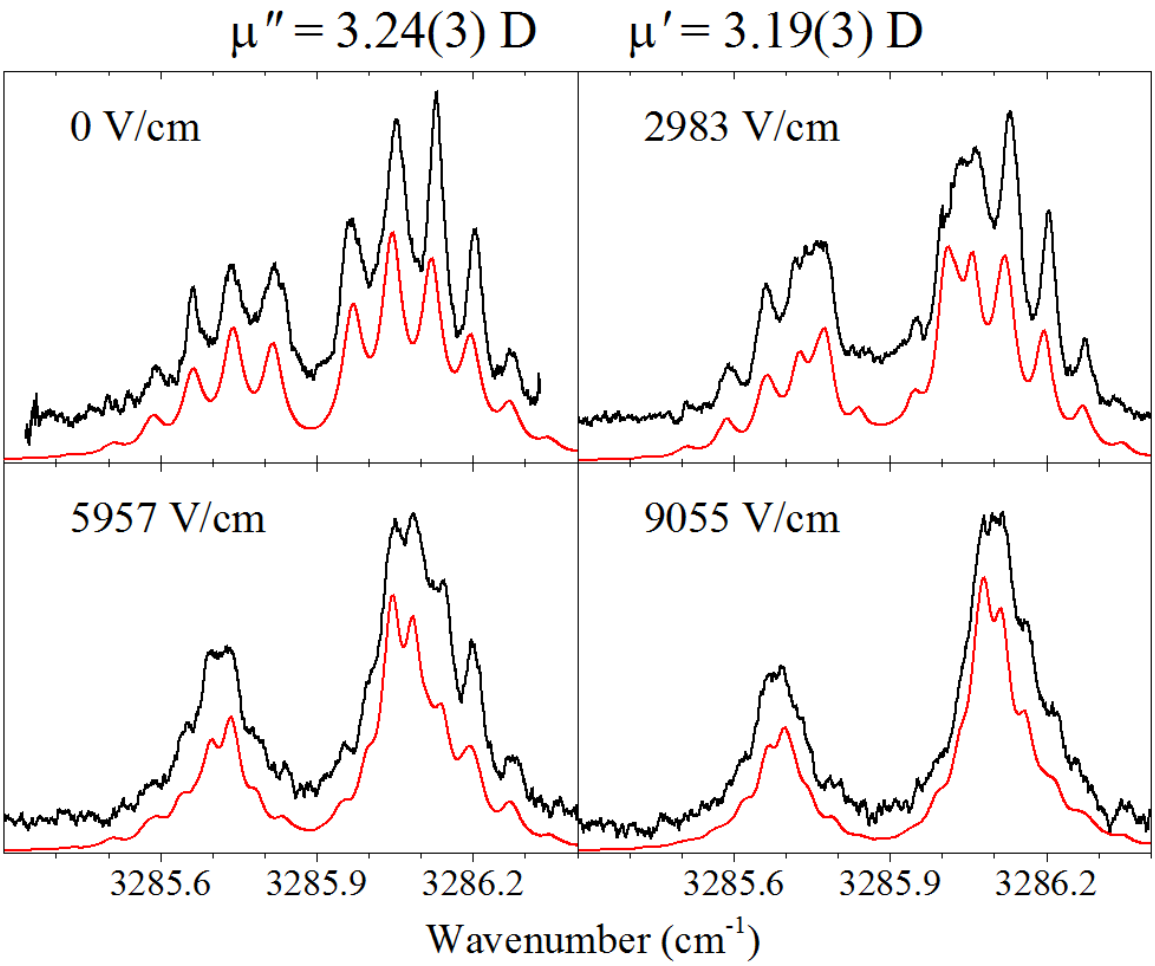

Figure 3.4: Stark spectra using perpendicular laser polarization (selection rule $\Delta M = \pm 1$) with four different Stark field strengths (including 0 V/cm). Rotational parameters and band origin were fixed from the zero-field fit, and simulations included the same 0.4 K rotational temperature and 0.08 cm^{-1} Lorentzian linewidth for each transition as the zero-field simulations. Dipole moments in the ground and excited vibrational states were empirically optimized to best reproduce experimental observations. Uncertainties are approximated.

suggests that there are no wavefunction instabilities compromising the results.

When discussing these linear structures, there are three electronic states that are close in energy and depend on the orientation of the three 2p orbitals of the oxygen atom. One of these states in each geometry is non-degenerate ($^3\Sigma$), with the doubly occupied p-orbital oriented along the HCN internuclear axis. The other two states are degenerate ($^3\Pi$), with the doubly occupied p-orbital oriented perpendicular to the internuclear axis. To identify barriers heights, we computed the non-relativistic, adiabatic potential energy surfaces for interconversion between the two linear species. Between the Jacobi coordinate extremes of 0º and 180º (H- and N-bound, respectively) the symmetry of the molecule devolves from $C_{\infty v}$ to C_s. In this intermediate region, the potentials are no longer well-represented using single determinant methods, especially in the region around the barrier. Therefore, the two-dimensional potential energy surfaces of the three lowest-lying electronic states for the complex were calculated with NEVPT2. NEVPT2 provides a qualitatively correct description of the low-lying electronic states in the regions of the PES where configuration mixing is strong. Additionally it is size consistent; the quality of the energy computations does not degrade in the regions of the PES where O and HCN are far apart.

The scan over the Jacobi coordinates R and θ for the $^3A''$ ground electronic state is shown in the top panel of Figure 3.5. The R and θ coordinates are defined as shown in the inset. The NEVPT2 predicted energy difference between linear isomers (323 cm^{-1}) agrees qualitatively with the results from the CCSD(T)/ANO1 computations (291 cm^{-1}). The barrier between linear isomers along the ground electronic surface is 42.4 cm^{-1} at the NEVPT2/aug-cc-pVTZ level of theory. A slice of each two-dimensional surface at R=4.0

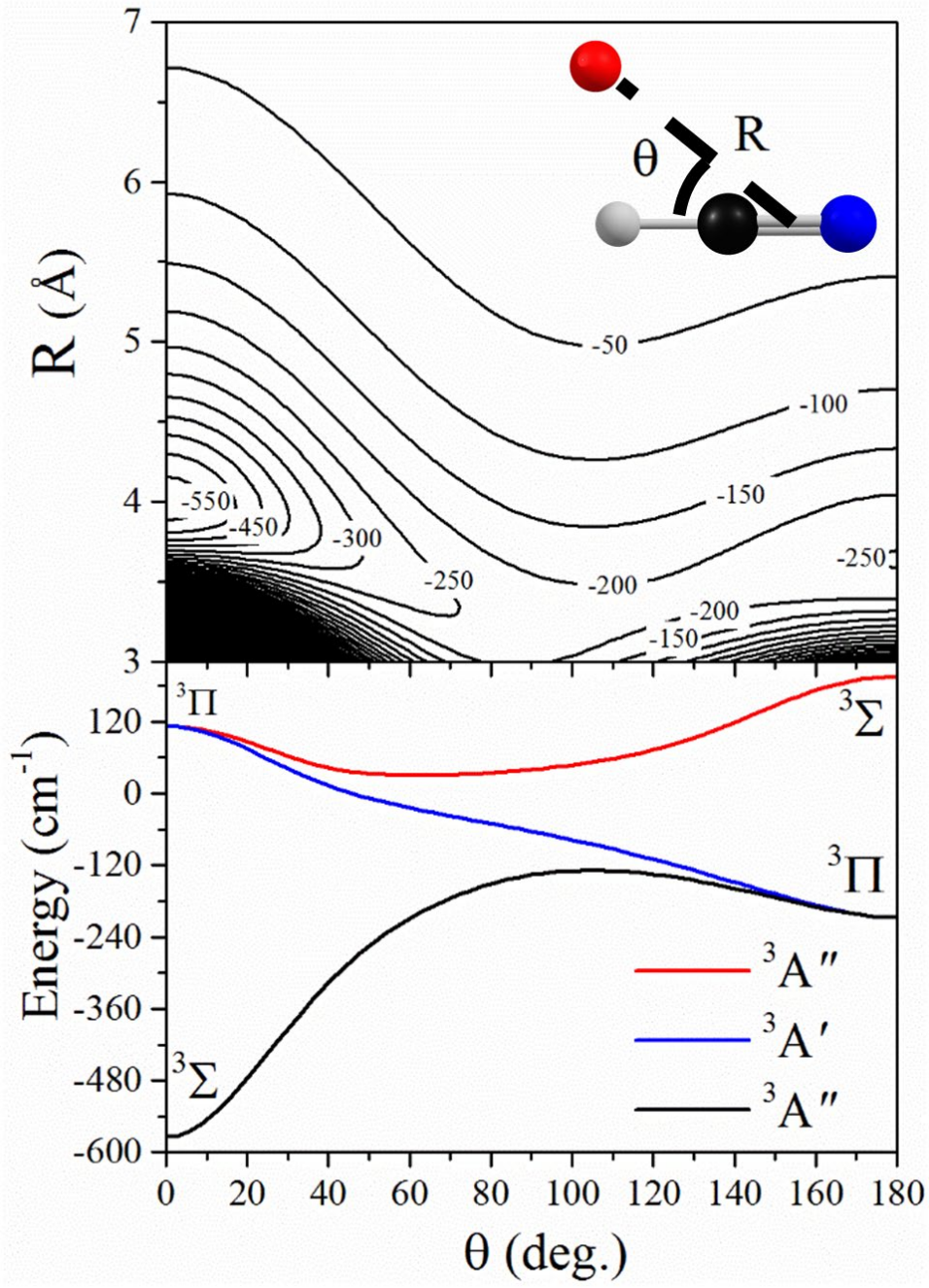

Figure 3.5: *Top panel*: NEVPT2/aug-cc-pVTZ potential energy scan of the ground electronic surface of triplet O–HCN. Inset shows the definition of the Jacobi coordinates used in the scan. Contours are spaced every 50 cm^{-1} from -550 cm^{-1} to 6000 cm^{-1} measured relative to the asymptotic limit. The two minimum energy structures can be found at (R = 4.00 Å, θ = 0°) and (R = 3.65 Å, θ = 180°) with energies of -575 and -252 cm^{-1}. *Bottom panel*: A slice of all three electronic surfaces calculated with state-averaged CASSCF/NEVPT2 at R = 4.0 Å. Slices illustrate the correlation between the linear $C_{\infty v}$ symmetry species and the three C_s symmetry electronic surfaces.

Å is presented in the lower panel of Figure 3.5 to illustrate the correlation between the three electronic surfaces and the Σ/Π states of the linear species. From this long-range potential surface, it is apparent that a large fraction of O + HCN approach geometries will favor the production of the lower energy H-bound species. It is not obvious, however, that N-bound isomers would be completely absent. We are left to conclude that either zero-point/non-adiabatic effects render the interconversion of N-bound isomers barrierless or that, upon complexation in the vicinity of the N-bound potential well, the helium droplet is not capable of quenching the kinetic energy gain prior to its rearrangement over (or through) the ~40 cm^{-1} barrier. This is not without precedent; previous work on $(HF)_n$ clusters[51] and acetylene/furan clusters[52] (for example) showed that barriers of similar magnitude could be overcome during the aggregation process within the helium droplet. Future computations of the O-HCN potential surfaces, including spin-orbit coupling and non-adiabatic effects,[53-54] may be capable of providing further insight into this issue.

3.5 Summary and Outlook

A commercial molecular gas cracker for the production of $O(^3P)$ atoms has been used to dope helium nanodroplets. On the basis of mass spectrometry results, we estimate that with optimal conditions, 26% of the droplet ensemble is doped with single oxygen atoms. Upon sequential capture of an $O(^3P)$ atom and HCN, a weakly bound complex is observed *via* measurements of beam depletion in the CH stretching region of the IR spectrum. The analysis of rotational fine structure and comparisons to *ab initio* computations support an assignment of a band centered at 3285.89 cm^{-1} to a linear, H-

bound, ($^3\Sigma$) O−HCN van der Waals complex. There is no experimental evidence for the production of an N-bound complex. Multi-reference *ab initio* computations predict a relatively small barrier for interconversion from the higher energy N-bound complex to the more stable H-bound system.

According to Smith *et al*.,[55] for molecule + radical reactions, the energetic difference between the molecule's ionization energy (IE) and the radical's electron affinity (EA) can provide insight into the nature of the reaction barrier, either *above* or *below* the reactant asymptote. They propose that a difference (IE − EA) greater than 8.75 eV indicates a real barrier above the asymptotic limit, whereas a value below 8.75 eV indicates a submerged barrier.[55] Indeed, this difference for the O(^{3}P) + HCN system is 12.2 eV. Accordingly, the barrier[11] to oxygen insertion into the CN π system is ~10 kcal/mol above the reactant asymptote, and a van der Waals complex is observed when these species are brought together in a 0.4 K helium nanodroplet. However, O(^{3}P) reactions with *alkenes* are predicted to cross the postulated 8.75 eV threshold as the alkene substitution pattern evolves from ethene (no substitution) to propene (methyl group substitution) to butene (dimethyl substitution, of which there are four different isomers), and this trend was tested by Sabbah *et al.*[56] Their findings corroborated the behavior predicted by Smith *et al.*[55] The HCN + O(^{3}P) results presented here demonstrate the feasibility for analogous alkene + O(^{3}P) spectroscopic studies, in which O(^{3}P) and alkenes of varying substitution are combined in helium droplets *via* the sequential capture scheme. As the *real* reaction barrier (*i.e.* for the ethene and propene reactions) evolves to being *submerged* below the asymptotic limit (*i.e*. for the butene reactions), one might expect that strongly bound reaction intermediates, such as triplet biradicals,[5, 57-66] will be

observed in helium droplets, rather than van der Waals complexes. Given the fact that a 10,000 atom helium droplet can dissipate 140 kcal/mol, it should be possible to quench the internal energy of these reaction intermediates and probe them for the first time spectroscopically.

3.6 Appendix

3.6.1 Ancilotto Parameter

The Ancilotto parameter is a dimensionless number that provides a qualitative measure of the ratio between the energetic stabilization of helium solvation and the energetic cost of creating a cage around the dopant within the droplet.[17] It has the following expression.

$$\lambda = \frac{\rho \epsilon r_{min}}{\sigma 2^{1/6}} \tag{A3.1}$$

ρ is the number density of atoms in the region of the solute, and σ is the surface tension of liquid helium; ε and r_{min} are the two parameters of a Lennard-Jones (LJ) potential, V(r).

$$V(r) = \epsilon \left[\left(\frac{r_{min}}{r} \right)^{12} - 2 \left(\frac{r_{min}}{r} \right)^{6} \right] \tag{A3.2}$$

The Lennard-Jones potential is used to model the solute-solvent interaction, and a one-dimensional scan of the internuclear coordinate for a helium atom and the impurity is fit to the LJ potential to determine ε and r_{min}. ρ and σ were calculated using DFT, and have values[177] of 0.0218 $Å^{-3}$ and 0.179 $cm^{-1}Å^{-2}$. Ancilotto *et al.*[17] further indicate that solvation of an impurity in a helium droplet is dependent on the value of λ with respect to the critical value: 1.9. Above the threshold, the energetic stabilization outweighs the

penalty of solvation and the impurity is predicted to be solvated. Below the threshold, the impurity remains on the surface of the droplet.

The pair potential of He and O(^{3}P) was computed with CCSD(T) at the complete basis set (CBS) limit using a restricted open-shell reference wavefunction within the CFOUR computational package.[22] The CBS limit was estimated using the basis set extrapolation methods of Feller[67] and Helgaker *et al.*,[68] which have been programmed into CFOUR. Extrapolation of the SCF energy was computed using the aug-cc-pVXZ (X= Q, 5, 6) basis sets.[38] The dynamic electron correlation was computed using the aug-cc-pVXZ (X=Q,5) basis sets. CFOUR approximated the energy at the CBS limit using the following scheme.

$$E_\infty(\mathrm{SCF}) = E(\mathrm{SCF/cc-pVXZ}) - ae^{-bX} \tag{A3.3}$$

$$\Delta E_\infty(\mathrm{CC}) = \Delta E(\mathrm{CC/cc-pVXZ}) - \frac{c}{X^3} \tag{A3.4}$$

Here, X is the cardinality of the Dunning basis set used, and a, b and c are constants that are determined by solution to Eqs. (A3.3)[67] and (A3.4)[68]. Final energy at the CBS limit is found from the sum $E_\infty(\mathrm{SCF}) + \Delta E_\infty(\mathrm{CC})$. The two low-lying electronic states on triplet potential surface of He + O(^{3}P) were computed in CFOUR. The states are of Σ and Π symmetry. To scan the internuclear degree of freedom in these states, the irreducible representations of the occupied molecular orbitals were fixed at every scan point in the C_{2v} point group (largest abelian subgroup of $C_{\infty v}$). The Σ electronic state occupation was α-spin(4 A_1/0 A_2/1 B_1/1 B_2) and β-spin(4 A_1/0 A_2/0 B_1/0 B_2), and α-spin(4 A_1/0 A_2/1 B_1/1 B_2) and β-spin(3 A_1/0 A_2/1 B_1/0 B_2) was arbitrarily chosen as one of the Π electronic states.

Computed pair potentials were fit to a LJ potential using Wolfram Mathematica

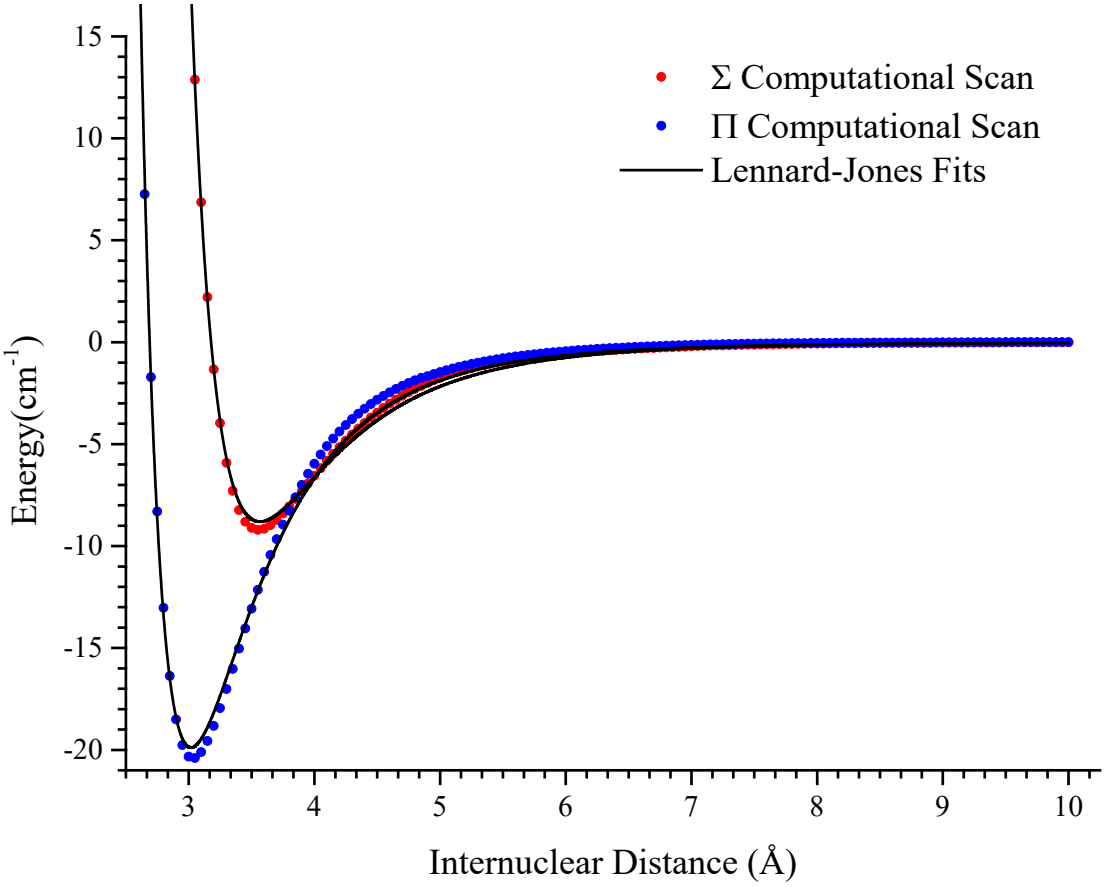

Figure A3.1: Potential energy surface scans of the internuclear degree of freedom in the He + O(^{3}P) system. The alignment of the doubly occupied p-orbital determines the symmetry. Perpendicular to the scan coordinate, the system is a doubly degenerate Π state, and oriented along, the system is a Σ state. These two states were fit to a Lennard-Jones (LJ) potential to determine the LJ parameters ε and r_{min}, which was computed in Mathematica 10.4[69]

10.4's FindFit algorithm.[69] The fit provided the optimized (ε, r_{min}) from the theoretical data: (19.9 cm^{-1}, 3.02 Å) for the Π electronic states and (8.8 cm^{-1}, 3.57 Å) for the Σ electronic state. The scan data and fits are shown in Figure A3.1. From these parameters, we calculate Ancilotto parameters of 6.5 and 3.4 for the Π and Σ, respectively. Since the Ancilotto parameters of both states are above the critical value, these computational results predict the solvation of ^{3}P atomic oxygen within a helium droplet.

3.6.2 Assignment of the Spectral Features of HCN-O_2:

Figure A3.2 shows high-resolution scans of the two features centered at 3307.9 and 3310.1 cm^{-1}. The absence of a *Q*-branch in the lower frequency band is indicative of a linear complex. The higher frequency band must then have a non-linear structure. Both features optimize under the same conditions, indicating they arise from a spectral carrier having the same composition. Moreover, both features optimize at the same experimental conditions that optimize the doping of the HCN monomer, indicating these features derive from complexes with one HCN. The O_2 partial pressure is consistent with our previous experiments, wherein nascent radicals are reacted with O_2 to form peroxyradicals.[70-73] This motivates an assignment of the two bands to a linear and non-linear HCN–O_2. We have not attempted in this work to compute the structures of the two isomers.

3.6.3 Difference Mass Spectra

Difference mass spectra are obtained from a technique known as optically selective mass spectrometry (OSMS). Wherein the technique for obtaining infrared spectra requires the selection of a mass channel and scanning the infrared laser, OSMS

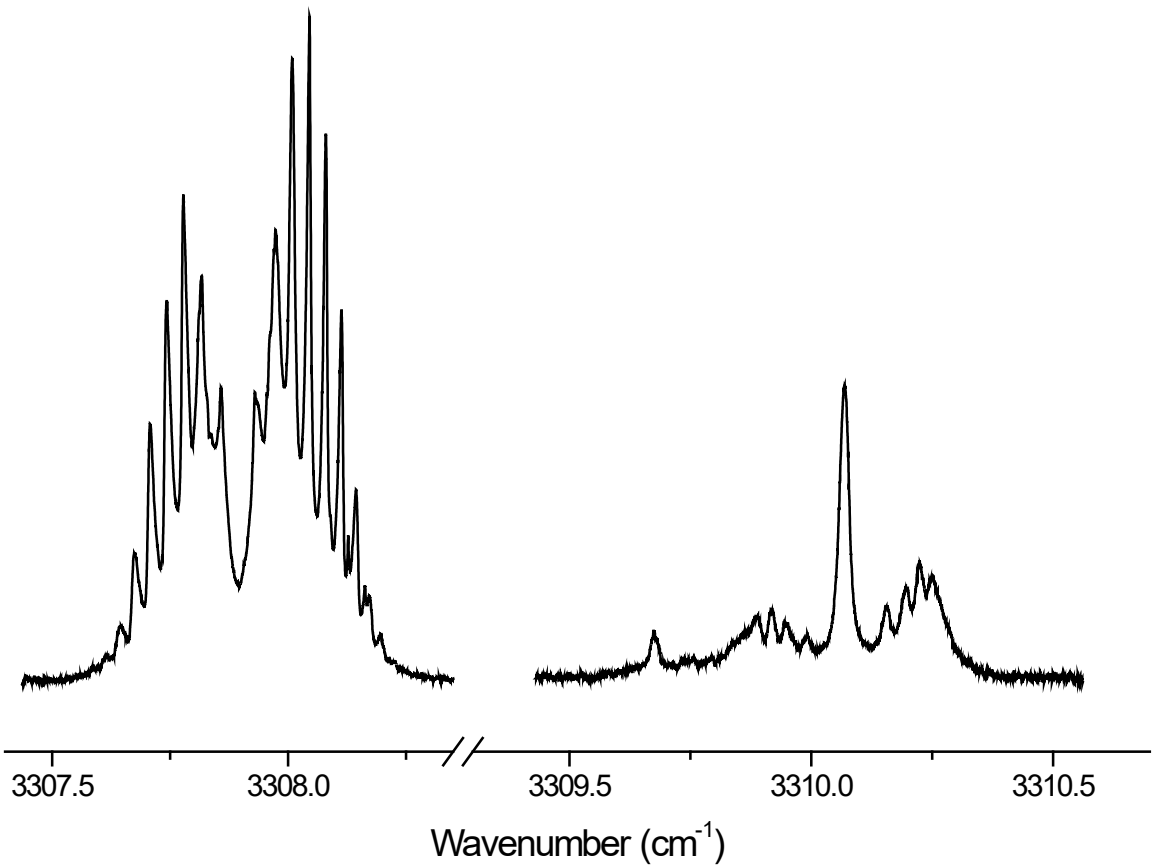

Figure A3.2: High resolution scans of the two features that arise from sequential capture of HCN and O_2 in a helium droplet. Scans were obtained at the same experimental conditions, which were optimized to favor doping of one each of the monomers.

works in the opposite configuration. The laser frequency is fixed (usually to a resonant transition identified in an IR spectrum), and the mass is scanned. Masses, whose arrival at the detector is intensely modulated by the laser, have larger depletions as measured by a lock-in amplifier, and thus intensity in an OSMS is related to the amount of light absorbed by the droplet ensemble. A higher intensity in an OSMS indicates a favorable channel for spectroscopy at that frequency.

For this experiment, the signature of the $^3\Sigma$ O–HCN complex has intense depletions on several channels, the largest of which is 27 u. However, this mass channel does not discriminate between other complexes that involve HCN, so to quasi-mass select, choosing 29 or 42 u requires the presence of an oxygen atom. We find that 42 u provides the highest signal to noise ratio on the 3286 cm^{-1} band.

3.7 References

(1) Miller, J. A.; Kee, R. J.; Westbrook, C. K., Chemical-Kinetics and Combustion Modeling. *Annu. Rev. Phys. Chem.* **1990**, *41*, 345-387

(2) Viti, S.; Roueff, E.; Hartquist, T. W.; des Forets, G. P.; Williams, D., Interstellar Oxygen Chemistry. *Astron. Astrophys.* **2001**, *370*, 557-569

(3) Occhiogrosso, A.; Viti, S.; Balucani, N., An Improved Chemical Scheme for the Reactions of Atomic Oxygen and Simple Unsaturated Hydrocarbons - Implications for Star-forming Regions. *Mon. Not. R. Astron. Soc.* **2013**, *432*, 3423-3430

(4) Nguyen, T. L.; Vereecken, L.; Peeters, J., Quantum Chemical and Theoretical Kinetics Study of the $O(^3P)+C_2H_2$ Reaction: A Multistate Process. *J. Phys. Chem. A* **2006**, *110*, 6696-6706

(5) Rajak, K.; Maiti, B., Trajectory Surface Hopping Study of the $O(^3P) + C_2H_2$ Reaction Dynamics: Effect of Collision Energy on the Extent of Intersystem Crossing. *J. Chem. Phys.* **2014**, *140*, 044314

(6) Choi, M. Y.; Douberly, G. E.; Falconer, T. M.; Lewis, W. K.; Lindsay, C. M.; Merritt, J. M.; Stiles, P. L.; Miller, R. E., Infrared Spectroscopy of Helium Nanodroplets: Novel Methods for Physics and Chemistry. *Int. Rev. Phys. Chem.* **2006**, *25*, 15-75

(7) Toennies, J. P.; Vilesov, A. F., Superfluid Helium Droplets: A Uniquely Cold Nanomatrix for Molecules and Molecular Complexes. *Angew. Chem. Int. Ed.* **2004**, *43*, 2622-2648

(8) Miller, J. A.; Branch, M. C.; McLean, W. J.; Chandler, D. W.; Smooke, M. D.; Kee, R. J., The Conversion of HCN to NO and N_2 in H_2-O_2-HCN-Ar Flames at Low Pressure. *Symp. (Int.) Combust., [Proc.]* **1985**, *20*, 673-684

(9) Dagaut, P.; Glarborg, P.; Alzueta, M. U., The Oxidation of Hydrogen Cyanide and Related Chemistry. *Prog. Energy Combust. Sci.* **2008**, *34*, 1-46

(10) Szekely, A.; Hanson, R. K.; Bowman, C. T., Shock Tube Study of the Reaction Between Hydrogen Cyanide and Atomic Oxygen. *Symp. (Int.) Combust., [Proc.]* **1985**, *20*, 647-654

(11) Miller, J. A.; Parrish, C.; Brown, N. J., A Statistical Theoretical Investigation of the Thermal Rate Coefficient and Branching Ratio for the Reaction O + HCN → Products. *J. Phys. Chem.* **1986**, *90*, 3339-3345

(12) Perry, R. A.; Melius, C. F., The Rate and Mechanism of the Reaction of HCN with Oxygen Atoms over the Temperature Range 540-900 K. *Symp. (Int.) Combust., [Proc.]* **1985**, *20*, 639-646

(13) Mielke, Z.; Andrews, L., Matrix Infrared Studies of the HCN+O_3 and HCN+O Systems. *J. Phys. Chem.* **1990**, *94*, 3519-3525

(14) Liang, T.; Flynn, S. D.; Morrison, A. M.; Douberly, G. E., Quantum Cascade Laser Spectroscopy and Photoinduced Chemistry of Al-$(CO)_n$ Clusters in Helium Nanodroplets. *J. Phys. Chem. A* **2011**, *115*, 7437-7447

(15) Lewerenz, M.; Schilling, B.; Toennies, J. P., Successive Capture and Coagulation of Atoms and Molecules to Small Clusters in Large Liquid-Helium Clusters. *J. Chem. Phys.* **1995**, *102*, 8191-8207

(16) Chin, S. A.; Krotscheck, E., Systematics of Pure and Doped ^{4}He Clusters. *Phys. Rev. B* **1995**, *52*, 10405-10428

(17) Ancilotto, F.; Lerner, P. B.; Cole, M. W., Physics of Solvation. *J. Low Temp. Phys.* **1995**, *101*, 1123-1146

(18) Franke, P. R.; Tabor, D. P.; Moradi, C. P.; Douberly, G. E.; Agarwal, J.; Schaefer, H. F.; Sibert, E. L., Infrared Laser Spectroscopy of the *n*-Propyl and *i*-Propyl Radicals: Stretch-Bend Fermi Coupling in the Alkyl CH Stretch Region. *J. Chem. Phys.* **2016**, *145*, 224304, 224304.

(19) Morrison, A. M.; Liang, T.; Douberly, G. E., Automation of an "Aculight" Continuous-Wave Optical Parametric Oscillator. *Rev. Sci. Instrum.* **2013**, *84*, 013102, 013102.

(20) Hernandez, F. J.; Brice, J. T.; Leavitt, C. M.; Liang, T.; Raston, P. L.; Pino, G. A.; Douberly, G. E., Mid-Infrared Signatures of Hydroxyl Containing Water Clusters: Infrared Laser Stark Spectroscopy of OH-H_2O and $OH(D_2O)_n$ (n=1-3). *J. Chem. Phys.* **2015**, *143*, 164304, 164304.

(21) Stiles, P. L.; Nauta, K.; Miller, R. E., Dipole Moments of Molecules Solvated in Helium Nanodroplets. *Phys. Rev. Lett.* **2003**, *90*, 135301, 135301.

(22) Tscherbul, T. V.; Krems, R. V., Tuning Bimolecular Chemical Reactions by Electric Fields. *Phys. Rev. Lett.* **2015**, *115*, 5, 023201.

(23) Stanton, J. F., Why CCSD(T) Works: A Different Perspective. *Chem. Phys. Lett.* **1997**, *281*, 130-134

(24) Watts, J. D.; Gauss, J.; Bartlett, R. J., Open-Shell Analytical Energy Gradients for Triple Excitation Many-Body, Coupled-Cluster Methods - MBPT(4), CCSD+T(CCSD), CCSD(T), and QCISD(T). *Chem. Phys. Lett.* **1992**, *200*, 1-7

(25) Raghavachari, K.; Trucks, G. W.; Pople, J. A.; Headgordon, M., A 5th-Order Perturbation Comparison of Electron Correlation Theories. *Chem. Phys. Lett.* **1989**, *157*, 479-483

(26) Almlof, J.; Taylor, P. R., General Contraction of Gaussian-Basis Sets. I. Atomic Natural Orbitals for First-Row and Second-Row Atoms. *J. Chem. Phys.* **1987**, *86*, 4070-4077

(27) Hampel, C.; Peterson, K. A.; Werner, H. J., A Comparison of the Efficiency and Accuracy of the Quadratic Configuration-Interaction (QCISD), Coupled Cluster (CCSD), and Brueckner Coupled Cluster (BCCD) Methods. *Chem. Phys. Lett.* **1992**, *190*, 1-12

(28) Neese, F., The ORCA Program System. *Wiley Interdiscip. Rev.: Comput. Mol. Sci.* **2012**, *2*, 73-78

(29) Roos, B. O.; Taylor, P. R.; Siegbahn, P. E. M., A Complete Active Space SCF Method (CASSCF) using a Density-Matrix Formulated Super-CI Approach. *Chem. Phys.* **1980**, *48*, 157-173

(30) Schweinfurth, D.; Sommer, M. G.; Atanasov, M.; Demeshko, S.; Hohloch, S.; Meyer, F.; Neese, F.; Sarkar, B., The Ligand Field of the Azido Ligand: Insights into Bonding Parameters and Magnetic Anisotropy in a Co(II)-Azido Complex. *J. Am. Chem. Soc.* **2015**, *137*, 1993-2005

(31) Weigend, F.; Kattannek, M.; Ahlrichs, R., Approximated Electron Repulsion Integrals: Cholesky Decomposition versus Resolution of the Identity Methods. *J. Chem. Phys.* **2009**, *130*, 164106, 164106.

(32) Malmqvist, P. A.; Roos, B. O., The CASSCF State Interaction Method. *Chem. Phys. Lett.* **1989**, *155*, 189-194

(33) Angeli, C.; Bories, B.; Cavallini, A.; Cimiraglia, R., Third-Order Multireference Perturbation Theory: The N-Electron Valence State Perturbation-Theory Approach. *J. Chem. Phys.* **2006**, *124*, 054108, 054108.

(34) Angeli, C.; Borini, S.; Cestari, M.; Cimiraglia, R., A Quasidegenerate Formulation of the Second Order n-Electron Valence State Perturbation Theory Approach. *J. Chem. Phys.* **2004**, *121*, 4043-4049

(35) Angeli, C.; Cimiraglia, R.; Evangelisti, S.; Leininger, T.; Malrieu, J. P., Introduction of n-Electron Valence States for Multireference Perturbation Theory. *J. Chem. Phys.* **2001**, *114*, 10252-10264

(36) Angeli, C.; Cimiraglia, R.; Malrieu, J. P., N-Electron Valence State Perturbation Theory: A Fast Implementation of the Strongly Contracted Variant. *Chem. Phys. Lett.* **2001**, *350*, 297-305

(37) Angeli, C.; Cimiraglia, R.; Malrieu, J. P., N-Electron Valence State Perturbation Theory: A Spinless Formulation and an Efficient Implementation of the Strongly Contracted and of the Partially Contracted Variants. *J. Chem. Phys.* **2002**, *117*, 9138-9153

(38) Kendall, R. A.; Dunning, T. H.; Harrison, R. J., Electron Affinities of the First-Row Atoms Revisited. Systematic Basis-Sets and Wave-Functions. *J. Chem. Phys.* **1992**, *96*, 6796-6806

(39) Scheidemann, A.; Schilling, B.; Toennies, J. P., Anomalies in the Reactions of He^+ with SF_6 Embedded in Large ^4He Clusters. *J. Phys. Chem.* **1993**, *97*, 2128-2138

(40) Ruchti, T.; Forde, K.; Callicoatt, B. E.; Ludwigs, H.; Janda, K. C., Charge Transfer and Fragmentation of Liquid Helium Clusters that Contain One or More Neon Atoms. *J. Chem. Phys.* **1998**, *109*, 10679-10687

(41) Callicoatt, B. E.; Forde, K.; Ruchti, T.; Jung, L. L.; Janda, K. C.; Halberstadt, N., Capture and Ionization of Argon within Liquid Helium Droplets. *J. Chem. Phys.* **1998**, *108*, 9371-9382

(42) Zhao, L. B.; Stancil, P. C.; Gu, J. P.; Liebermann, H. P.; Li, Y.; Funke, P.; Buenker, R. J.; Zygelman, B.; Kimura, M.; Dalgarno, A., Radiative Charge Transfer in Collisions of O with He^+. *Astrophys. J.* **2004**, *615*, 1063-1072

(43) Halberstadt, N.; Janda, K. C., The Resonant Charge Hopping Rate in Positively Charged Helium Clusters. *Chem. Phys. Lett.* **1998**, *282*, 409-412

(44) Brown, A. R.; Franke, P. R.; Douberly, G. E., Helium Nanodroplet Isolation of the Cyclobutyl, 1-Methylallyl, and Allylcarbinyl Radicals: Infrared Spectroscopy and *ab Initio* Computations. *J. Phys. Chem. A* **2017**, *121*, 7576-7587

(45) Nauta, K.; Miller, R. E., Solvent Mediated Vibrational Relaxation: Superfluid Helium Droplet Spectroscopy of HCN dimer. *J. Chem. Phys.* **1999**, *111*, 3426-3433

(46) Douberly, G. E. Infrared Laser Spectroscopy of Dopants in and on Helium Nanodroplets: Rotational and Vibrational Dynamics. University of North Carolina at Chapel Hill, Chapel Hill, NC, 2006.

(47) Western, C. M. *PGOPHER*, University of Bristol Research Data Repository: Bristol, U.K., 2014.

(48) Western, C. M.; Billinghurst, B. E., Automatic Assignment and Fitting of Spectra with PGOPHER. *Phys. Chem. Chem. Phys.* **2017**, *19*, 10222-10226

(49) Western, C. M., PGOPHER: A Program for Simulating Rotational, Vibrational, and Electronic Spectra. *J. Quant. Spectrosc. Radiat. Transfer* **2017**, *186*, 221-242

(50) Nauta, K.; Miller, R. E., Stark Spectroscopy of Polar Molecules Solvated in Liquid Helium Droplets. *Phys. Rev. Lett.* **1999**, *82*, 4480-4483

(51) Douberly, G. E.; Miller, R. E., The Growth of HF Polymers in Helium Nanodroplets: Probing the Barriers to Ring Insertion. *J. Phys. Chem. B* **2003**, *107*, 4500-4507

(52) Metzelthin, A.; Sanchez-Garcia, E.; Birer, O.; Schwaab, G.; Thiel, W.; Sander, W.; Havenith, M., Acetylene center dot center dot center dot Furan Trimer Formation at 0.37 K as a Model for Ultracold Aggregation of Non- and Weakly Polar Molecules. *Chemphyschem* **2011**, *12*, 2009-2017

(53) Zeimen, W. B.; Klos, J.; Groenenboom, G. C.; van der Avoird, A., Bound States of the $Cl(^2P)$-HCl van der Waals Complex from Coupled *ab Initio* Potential Energy Surfaces. *J. Phys. Chem. A* **2003**, *107*, 5110-5121

(54) Zeimen, W. B.; Klos, J.; Groenenboom, G. C.; van der Avoird, A., Erratum: Bound States of the $Cl(^2P)$-HCl van der Waals Complex from Coupled *Ab Initio* Potential Energy Surfaces. *J. Phys. Chem. A* **2004**, *108*, 9319-9322

(55) Smith, I. W. M.; Sage, A. M.; Donahue, N. M.; Herbst, E.; Quan, D., The temperature-dependence of rapid low temperature reactions: experiment, understanding and prediction. *Faraday Discuss.* **2006**, *133*, 137-156

(56) Sabbah, H.; Biennier, L.; Sims, I. R.; Georgievskii, Y.; Klippenstein, S. J.; Smith, I. W., Understanding Reactivity at Very Low Temperatures: The Reactions of Oxygen Atoms with Alkenes. *Science* **2007**, *317*, 102

(57) Leonori, F.; Balucani, N.; Capozza, G.; Segoloni, E.; Volpi, G. G.; Casavecchia, P., Dynamics of the $O(^3P) + C_2H_2$ Reaction from Crossed Molecular Beam Experiments with Soft Electron Ionization Detection. *Phys. Chem. Chem. Phys.* **2014**, *16*, 10008-10022

(58) Hu, W.; Lendvay, G.; Maiti, B.; Schatz, G. C., Trajectory Surface Hopping Study of the $O(^3P)$ + Ethylene Reaction Dynamics. *J. Phys. Chem. A* **2008**, *112*, 2093

(59) Balucani, N.; Leonori, F.; Casavecchia, P.; Fu, B.; Bowman, J. M., Crossed Molecular Beams and Quasiclassical Trajectory Surface Hopping Studies of the Multichannel Nonadiabatic $O(^3P)$ + Ethylene Reaction at High Collision Energy. *J. Phys. Chem. A* **2015**, *119*, 12498-12511

(60) DeBoer, G. D.; Dodd, J. A., *Ab Initio* Energies and Product Branching Ratios for the $O+C_3H_6$ Reaction. *J. Phys. Chem. A* **2007**, *111*, 12977

(61) Savee, J. D.; Welz, O.; Taatjes, C. A.; Osborn, D. L., New Mechanistic Insights to the $O(^3P)$ + Propene Reaction from Multiplexed Photoionization Mass Spectrometry. *Phys. Chem. Chem. Phys.* **2012**, *14*, 10410

(62) Zhao, H. M.; Pan, L.; Bian, W. S., A Theoretical Study on the Reaction Mechanisms of $O(^3P)$+1-Butene. *Int. J. Quantum Chem* **2012**, *112*, 858

(63) Messaoudi, B.; Mekelleche, S. M.; Mora-Diez, N., Theoretical Study of the Complex Reaction of $O(^3P)$ with *cis*-2-Butene. *Theor. Chem. Acc.* **2013**, *132*, 1394

(64) Messaoudi, B.; Mekelleche, S. M.; Alvarez-Idaboy, J. R.; Mora-Diez, N., Theoretical Study of the Complex Reaction of $O(^3P)$ with *trans*-2-Butene. *Theor. Chem. Acc.* **2013**, *132*, 1366

(65) Zhao, H.; Bian, W.; Liu, K., A Theoretical Study of the Reaction of $O(^3P)$ with Isobutene. *J. Phys. Chem. A* **2006**, *110*, 7858

(66) Caracciolo, A.; Vanuzzo, G.; Balucani, N.; Stranges, D.; Cavallotti, C.; Casavecchia, P., Observation of H Displacement and H_2 Elimination Channels in the Reaction of $O(^3P)$ with 1-Butene From Crossed Beams and Theoretical Studies. *Chem. Phys. Lett.* **2017**, *683*, 105-111

CHAPTER 4

INFRARED STARK SPECTROSCOPY OF OH–CO: THE ENTRANCE CHANNEL COMPLEX ALONG THE OH + CO → *trans*-HOCO REACTION PATHWAY

Sequential capture of OH and CO by superfluid helium droplets leads exclusively to the formation of the linear, entrance-channel complex, OH–CO. This species is characterized by infrared laser Stark spectroscopy via measurements of the fundamental OH stretching vibration. Experimental dipole moments are in disagreement with *ab initio* calculations at the equilibrium geometry, indicating large-amplitude motion on the ground state potential energy surface. Vibrational averaging along the hydroxyl bending coordinate recovers 80% of the observed deviation from the equilibrium dipole moment. Inhomogeneous line broadening in the zero-field spectrum is modeled with an effective Hamiltonian approach that aims to account for the anisotropic molecule-helium interaction potential that arises as the OH–CO complex is displaced from the center of the droplet.

4.1 Introduction

The exothermic exchange reaction between OH and CO to give H and CO_2 is one of the most important reactions in atmospheric and combustion chemistry.[1] In both the terrestrial atmosphere[2] and high temperature combustion environments,[3] it is largely responsible for the oxidation of CO in addition to being an important sink for the OH radical. It is a prototypical example of a tetratomic "complex-forming" reaction,[4] where the "complex" corresponds to the chemically bound hydroxycarbonyl intermediate

(HOCO).[5, 6] At energies well below the exit channel barrier, HOCO dissociates to give H and CO_2 via a deep-tunneling mechanism, which was revealed by dissociative photodetachment studies of the anion ($HOCO^-$).[1, 7-9] These measurements have spurred several recent theoretical investigations of the tunneling mechanism and its mode specificity,[9-12] including full-dimensional quantum dynamics calculations.[13-14] Here we investigate the outcome of the sequential capture of OH (or OD) and CO by superfluid helium droplets and the ensuing solvent-mediated reaction using infrared (IR) laser spectroscopy.

The *trans*- isomer of HOCO has been characterized at high resolution by microwave,[15-16] far-IR,[17-18] and mid-IR spectroscopies.[19-22] While the *trans*-HOCO isomer represents the global minimum on the reactive potential energy surface,[8, 10, 23-24] other minima include the *cis*-HOCO isomer and two weakly bound linear complexes (OH–CO and OH–OC), both of which lie in the entrance valley to the reaction. Vibrational frequencies for both *trans*- and *cis*-HOCO have been obtained via anion photoelectron spectroscopy[25] and matrix isolation spectroscopy.[26-28] A rotational spectrum of *cis*-HOCO has been reported by Endo and co-workers.[16] The OH–CO complex is bound by ~320 cm^{-1} and the interconversion barrier leading to *trans*-HOCO lies ~330 cm^{-1} above the asymptotic OH + CO energy.[8, 10, 23] The OH stretch overtone spectroscopy and photodissociation dynamics of OH–CO have been extensively studied by Lester and co-workers in a series of seminal papers.[29-35] The other predicted entrance channel complex, OH–OC, has never been observed experimentally.

Helium droplets provide a cold (0.4 K)[36] liquid environment that very weakly interacts with foreign species.[37-39] The highly dissipative nature of the liquid with respect

to heat means that foreign species very quickly thermalize to the droplet temperature, such that it is possible to trap molecular systems in local minima. For example, different conformers of molecules are readily "frozen out" in helium droplets with a relative abundance that is unchanged with respect to the gas phase.[40-43] Other examples of kinetic trapping in helium droplets include the formation of the high energy cyclic isomer of $(H_2O)_6$,[44] non-equilibrium clusters of HF,[45] and pre-reactive complexes such as Cl–HCN[46] and Ga–HCN.[47] The dissipative nature of helium droplets is ideally suited for trapping entrance channel complexes along bimolecular reaction paths, such as for the OH + CO reaction.

The HOCO complex is not expected to be produced following the association reaction between OH and CO in helium droplets, because the zero-point corrected barrier in going from OH + CO to *trans*-HOCO is above the asymptotic reaction energy.[10] The internal energy of the molecular fragments is expected to be dissipated on a time scale that is fast in comparison to the time scale for complex formation in helium droplets; therefore, the *in situ* bimolecular reaction is expected to occur between monomers lacking internal energy. In the absence of tunneling, any positive barrier in the entrance channel will thereby serve to trap the system in one of the pre-reactive OHCO wells. Nevertheless, we searched for spectroscopic signals corresponding to both *trans*- and *cis*-HOCO. The search resulted in no evidence for either of these species, indicating that barriers are sufficiently high such that the reaction does not proceed in helium droplets on the time scale of the experiment (~2 ms). Instead, we find that the helium-mediated OH + CO association reaction leads exclusively to the OH–CO entrance channel

complex. We report a detailed spectroscopic analysis of this species by employing high-resolution Stark measurements in the vicinity of the fundamental OH stretching vibration.

4.2 Experimental Methods

The apparatus used for measuring helium droplet depletion spectra has been described in detail earlier,[37, 48-50] and we only include some important aspects here. Helium nanodroplets consisting of several thousand atoms are generated by expanding high pressure, low temperature helium gas through a 5 μm pinhole nozzle. The expansion is skimmed and the droplet beam passes into a pick-up chamber, which houses a pyrolysis source and pick-up cell. The pyrolysis source consists of a water cooled, resistively heated quartz tube that is used to produce the OH and OD radicals via thermal decomposition of tert-butyl hydroperoxide[51] or tert-butyl deuteroperoxide,[52] respectively (Eq. 4.1).

$$\mathrm{TBHP} \xrightarrow{\Delta} \cdot\mathrm{OH} + \cdot\mathrm{CH_3} + (\mathrm{CH_3})_2\mathrm{CO} \qquad (4.1)$$

The flow rate of precursor through the tube is adjusted to maximize the number of OH(D) doped helium droplets. The droplet beam subsequently passes through the pick-up cell, which contains a CO pressure optimized for the pick-up of one CO molecule per droplet (except for the OD–CO survey scan, for which the pressure was higher). Further downstream, the doped droplets are overlapped with the idler output from a continuous wave optical parametric oscillator (OPO).[50] Subsequently, the droplet beam is detected with a quadrupole mass spectrometer (QMS). For the zero-field spectra, the IR output from the OPO system was aligned collinearly with the droplet beam, and for the Stark spectra, the output crossed (nearly perpendicularly) the droplet beam ~30 times in a

multipass cell.[51, 53] The polarization of the laser beam can be aligned either parallel or perpendicular to the electric (or magnetic) static field axis. The Stark field is calibrated via measurements of the field induced splitting of the HCN *R*(0) line into its two ΔM_J components.[54] The separation between the Stark electrodes is found to be 3.10 ± 0.03 mm.

When the IR radiation is absorbed by the species in the helium droplet, energy transfer to the solvent occurs on a time scale that is fast in comparison to the flight time of droplets to the detector, which results in the evaporation of several hundred helium atoms. Thus, when on resonance, the ionization cross section of the droplet is smaller than when off resonance, and this photo-induced cross section reduction for ionization is detected by the QMS. The output from the QMS is processed with a lock-in amplifier (laser is amplitude modulated at ∼80 Hz) and plotted against the output from a high-precision wavemeter (repeatability ±20 MHz) to give the depletion spectra. For the species investigated here, we tuned the quadrupole to pass either ions with mass 17 (OH^+), 29 (COH^+), or 44 u (CO_2^+), which all result from the ionization induced fragmentation of OH–CO. Except for the OH–CO survey spectrum, the spectra have been normalized to laser power.

4.3 Theoretical Methods

Electronic structure computations were all carried out using the CFOUR software package.[55] Geometries, harmonic frequencies, potential energy surfaces, and dipole moment surfaces were all computed at the CCSD(T)/Def2-TZVPD level of theory. The convergence of dipole moments was tested by single point energy computations

employing Dunning's aug-cc-pVXZ basis sets.[56] Dipole moments computed using the Def2-TZVPD basis are essentially the same as those computed with the aug-cc-pVQZ basis.

To obtain the vibrationally averaged dipole moment for OH–CO, we calculate the ground state vibrational wave function in a two-dimensional representation consisting of the center of mass separation between the OH and CO fragments (R) and the angle (θ_1) between the OH bond and a vector along R. In this picture, the CO bending motion is assumed to be negligible, and the angle (θ_2) between the CO bond and the vector along R is fixed at 0° (θ_1 = 180° and θ_2 = 0° corresponds to the OH–CO equilibrium geometry). The calculation is carried out in two steps based on the Jacobi coordinate Hamiltonian, expressed in terms of R and θ_1, their conjugate momenta and the reduced mass associated with the complex μ_R.

$$H = \frac{{p_R}^2}{2\mu_R} + \frac{{j_1}^2}{2\mu_R R^2} + V(R, \theta_1) \tag{4.2}$$

First the vibrational energies and wave functions are obtained for the one-dimensional cuts through the potential in R at θ_1 = 160° and in θ_1 with R = 3.9856 Å using a discrete variable representation (DVR).[57-58] These values are chosen to be close to the maximum in the probability amplitude. A direct product basis is generated from these wave functions, and the two-dimensional Schrödinger equation is solved in this basis. The procedure closely follows the approach we used to obtain the vibrational wave functions for ICN^-.[59] In the present work, the stretch wave function is based on 500 DVR points ranging from 3.2 to 4.8 Å, while 500 DVR points based on Legendre polynomials are used to describe the bend wave function. The lowest 100 and 60 solutions to stretch and

bend Hamiltonians, respectively, are used to generate the basis for the two-dimensional calculation.

4.4 Results

A survey spectrum covering the 3500–3660 cm^{-1} region is shown in Figure 4.1, which was recorded with conditions optimized for sequential capture of OH and CO. Positive spectroscopic signal corresponds to ion current depletion in mass channel 17 u (OH^+). Other than the $Q(3/2)$ and $R(3/2)$ transitions of OH and weak features due to H_2O_2,[51, 60] one strong band is observed near 3551 cm^{-1}. The dashed lines in Figure 4.1 labeled as "OH–CO" and "OH–OC" represent harmonic band origin shifts from the OH monomer, which were computed at the CCSD(T)/Def2-TZVP level of theory. For the OH–CO complex, the computed 19 cm^{-1} red shift is in rather good agreement with the 3551 cm^{-1} band (17 cm^{-1} red shift from OH monomer), whereas a 10 cm^{-1} blue shift is predicted for the OH–OC complex. The dashed line labeled as "*trans*-HOCO" represents the experimental gas-phase band origin for the OH stretch.[22] Similar survey spectra were recorded in mass channels 29 u (HCO^+) and 44 u (OCO^+), and both contained the band at 3551 cm^{-1}. None of the survey spectra contain evidence for either the higher energy OH–OC linear complex or the covalently bound HOCO radical. Sequential capture of OH and CO by helium droplets apparently leads to the exclusive formation of the linear OH–CO entrance channel complex. The analysis of high-resolution spectra in the vicinity of the 3551 cm^{-1} band confirms this assignment.

Figure 4.2 contains several high-resolution scans (black traces) in the vicinity of the 3551 cm^{-1} band with different electric fields applied to the Stark electrodes. The

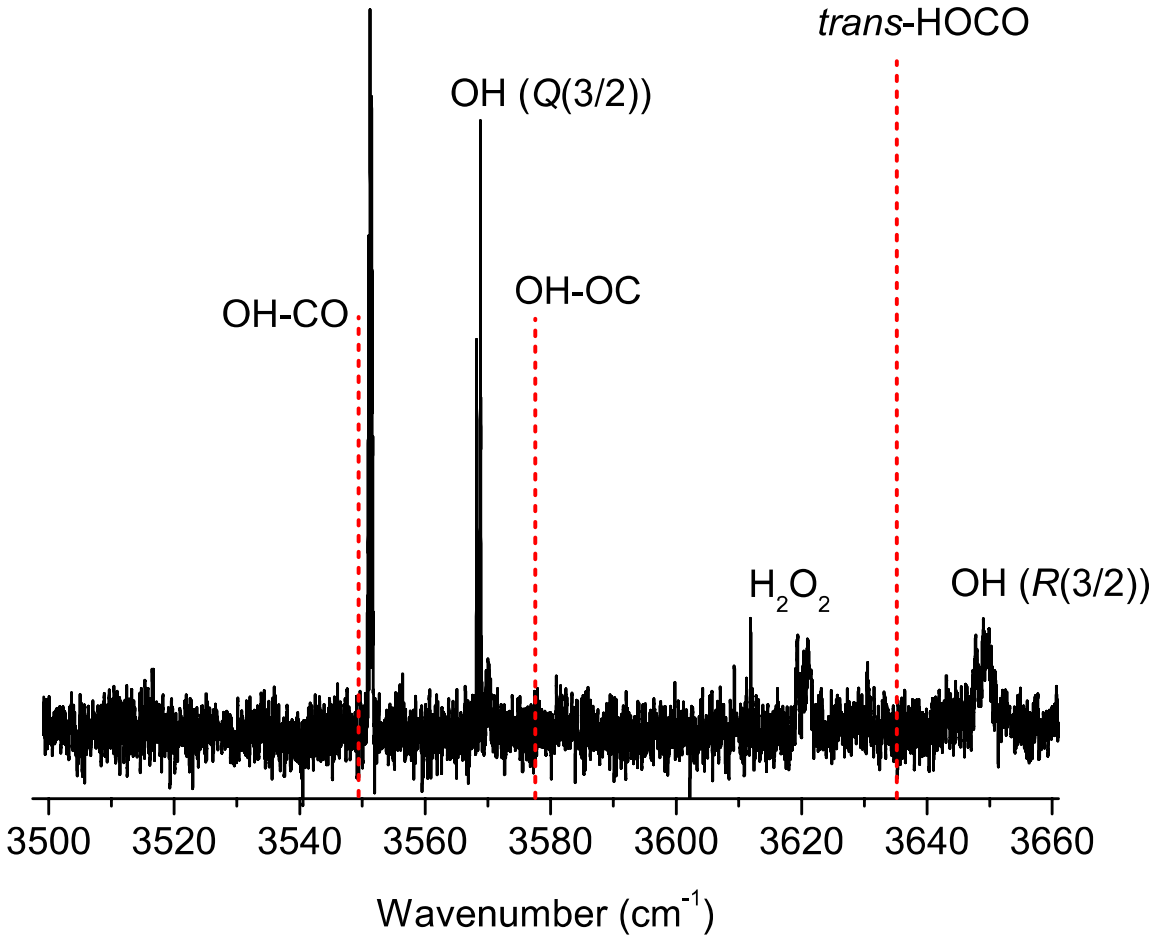

Figure 4.1: Infrared survey spectrum measured as depletion in mass channel 17 u. In addition to the rovibrational transitions associated with OH monomer and H_2O_2, a strong band centered near 3551 cm^{-1} is observed. Dashed lines labeled as OH−CO and OH−OC represent harmonic band origin shifts from OH monomer computed at the CCSD(T)/Def2-TZVP level of theory. The dashed line labeled as *trans*-HOCO represents the experimental gas-phase band origin for the OH stretch.[61]

bottom spectrum corresponds to the zero-field condition. Cursory examination of the zero-field spectrum reveals *P*, *Q*, and *R* branches. The separation between the *Q* branch and the first *P* and *R* branch transitions is approximately equal to $5B$ (~0.24 cm^{-1}), which is consistent with the half-integer J quantum numbers and the $^2\Pi_{3/2}$ electronic ground state expected for a linear complex containing the hydroxyl radical and a closed shell partner. Individual transitions are labeled in the figure with the standard convention $\Delta J(J'')$.

The effective Hamiltonian used to model the zero-field spectrum is given in Eq. 4.3, which contains terms for rigid rotation and spin-orbit coupling.[62] The tensor operators $\mathrm{T}^{\mathbf{1}}(\boldsymbol{J})$, $\mathrm{T}^{\mathbf{1}}(\boldsymbol{L})$, and $\mathrm{T}^{\mathbf{1}}(\boldsymbol{S})$ correspond to the total (less nuclear spin), orbital, and spin angular momenta, respectively. The parameters A_{SO} and B are the spin-orbit coupling constant and the rotational constant for the OH–CO complex, respectively.

$$H_0 = H_{\mathrm{SO}} + H_{rot} = A_{\mathrm{SO}}\mathrm{T}^1(\boldsymbol{L}) \cdot \mathrm{T}^1(\boldsymbol{S}) + B\ \mathrm{T}^1(\boldsymbol{J} - \boldsymbol{L} - \boldsymbol{S}) \cdot \mathrm{T}^1(\boldsymbol{J} - \boldsymbol{L} - \boldsymbol{S}) \qquad (4.3)$$

Equation 4.4 is obtained upon expanding the dot products. The p and q indices span {− 1, 0,+ 1} and are associated with laboratory-fixed and molecule-fixed components of the angular momenta, respectively.

$$\begin{aligned} H_0 = (A_{\mathrm{SO}} + 2B)T_0^1(\boldsymbol{L})T_0^1(\boldsymbol{S}) \\ + B\Bigg\{\sum_p (-1)^p T_p^1(\boldsymbol{J})T_{-p}^1(\boldsymbol{J}) + \sum_q (-1)^q T_q^1(\boldsymbol{S})T_{-q}^1(\boldsymbol{S}) \\ + T_0^1(\boldsymbol{L})T_0^1(\boldsymbol{L}) - 2T_0^1(\boldsymbol{J})\mathfrak{D}_{00}^{(1)*}T_0^1(\boldsymbol{L}) \\ - 2\sum_{p,q} (-1)^p T_p^1(\boldsymbol{J})\mathfrak{D}_{-pq}^{(1)*}T_q^1(\boldsymbol{S})\Bigg\} \\ + \sum_{q=\pm 1}\Bigg\{(-1)^q(A_{\mathrm{SO}} + 2B)T_q^1(\boldsymbol{L})T_{-q}^1(\boldsymbol{S}) \\ + (-1)^q B T_q^1(\boldsymbol{L})T_{-q}^1(\boldsymbol{L}) - 2B\sum_p (-1)^p T_p^1(\boldsymbol{J})\mathfrak{D}_{-pq}^{(1)*}T_q^1(\boldsymbol{L})\Bigg\} \end{aligned} \qquad (4.4)$$

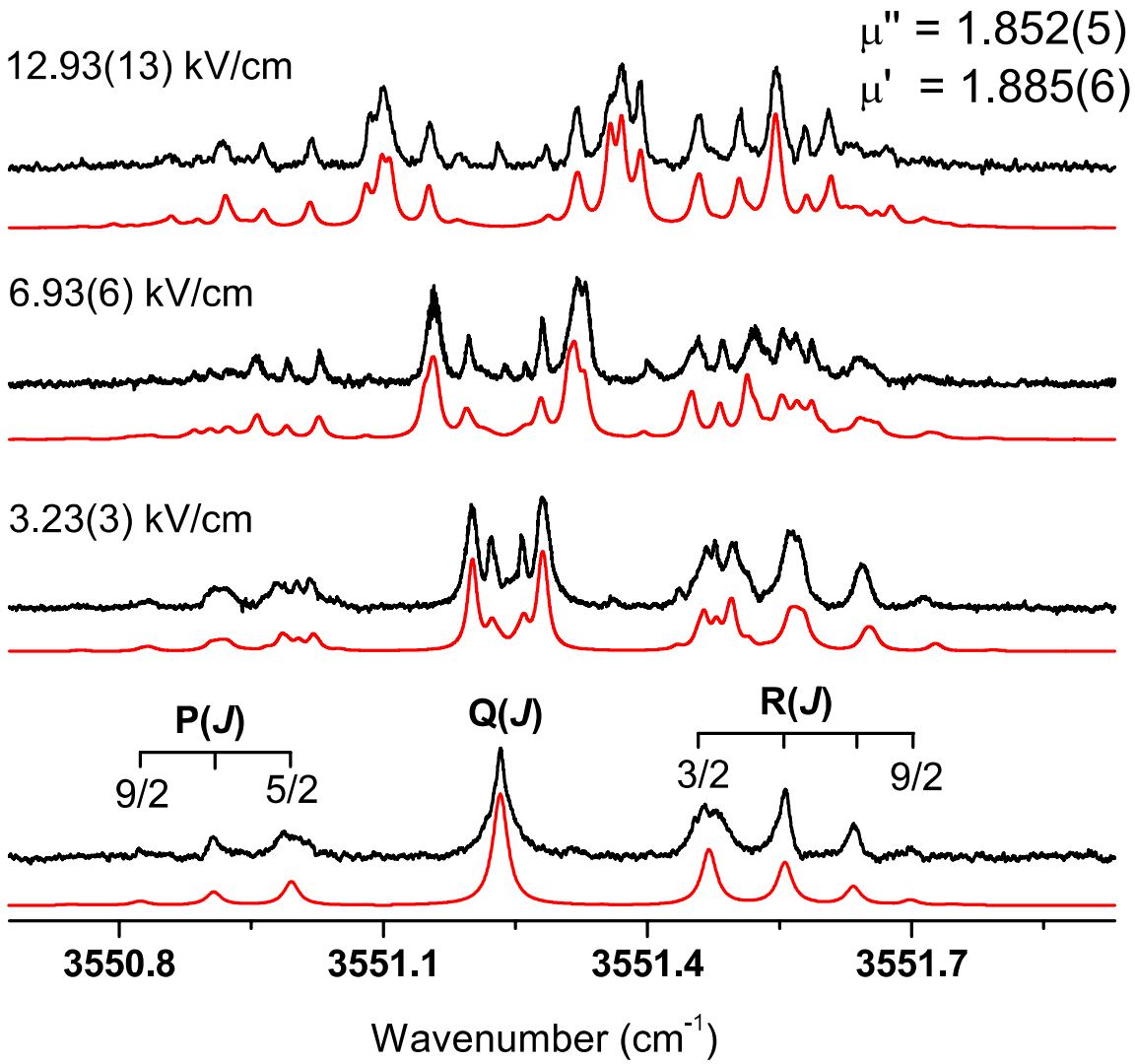

Figure 4.2: Rovibrational spectra of the OH stretch band of the linear OH−CO hydrogen bonded complex. Individual transitions are labeled above the zero-field spectrum (bottom). Infrared Stark spectra were obtained with a perpendicular laser polarization configuration and three separate static field strengths, revealing the magnitude of the permanent dipole moments in both the ground and excited vibrational states. The red traces are simulations using the effective Hamiltonian model described in the text

We chose to omit the last group of terms falling under the $q = \pm 1$ summation, because they contribute to, respectively, off-diagonal spin-orbit coupling that shifts the electronic energy independent of J, a constant contribution to the electronic energy that can be absorbed into the vibronic band origin, and an L-uncoupling interaction that mixes Π and Σ states leading to Λ-doubling. The estimated Λ-doubling is several orders smaller than the experimental line widths (~250 MHz).

The Hamiltonian matrix is represented in a Hund's case (a) primitive basis (Eq. 4.5).

$$|\eta, \Lambda; S, \Sigma; J, M_J, \Omega\rangle \tag{4.5}$$

The quantum numbers Λ, Σ, and Ω correspond to projections of the orbital (η=1), spin (S=1/2), and total angular momenta of OH–CO onto the molecular frame z-axis (q=0), respectively. M_J is the projection of the total angular momentum onto the laboratory frame Z-axis (p = 0), which is defined as the axis of the static electric or magnetic field applied to the laser interaction region. Matrix elements in the primitive case (a) representation are derived by applying the Wigner-Eckart theorem and standard angular momentum algebraic manipulations (Eq. 4.6).[62]

$$\begin{aligned}\langle -|H_0|-'\rangle = \Bigg\{ & \{(A_{\mathrm{SO}} + 2B)\Lambda\Sigma + B[J(J+1) + S(S+1) + \Lambda^2 - 2\Omega^2]\}\delta_{\Omega'\Omega}\delta_{\Sigma'\Sigma} \\ & - 2B\sum_{q=\pm 1}(-1)^{J-\Omega+S-\Sigma}[S(S+1)(2S+1)]^{\frac{1}{2}}[J(J+1)(2J \\ & + 1)]^{\frac{1}{2}}\begin{pmatrix} J & 1 & J \\ -\Omega & q & \Omega' \end{pmatrix}\begin{pmatrix} S & 1 & S \\ -\Sigma & q & \Sigma' \end{pmatrix}\Bigg\}\delta_{\eta'\eta}\delta_{\Lambda'\Lambda}\delta_{S'S}\delta_{J'J}\delta_{M'M}\end{aligned} \tag{4.6}$$

The matrix elements given in Eq. 4.6 are almost completely diagonal, except for the term that falls under the q=±1 summation. This term corresponds to an off-diagonal spin-rotation contribution to the energy that is expected to be small for J levels populated at

0.35 K; for example, it has a selection rule equal to $\Delta\Omega = \Delta\Sigma = \pm 1$, and therefore couples different spin-orbit manifolds that are separated by ~140 cm^{-1}.

In an *ad hoc* manner, we include in the Hamiltonian matrix a single quadratic centrifugal distortion term that is diagonal in all quantum numbers, i.e., $-D_J J^2(J+1)^2$. We find this to be the simplest way to model the *J*-dependence of the molecule-helium interaction potential, which is expected to become more anisotropic with increasing *J*.[63] Unlike the typical definition that applies to gas-phase molecules, the centrifugal distortion term used here models the increase in the solvent-solute effective moment of inertia as *J* increases. The Hamiltonian matrices are diagonalized for both the ground and excited vibrational states. The spin-orbit coupling constant, A_{SO}, is set equal to the OH monomer value (−139.05 cm^{-1}), and the *B* and D_J constants are allowed to differ in the ground and excited vibrational manifolds.

The transition dipole moment operator projected onto the laser polarization axis and its matrix elements in the primitive case (a) basis are given in Eqs. 4.7 and 4.8, respectively.

$$M = -\mathbf{T^1}(\boldsymbol{\mu}_t) \cdot \mathbf{T^1}(\boldsymbol{E}_{laser}) = -\sum_{p,q=-1}^{1} (-1)^p \mathfrak{D}^{(1)*}_{pq} T^1_q(\boldsymbol{\mu}_t) T^1_{-p}(\boldsymbol{E}_{laser}) \tag{4.7}$$

$$\langle -|M|-'\rangle = -\delta_{\Lambda'\Lambda}\delta_{\Sigma'\Sigma}\delta_{\eta'\eta}\delta_{S'S} T^1_0(\boldsymbol{\mu}_t)(-1)^{M-\Omega}[(2J'+1)(2J+1)]^{\frac{1}{2}} \begin{pmatrix} J & 1 & J' \\ -\Omega & 0 & \Omega \end{pmatrix} \sum_{p=-1}^{1} (-1)^p T^1_{-p}(\boldsymbol{E}_{laser}) \begin{pmatrix} J & 1 & J' \\ -M & p & M' \end{pmatrix} \tag{4.8}$$

The summation over the *p* index in Eq. 4.8 allows for the prediction of spectra obtained with either parallel, perpendicular, or random laser electric field polarizations relative to the lab-frame Z-axis. The $\boldsymbol{M}$ matrix is transformed via the matrix operation, $\boldsymbol{U}_e^{\dagger}\boldsymbol{M}\boldsymbol{U}_g = \boldsymbol{I}$, where $\boldsymbol{U}_g$ and $\boldsymbol{U}_e$ are the eigenvector matrices for the ground and excited vibrational

levels, respectively. The elements of the intensity matrix, $\boldsymbol{I}$, correspond to $\sqrt{\boldsymbol{I_{ij}/w}}$, where $\boldsymbol{I_{ij}}$ is the intensity of the transition from the j^{th} ground-state level to the i^{th} excited-state level, and w is a Boltzmann weight with T_{rot} = 0.35 K. The simulation of the zero-field spectrum is shown as the red trace along the bottom of Figure 4.2, and the best fit band origin along with the rotational and centrifugal distortion constants are given in Table 4.1.

We note that the simulations assume a $^2\Pi_{3/2}$ electronic ground state for the spectral carrier, which is consistent with computations and previous OH stretch overtone spectroscopy of the OH–CO complex.[29-30] We measured similar spectra for OD + CO. The survey scan (with higher CO pressure than for OH + CO) reveals bands that correspond to OD–CO and most likely OD–$(CO)_2$ (see Figure A4.1 of the appendix), while there is no evidence for OD–OC. The high-resolution scan of the OD–CO band reveals a similar structure to that of OH–CO (see Figure A4.2 of the appendix).

The ground state rotational constants for OX–CO complexes are reduced to ~50% of their gas phase values, which is relatively similar to other helium-solvated rotors with rotational constants of similar magnitude.[37] The solvent contribution to the effective moment of inertia arises from the anisotropy in the He–(OX–CO) interaction potential, resulting in a renormalization of the rotational constant in going from the gas phase to liquid helium.[64] The vibrational red shift from OX monomer is 17.27 cm^{-1} for OH–CO, 14.82 cm^{-1} for OD–CO, and 19.4 cm^{-1} for OD–$(CO)_2$. For comparison, the gas phase overtone (ν = 2-0) red shifts divided by two are 14.8 cm^{-1} for OH–CO and 13.0 cm^{-1} for OD–CO, which are less than those observed here for the fundamental bands due to vibrational anharmonicity. Although the gas-phase fundamental OX stretching bands

TABLE 4.1. Spectroscopic constants for OH−CO and OD−CO (in cm^{-1}).

	ν_0	B'' (Helium)	B'' (Gas)[a]	B'	μ'' (D)	μ' (D)
OH–CO	3551.233(1)	0.0480(5)	0.0972(1)	0.0478(3)	1.852(5)	1.885(6)
OD–CO	2616.478(2)	0.0490(7)	0.0961(5)	0.0481(7)	1.88(8)	1.94(5)

[a] From IR photodissociation spectra of the $2\nu_1$ bands; Refs. 32 and 33.

have not been observed, on the basis of an empirically observed dependence of the solvent shift on the complexation induced red shift of OX stretches,[37] we estimate the solvent shifts for OX–CO complexes to be ∼2 cm^{-1} to the red.

The Stark effect is accounted for by appending the Stark operator[62] (Eq. 4.9) to the zero-field effective Hamiltonian. Here, the tensor operators, $\mathbf{T^1}(\boldsymbol{\mu})$ and $\mathbf{T^1}(\boldsymbol{E})$ correspond to the molecular dipole moment and the external static Stark field, respectively.

$$\begin{aligned} H_{Stark} &= -\boldsymbol{T^1}(\boldsymbol{\mu}) \cdot \boldsymbol{T^1}(\boldsymbol{E}) = -\sum_{p,q=-1}^{1} (-1)^p \mathfrak{D}_{pq}^{(1)*} T_q^1(\boldsymbol{\mu}) T_{-p}^1(\boldsymbol{E}) \\ &= -T_0^1(\boldsymbol{\mu}) T_0^1(\boldsymbol{E}) \mathfrak{D}_{00}^{(1)*} \end{aligned} \tag{4.9}$$

Matrix elements of the Stark operator in the primitive case (a) basis are given in the following equation, where the magnitude of the vibrationally averaged dipole moment and the applied electric field are $|\mu|$ and $|E|$, respectively.

$$\begin{aligned} \langle -|H_{Stark}|-' \rangle = -|\mu||E|(-1)^{M-\Omega}[(2J'+1)(2J \\ +1)]^{\frac{1}{2}} \begin{pmatrix} J & 1 & J' \\ -\Omega & 0 & \Omega' \end{pmatrix} \begin{pmatrix} J & 1 & J' \\ -M & 0 & M' \end{pmatrix} \delta_{\Lambda'\Lambda} \delta_{\Sigma'\Sigma} \delta_{\eta'\eta} \delta_{S'S} \end{aligned} \tag{4.10}$$

Stark spectra acquired at three separate field strengths are shown in Figure 4.2 along with simulations, from which the magnitude of the permanent electric dipole moments in the ground and excited vibrational states are extracted. The Stark spectra were recorded with a perpendicular laser polarization configuration relative to the applied electric field. The agreement between experiment and simulation is generally excellent when the zero-field rotational constants are retained and the dipole moments are set equal to μ″ = 1.852(5) and μ′ = 1.885(6) D. The error bars are largely due to the uncertainty in the applied field strength. The vibrationally averaged induced dipole moment upon OH + CO complexation is ∼0.1 D.

4.5 Discussion

Sequential capture and solvation of OH and CO by helium droplets leads to the exclusive formation of the OH–CO linear complex, as confirmed by IR spectroscopy in the fundamental OH stretching region. We find no evidence for the formation of either *cis*- or *trans*-HOCO. This observation is consistent with estimates of the OH–CO → *trans*-HOCO entrance channel barrier from kinetics studies, namely, 140–315 cm^{-1}.[65-66] In agreement with these experimental estimates, zero-point energy corrected *ab initio* calculations predict the barrier to be 330 cm^{-1} above the asymptotic OH + CO energy.[8, 10, 23-24] Furthermore, and perhaps surprisingly, we find no evidence for the OH–OC complex, which is predicted by ab initio theory to be bound by ∼160 cm^{-1} and separated from the OH–CO complex by a barrier of similar size.[24, 29] It seems possible that as OH and CO approach within a helium droplet, long-range forces along the potential valley pre-orient the complex into the more electrostatically favorable OH–CO configuration and funnel the system into the OH–CO minimum, precluding the formation of OH–OC. An electrostatic pre-orientation mechanism was similarly invoked to rationalize the helium-assisted trapping of linear $(HCN)_n$ clusters upon sequential addition of HCN to droplets containing the $(HCN)_{n-1}$ species.[67] To test the feasibility of this mechanism, we have computed barrier heights along the OH–OC↔OH–CO interconversion pathway as a function of the intermolecular separation, R (Figure A4.3 of the appendix). As is evident from the potential slice shown in Figure 4.3 (R = 4 Å), interconversion between linear complexes largely involves motion along the θ_2 coordinate, i.e., the internal rotation of the CO moiety. Computations find the OH–CO → OH–OC interconversion barrier to be ∼3 kT at R = 20 Å, whereas the barrier in the reverse direction is ∼0.7 kT. This

theoretical result implies that the long-range reorientation of the complex into the more electrostatically favorable OH–CO configuration will have the effect of biasing the outcome of cluster formation events, which is consistent with the experimental observation.

The OH–CO experimental dipole moment for the ground vibrational state is 1.852(5) D. Computations at the CCSD(T)/aug-cc-pVQZ level of theory predict an equilibrium dipole moment equal to 2.185 D, which differs from the experimental value by 0.333 D. An error of this magnitude is not expected at this level of electronic structure theory, as the dipole moment operator is a sum of one-electron operators and is easily converged with increasing level of theory and basis set size. We have confirmed the convergence of the computed dipole moment at the equilibrium geometry (e.g., at the CCSD(T)/aug-cc-pVTZ level, $\mu = 2.186$ D), and we therefore take the observed difference as a relatively good measure of the deviation between the experimental dipole moment and the gas-phase equilibrium value. The experimental measurement necessarily probes the expectation value of the permanent dipole moment, and vibrational averaging must be taken into account. Moreover, it is necessary to assess the extent by which the helium solvent contributes to the measured dipole.

Miller and co-workers reported an electrostatic elliptical cavity model to estimate the dipole induced polarization of the helium solvent, which leads to a modification of the measured dipole moment: $\mu_{He} = \mu_{gas} + \mu_{ind}$.[54] The model was found to quantitatively reproduce the observed dipole change for both HCN and HCCCN in going from the gas phase to helium droplets. Using the elliptical cavity model, we estimate the magnitude of the induced moment to be $|\mu_{ind}| \lesssim 0.01$ D (the sign of the induced moment is negative).

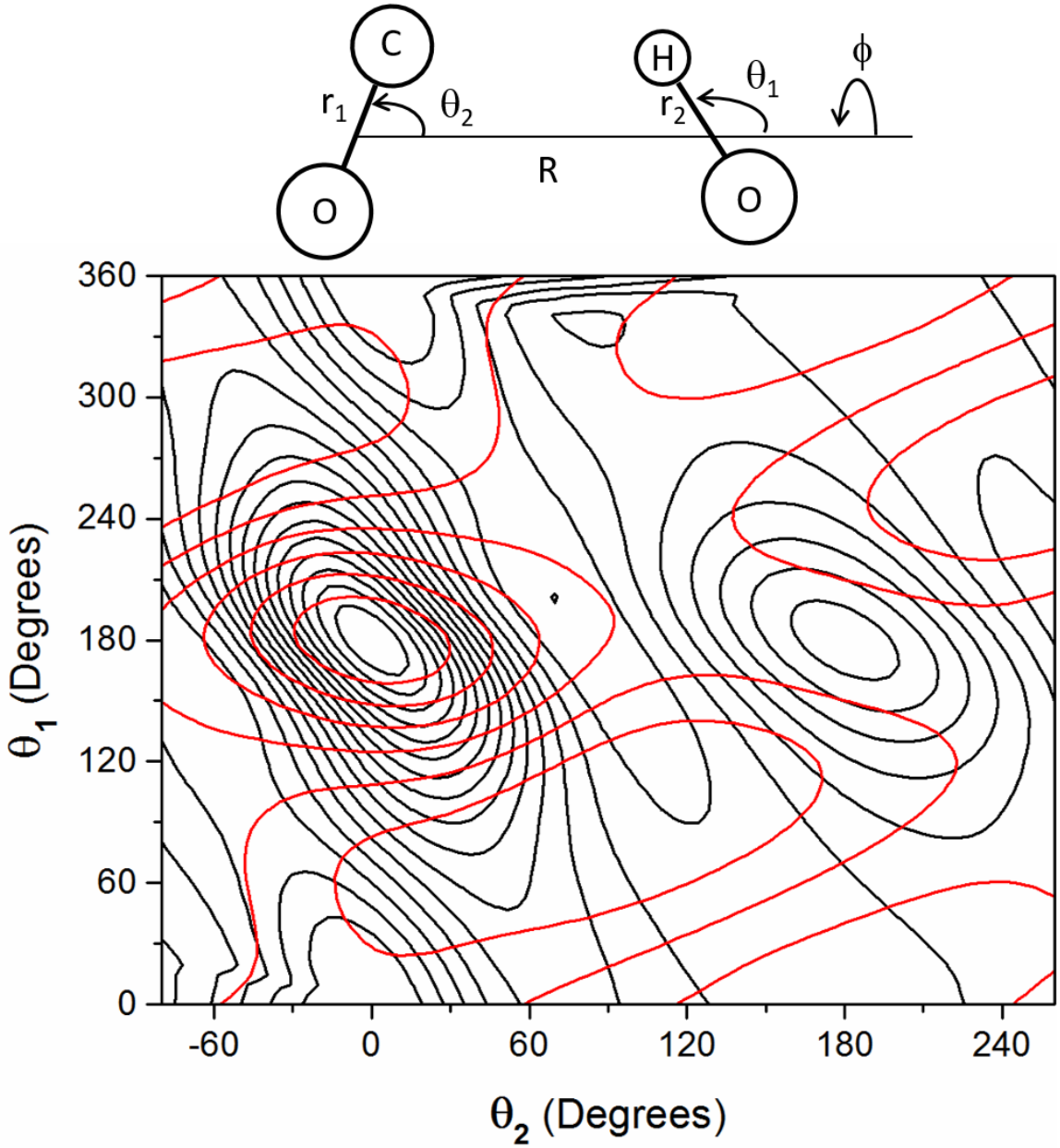

Figure 4.3: Two-dimensional slice of the OH−CO intermolecular potential energy surface (black) and dipole moment surface (red). The intermolecular separation, *R*, is fixed at 4.0 Å, which is approximately the optimal value for both the OH−CO (θ_1=180º, θ_2=0º) and OH−OC (θ_1=180º, θ_2=180º) linear configurations. The energy contours range from 0 to 800 cm^{-1} (50 cm^{-1} increments) where the zero is relative to the contour centered around the OH−CO complex. The dipole contours range from 1.5 to 2.1 D (0.1 D increments). The dipole contour centered around the minimum energy configuration is 2.1 D.

Therefore, on its own, the solvent polarization effect cannot account for the 0.333 D discrepancy between the experimentally measured and computed (equilibrium) dipoles.

The most likely source of vibrational averaging is large-amplitude intermolecular motion about the two in-plane angles (θ_1 and θ_2), as shown in Figure 4.3. The black contours (50 cm^{-1}) represent a slice of the CCSD(T)/Def2-TZVPD potential energy surface for $|\vec{R}|$=4.0 Å. This combination of basis set and level of theory similarly gave a 2.185 D dipole moment at the equilibrium OH–CO geometry (θ_1, θ_2) = (180°, 0°). The projection of the dipole vector onto $\vec{R}$ is shown as the red contours (0.1 D). The largest variation in the dipole occurs for motion along θ_1, which is expected because this internal coordinate corresponds to the large-amplitude bending motion of the lighter and more polar hydroxyl moiety (1.62 D dipole moment; B_0 = 18.55 cm^{-1}).

We chose both one-dimensional (Figure 4.4; θ_1 scanned, R = R_{mp} = 3.9856 Å) and two-dimensional (scanning both θ_1 and R) vibrational averaging schemes, which are carried out according to the procedures described in the theoretical methods section (more information can be found in the appendix; Figures A4.4–A4.8). Upon vibrational averaging about the θ_1 in-plane angle (R is fixed at its most probable value, R_{mp}), we obtain a 0.2638 D reduction for the dipole projected onto $\vec{R}$. A relatively small additional reduction (0.007 D) is obtained via the 2D averaging scheme. About 80% of the difference between the experimental $\langle\mu\vec{R}\rangle$ and *ab initio* $\mu_e$can already be accounted for by simply averaging over the large-amplitude bending motion of the hydroxyl moiety, which is clearly the leading effect. We estimate that the majority of the remaining difference is likely due to a combination of vibrational averaging due to OH stretching and bending motion of the heavier and less polar CO moiety.

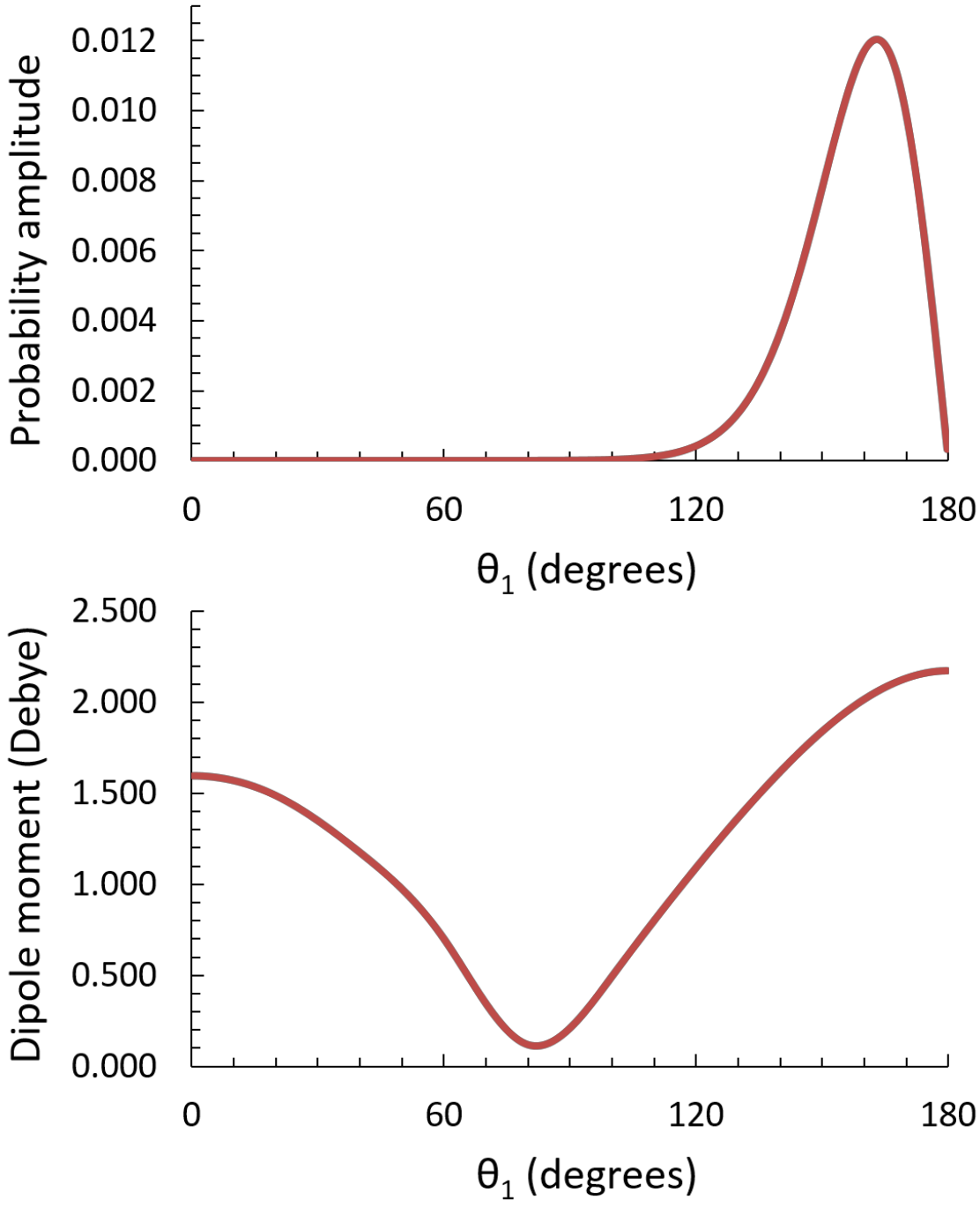

Figure 4.4: (Top frame) Probability amplitude for rotation about the θ_1 coordinate, showing the most probable value at ~160º. (Bottom frame) Projection of the dipole moment onto $\vec{R}$ as a function of θ_1. The intermolecular separation is set to the most probable value of R (3.9856 Å).

The zero-field spectrum is shown in greater detail in Figure 4.5 (black trace), which reveals substantial broadening of the $P(5/2)$ and $R(3/2)$ transitions (~1.2 GHz). The other *P*- and *R*-branch transitions exhibit slightly asymmetric line shapes shaded towards the vibrational band origin. Moreover, the base around the *Q*-branch is broadened. These broadening effects are not reproduced in simulations of the zero-field spectrum (red trace), which assume a transition-independent Lorentzian line shape of 250 MHz. We analyze this broadening in terms of the anisotropic solvent-solute interaction potential, which leads to *J*-dependent inhomogeneous broadening. Several authors have discussed potential sources of inhomogeneous broadening due to finite droplet size effects and the distribution of droplet sizes in the beam.[68-75] Experimental evidence for some of the proposed inhomogeneous broadening mechanisms has been reported,[69, 71, 73-74, 76] such as the observation of the simultaneous excitation of translational motion (3D harmonic oscillator type states) and tunneling inversion in helium-solvated ammonia.[76] An early and relevant example of finite size effects in rovibrational spectra was reported by Nauta and Miller, who observed a zero-field splitting of the HCN $R(0)$ transition into (at least what appeared to be) its ΔM_J components.[69] They discussed the mechanism of this solvent-induced splitting in analogy to the Stark effect, for which a field strength of 4.5 kV/cm ($\mu \cdot E = 0.23$ cm^{-1}) leads to a similar splitting (~200 MHz) for the isolated species. The origin of this effect was posited as being due to the anisotropic nature of the molecule-helium interaction potential when the molecule is displaced from the center of the droplet.

In a seminal paper by Lehmann,[68] a comprehensive overview of various inhomogeneous broadening mechanisms was reported along with rigorous calculations of

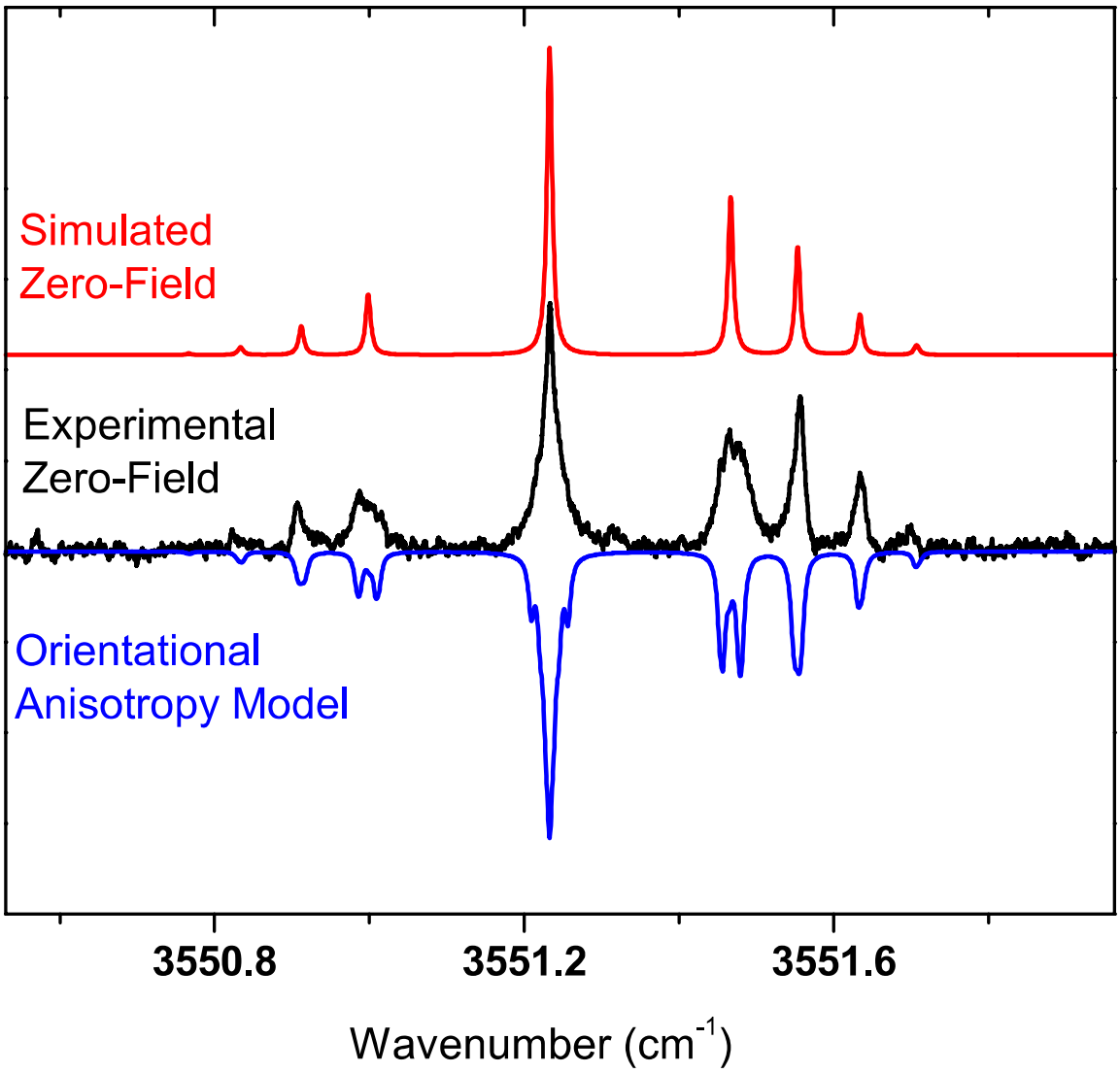

Figure 4.5: Zero-field OH stretch rovibrational spectrum of the linear OH−CO complex (black). Simulations are shown that employ the zero-field Hamiltonian (red) and orientational anisotropy models (blue). In both simulations, transitions are convoluted with Lorentzian functions having 250 MHz full-width at half maximum line widths.

the magnitude and expected importance of each. In this work, Lehmann computed the molecule-helium interaction potential, translational states, and radial distribution function for an HCN solute in a 3 nm diameter helium droplet. The long-range dispersion and induction interactions between the solute and the helium were found to lead to an anisotropic interaction potential. For example, as the HCN impurity approaches the surface of the droplet, the alignment of the molecular dipole parallel to the surface results in a larger dipole-induced polarization of the solvent, in comparison to a perpendicular alignment. The interaction potential can be expanded in Legendre polynomials (Eq. 4.11), where θ is defined as the angle between the symmetry axis of the solute and the displacement vector connecting the solute's center of mass to the center of the droplet, which has a normalized magnitude equal to r.

$$\Delta E(r,\theta) = \sum_n c_n(r) P_n(\cos\theta) \tag{4.11}$$

For HCN at its most probable normalized displacement (0.4), the first four coefficients in the expansion are 0.43, 0.0036, 0.0098, and 0.000 17 cm^{-1} for n = 0–3, respectively.[68] The $P_0(\cos\theta)$ term acts as a confining potential that keeps the HCN solute near the center of the droplet, whereas the anisotropic $P_{1,2,3}(\cos\theta)$ terms couple the rotational and translational motions of the solute and therefore provide a mechanism for *J*-dependent inhomogeneous line broadening.[68]

We have attempted to model the effect of the aforementioned broadening source by appending a single additional term to our effective zero-field Hamiltonian. However, for simplicity, we have neglected the coupling of OH–CO rotational angular momentum to its (translational) orbital angular momentum within the droplet, although the machinery necessary to do so for closed-shell linear molecules has been reported by

Lehmann.[68] We instead model the problem approximately by treating the coupling of radial motion within the droplet to molecular rotational motion. The anisotropic part of the interaction potential is written simply as $V' = c_1(r)\mathfrak{D}_{00}^{(1)*} + c_2(r)\mathfrak{D}_{00}^{(2)*}$, where the higher-order terms in the potential expansion are assumed to be negligible. Matrix elements of the anisotropic potential are derived for the primitive case (a) representation (Eq. 4.12).

$$\begin{aligned}\langle -|V'|-'\rangle = {} & (-1)^{M-\Omega}[(2J'+1)(2J \\ & +1)]^{\frac{1}{2}} \left\{\langle c_1(r)\rangle \begin{pmatrix} J & 1 & J' \\ -\Omega & 0 & \Omega' \end{pmatrix}\begin{pmatrix} J & 1 & J' \\ -M & 0 & M' \end{pmatrix}\right. \\ & \left. + \langle c_2(r)\rangle \begin{pmatrix} J & 2 & J' \\ -\Omega & 0 & \Omega' \end{pmatrix}\begin{pmatrix} J & 2 & J' \\ -M & 0 & M' \end{pmatrix}\right\} \delta_{\Lambda'\Lambda}\delta_{\Sigma'\Sigma}\delta_{\eta'\eta}\delta_{S'S}\end{aligned} \tag{4.12}$$

The *M* quantum number is now defined as the projection of the total angular momentum (less nuclear spin and translational orbital angular momenta) onto the displacement vector connecting the center of the droplet and the OH–CO center of mass.

In order to qualitatively reproduce the line broadening in the *P*(5/2), *R*(3/2), and *Q*-branch regions of the spectrum, the $\langle c_2(r)\rangle$ term must be approximately equal to the rotational constant (0.048 cm^{-1}). The blue spectrum in Figure 4.4 is a simulation using $\langle c_2(r)\rangle = B$ and $\langle c_1(r)\rangle = \langle c_2(r)\rangle/3$. The simulation is carried out with a random laser polarization configuration relative to the quantization axis, which is randomly oriented in the laboratory frame of reference. The splitting observed in the *P*(5/2), *R*(3/2), and *Q*-branch transitions is strongly affected by the $\langle c_2(r)\rangle\mathfrak{D}_{00}^{(2)*}$ anisotropy term, and with the aforementioned parameters, the model reproduces quite well the qualitative widths of these features. We find that upon reducing the value of $\langle c_2(r)\rangle$ to that computed for HCN (~0.014 cm^{-1}),[68] the splitting due to orientational anisotropy cannot account for the experimentally observed line widths and substructure (e.g., the simulated *R*(5/2) width is

now only ~500 MHz), suggesting a more anisotropic interaction between OH–CO and $(He)_N$, in comparison to HCN–$(He)_N$.

In the absence of an (OH–CO)–$(He)_N$ interaction potential, we are only able to say that the simulation can be made to qualitatively reproduce the experimental zero-field broadening. We emphasize however, to assess whether or not the values of $\langle c_1(r)\rangle$ and $\langle c_2(r)\rangle$ used in the model are realistic, future calculations of the molecule-helium potential will be required, along with a complete treatment of angular momentum coupling that includes the orbital motion of the impurity about the center of the droplet. Other broadening sources, such as translational-rotational coupling due to hydrodynamic effects are also predicted to be *J*-dependent.[68] These effects along with a realistic averaging over the spread of droplet sizes must also be accounted for to quantitatively model the broadening observed here for OH–CO. A future paper on this subject will address these issues along with a quantitative analysis of similar inhomogeneous broadening observed in the zero-field spectrum of HCCCN. We note in closing that like other systems studied in helium droplets,[77-79] inhomogeneous line broadening of low-*J* transitions appears to be largely quenched upon application of a Stark field that produces a $\mu \cdot E$ interaction on the order of ~*B*. These phenomena have yet to be explained.

4.6 Summary

Sequential capture and solvation of OH and CO by helium droplets lead to the exclusive formation of the OH–CO linear complex, as confirmed by IR spectroscopy in the fundamental OH stretching region. A systematic spectroscopic study is reported for the OH–CO hydroxyl stretching band near 3551 cm^{-1}. The ground state rotational

constant is observed to be reduced by about a factor of two in comparison to the gas-phase value. Stark spectra reveal the vibrationally averaged dipole moments in the ground and excited vibrational states to be 1.852(5) and 1.885(6) D, respectively. The computed equilibrium dipole moment at the CCSD(T)/aug-cc-pVQZ level of theory is 0.333 D larger than the experimental ground state value. Nearly 80% of this difference can be accounted for by averaging the dipole moment over the OH intermolecular bending coordinate on the *A′* potential surface. Zeeman spectra reveal the magnitude of *g*-factors to be the same as those expected for the isolated OH system, thereby indicating that, within the experimental error, neither complexation with CO nor solvation in superfluid helium results in any quenching of the orbital angular momentum.

Strongly *J*-dependent inhomogeneous line broadening effects are observed in the zero-field rovibrational spectrum. We have attempted to simulate this broadening via the application of a model that partially accounts for the coupling of translational and rotational motions that arise from the anisotropic nature of the molecule-helium interaction potential as the impurity is displaced from the droplet's center of mass. Qualitative broadening features are reproduced, although it is not yet clear if the parameters in the model are physically reasonable, the confirmation of which will require a calculation of the (OH–CO)–$(He)_N$ interaction potential averaged over both low-lying electronic states (*A′* and *A″)*.

4.7 Appendix

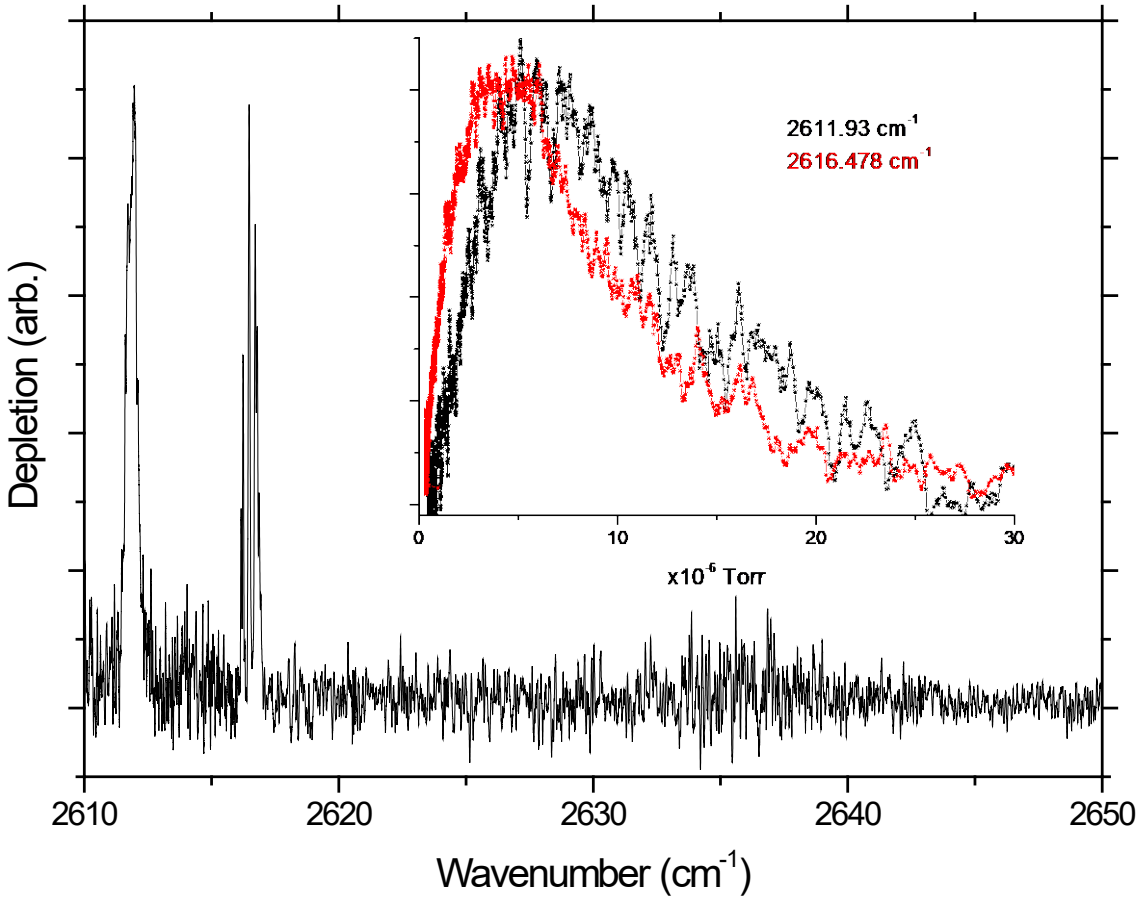

Figure A4.1: Survey spectrum of OD + CO. The pick-up cell pressure of CO was somewhat higher than for the analogous scan as shown in Figure 4.1 (main text). The peak at 2611.93 cm^{-1} optimizes at twice the pressure needed to optimize the OD-CO band at 2616.48 cm^{-1}. This pressure dependence indicates that the 2611.93 cm^{-1} band is due to the OD-$(CO)_2$ complex (see inset for pressure dependence curves).

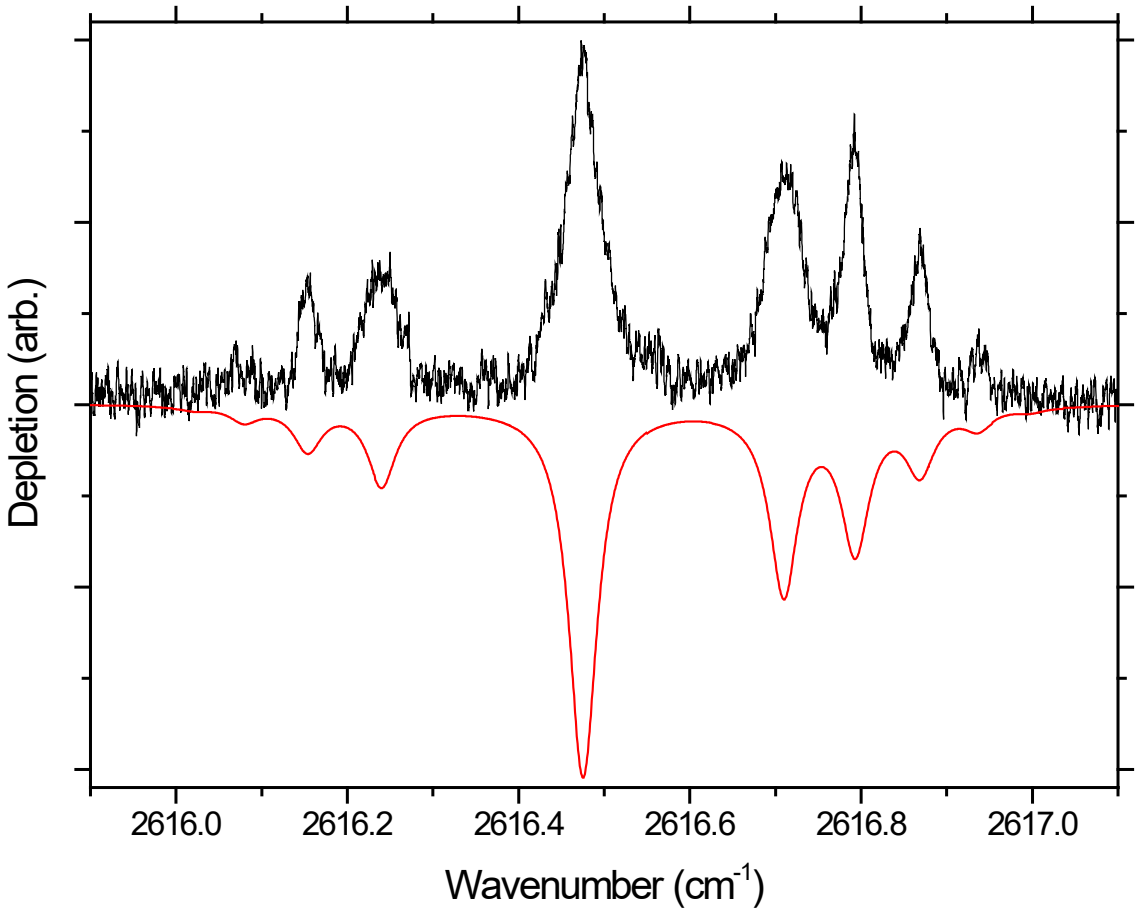

Figure A4.2: High resolution experimental and simulated spectra of OD-CO at full power (collinear). The spectrum is saturated with a *Q* branch peak that is about factor of 2 broader than that observed under non-saturating conditions.

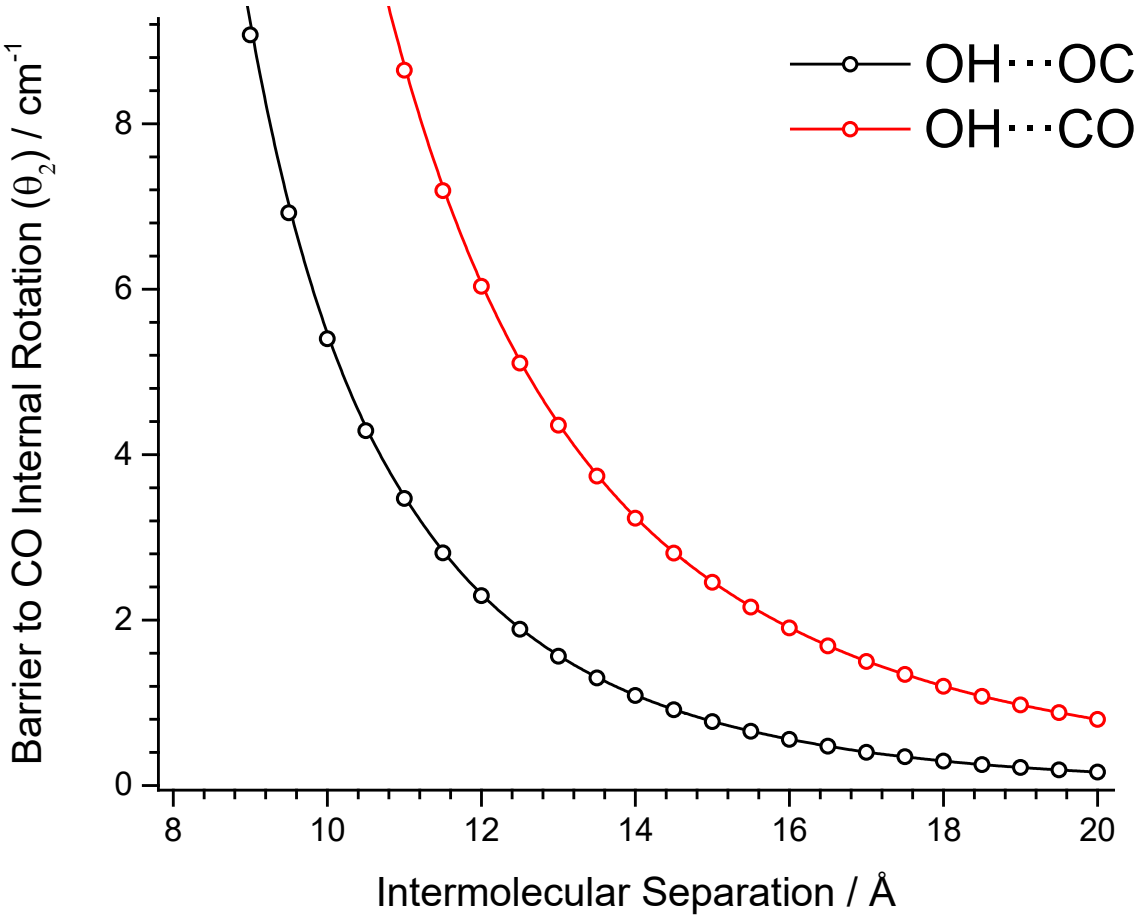

Figure A4.3: Interconversion barrier between OH−CO and OH−OC linear isomers as a function of the separation between OH and CO centers of mass. The red and black curves are associated with barrier heights for interconversion starting from OH−CO and OH−OC complexes, respectively.

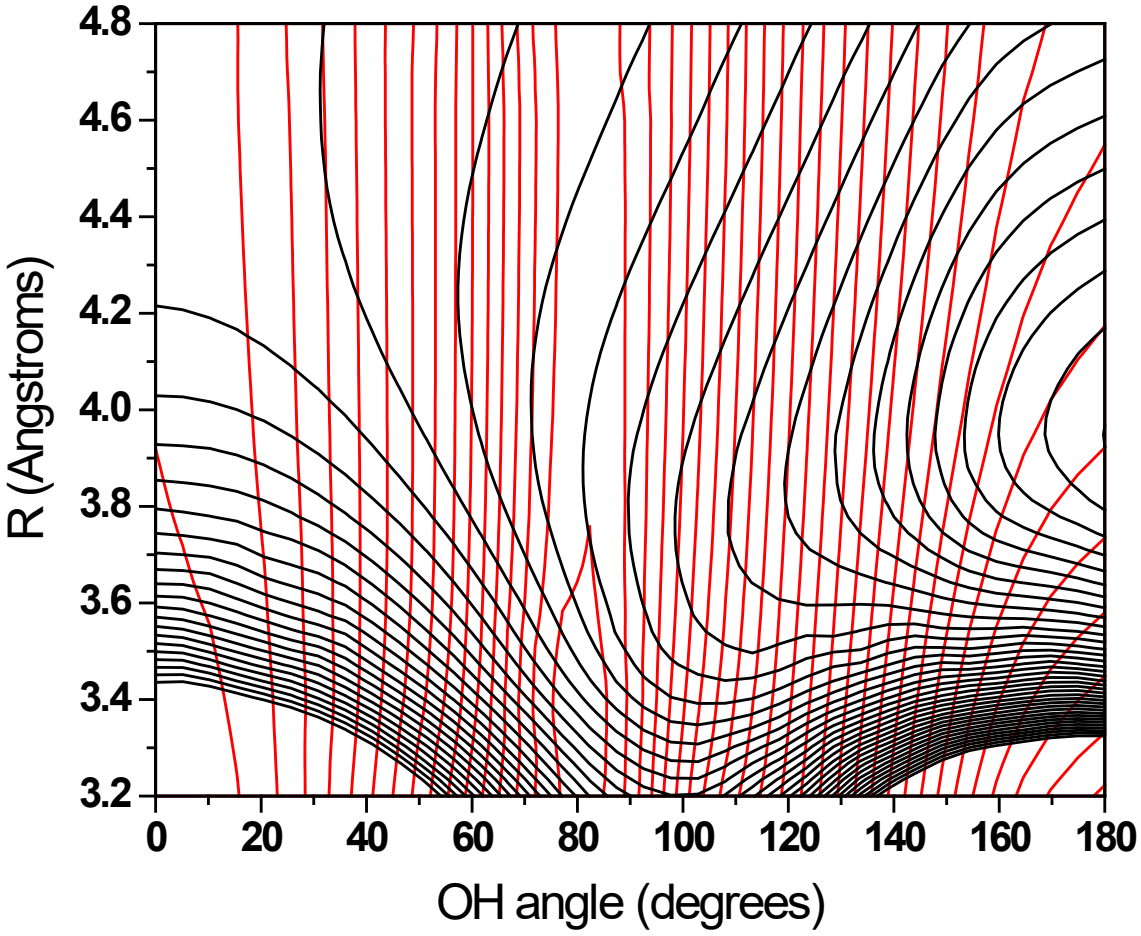

Figure A4.4: Two-dimensional intermolecular potential energy surface (black) (R, θ_1) used for the two dimensional vibrational averaging of the dipole moment projection (red) (see text). Energy contours relative to the OH−CO complex (θ_1=180º) are from 0 to 1750 cm^{-1} in 50 cm^{-1} increments. The dipole moment surface (red) has a range of 0 to 2.7 D with increments of 0.1 D. The zero of the dipole surface is the seam at θ_1=80º.

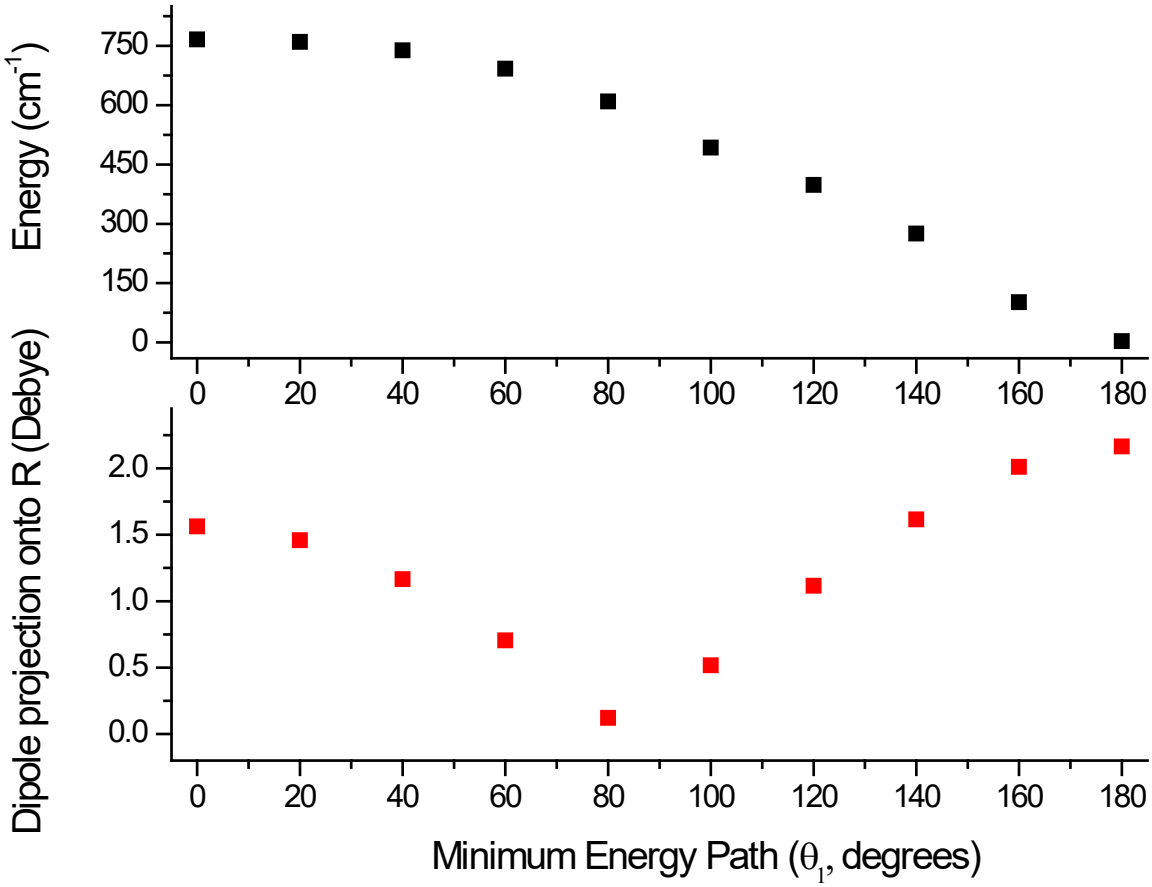

Figure A4.5: Minimum energy path for hydroxyl radical rotation (black) and corresponding dipole moment projection onto the intermolecular axis connecting OH and CO centers of mass.

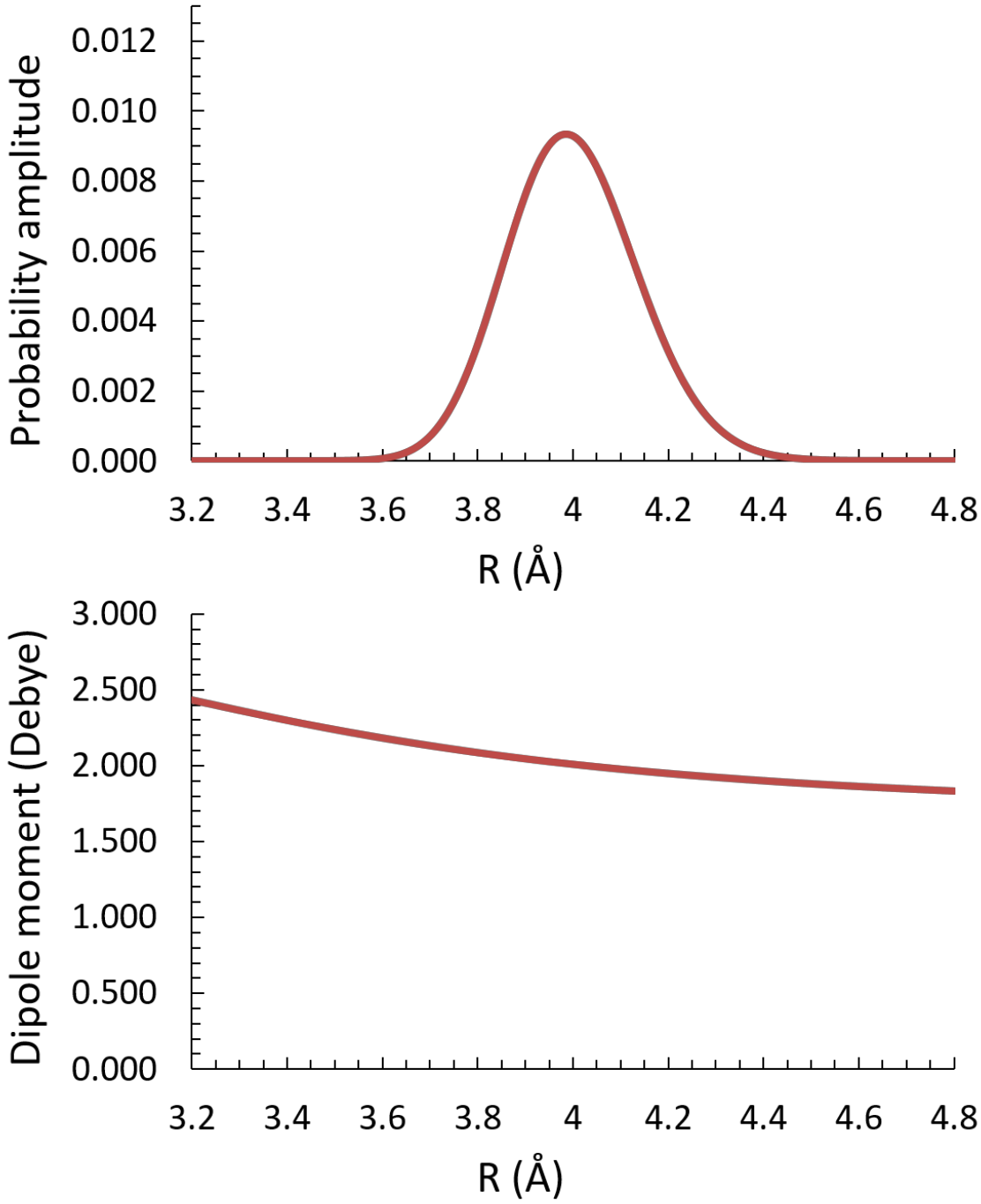

Figure A4.6: (Top frame) Probability amplitude for intermolecular stretching along the R coordinate, showing the most probable value at ~4.0 Å. (Bottom frame) Projection of the dipole moment onto $\vec{R}$ as a function of R. The θ_1 value is fixed at 160º, *i.e.* its most probable value.

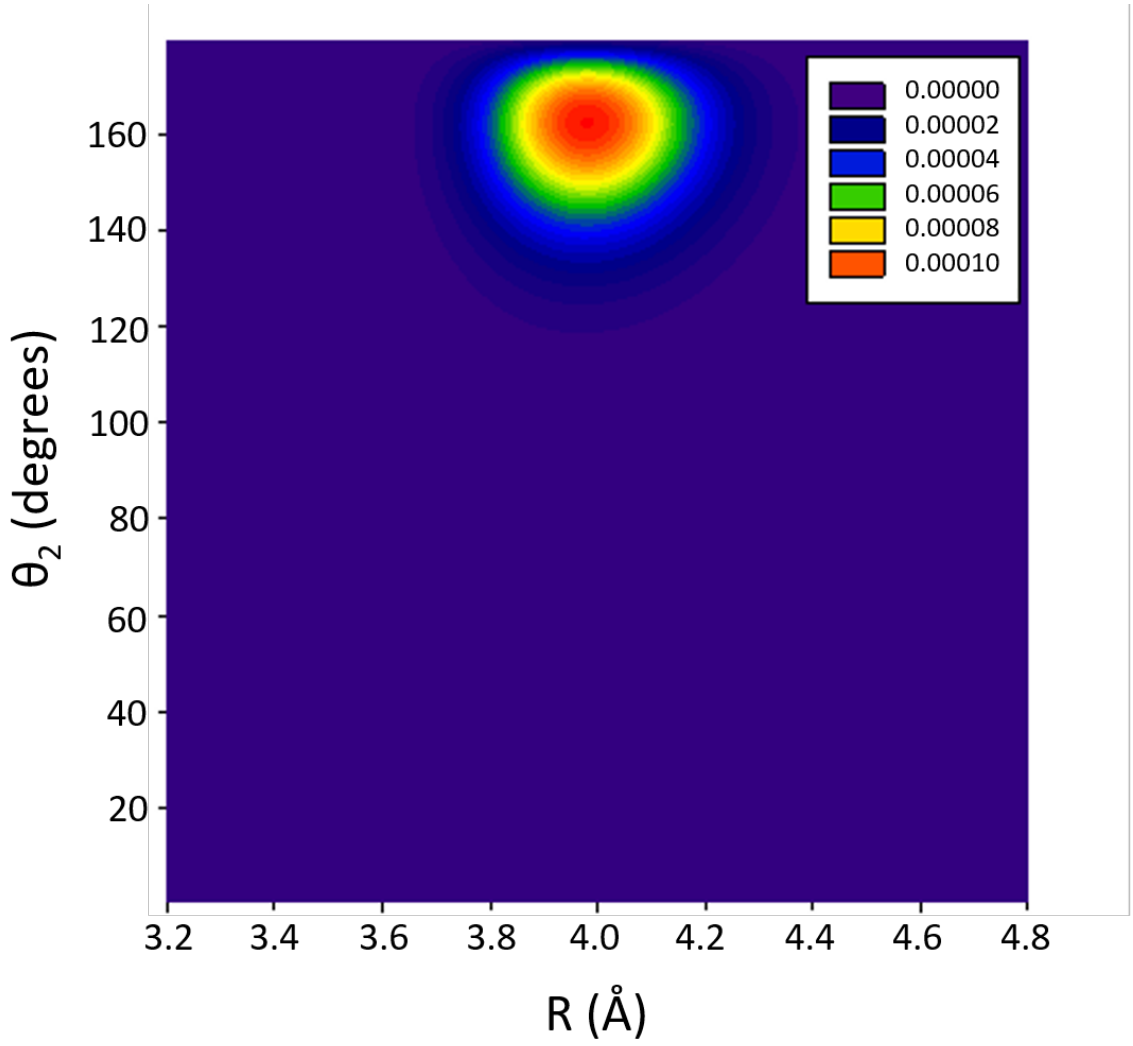

Figure A4.7: Ground state probability amplitude on the potential surface shown in Figure A4.4.

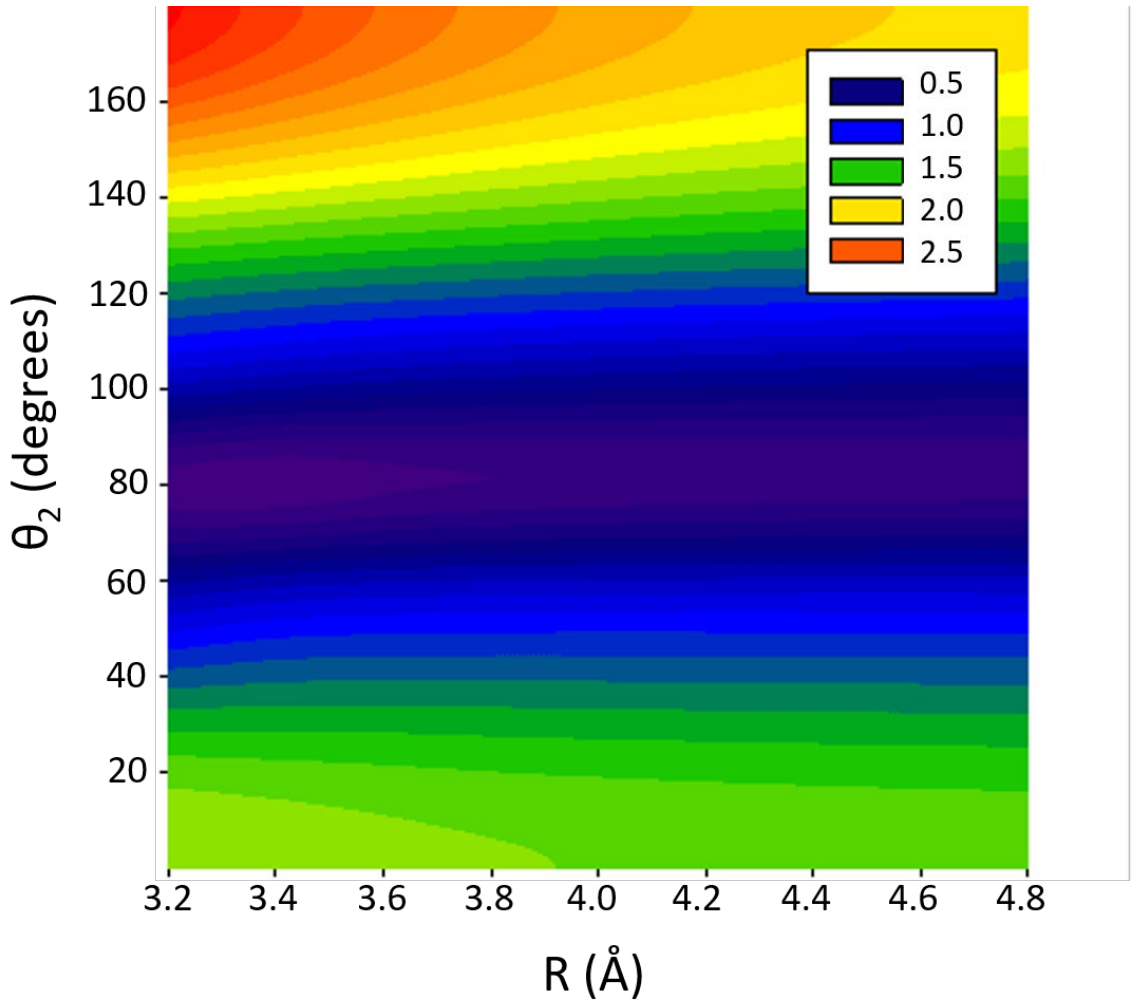

Figure A4.8: Dipole moment surface (same as red contours in Figure A4.4).

4.8 References

(1) Johnson, C. J.; Otto, R.; Continetti, R. E., Spectroscopy and Dynamics of the HOCO Radical: Insights into the OH + CO → H + CO_2 Reaction. *Phys. Chem. Chem. Phys.* **2014**, *16*, 19091-19105

(2) Wayne, R. P., *Chemistry of Atmospheres : An Introduction to the Chemistry of the Atmospheres of Earth, the Planets, and Their Satellites*, 3rd ed.; Oxford University Press: Oxford England ; New York, 2000, p xxix, 775 p.

(3) Warnatz, J., Rate Coefficients in the C/H/O System. In *Combustion Chemistry*, William C. Gardiner, J., Ed. New York : Springer-Verlag: New York, 1984; pp 197-360.

(4) Guo, H., Quantum Dynamics of Complex-Forming Bimolecular Reactions. *Int. Rev. Phys. Chem.* **2012**, *31*, 1-68

(5) Smith, I. W. M.; Zellner, R., Rate Measurements of Reactions of OH by Resonance-Absorption: Part 2 - Reactions of OH with CO, C_2H_4, and C_2H_2. *J. Chem. Soc., Faraday Trans.* **1973**, *69*, 1617

(6) Smith, I. W. M., Mechanism of OH + CO Reaction and Stability of HOCO Radical. *Chem. Phys. Lett.* **1977**, *49*, 112-115

(7) Johnson, C. J.; Poad, B. L. J.; Shen, B. B.; Continetti, R. E., Communication: New Insight into the Barrier Governing CO_2 Formation from OH+CO. *J. Chem. Phys.* **2011**, *134*, 4, 171106.

(8) Nguyen, T. L.; Xue, B. C.; Weston, R. E.; Barker, J. R.; Stanton, J. F., Reaction of HO with CO: Tunneling Is Indeed Important. *J. Phys. Chem. Lett.* **2012**, *3*, 1549-1553

(9) Ma, J. Y.; Li, J.; Guo, H., Tunneling Facilitated Dissociation to H+CO_2 in $HOCO^-$ Photodetachment. *Phys. Rev. Lett.* **2012**, *109*, 5, 063202.

(10) Li, J.; Xie, C. J.; Ma, J. Y.; Wang, Y. M.; Dawes, R.; Xie, D. Q.; Bowman, J. M.; Guo, H., Quasi-Classical Trajectory Study of the HO+CO→H+CO_2 Reaction on a New *ab Initio* Based Potential Energy Surface. *J. Phys. Chem. A* **2012**, *116*, 5057-5067

(11) Wang, X. H.; Bowman, J. M., Mode-Specific Tunneling in the Unimolecular Dissociation of *cis*-HOCO to H + CO_2. *J. Phys. Chem. A* **2014**, *118*, 684-689

(12) Wang, J.; Li, J.; Ma, J. Y.; Guo, H., Full-Dimensional Characterization of Photoelectron Spectra of $HOCO^-$ and $DOCO^-$ and Tunneling Facilitated Decay of HOCO Prepared by Anion Photodetachment. *J. Chem. Phys.* **2014**, *140*, 7, 184314.

(13) Liu, S.; Xu, X.; Zhang, D. H., Communication: State-to-State Quantum Dynamics Study of the OH+CO → H+CO_2 Reaction in Full Dimensions (J=0). *J. Chem. Phys.* **2011**, *135*, 4, 141108.

(14) Ma, J. Y.; Li, J.; Guo, H., Quantum Dynamics of the HO plus CO → H + CO_2 Reaction on an Accurate Potential Energy Surface. *J. Phys. Chem. Lett.* **2012**, *3*, 2482-2486

(15) Radford, H. E.; Wei, W.; Sears, T. J., The Rotational Spectrum of *trans*-HOCO and DOCO. *J. Chem. Phys.* **1992**, *97*, 3989-3995

(16) Oyama, T.; Funato, W.; Sumiyoshi, Y.; Endo, Y., Observation of the Pure Rotational Spectra of *trans*- and *cis*-HOCO. *J. Chem. Phys.* **2011**, *134*, 7, 174303.

(17) Sears, T. J.; Radford, H. E.; Moore, M. A., *b*-Dipole Transitions in *trans*-HOCO Observed by Far-Infrared Laser Magnetic Resonance. *J. Chem. Phys.* **1993**, *98*, 6624-6631

(18) Radford, H. E.; Moore, M. A.; Sears, T. J.; Grussdorf, J.; Nolte, J.; Temps, F., Far-Infrared Laser Magnetic-Resonance of $\tilde{X}^2A'$ *trans*-DOCO. *J. Mol. Spectrosc.* **1994**, *165*, 137-149

(19) Sears, T. J.; Fawzy, W. M.; Johnson, P. M., Transient Diode-Laser Absorption-Spectroscopy of the ν_2 Fundamental of *trans*-HOCO and DOCO. *J. Chem. Phys.* **1992**, *97*, 3996-4007

(20) Petty, J. T.; Moore, C. B., Transient Infrared-Absorption Spectrum of the ν_1 Fundamental of *trans*-HOCO *J. Mol. Spectrosc.* **1993**, *161*, 149-156

(21) Petty, J. T.; Moore, C. B., Transient Infrared-Absorption Spectrum of the ν_1 Fundamental of *trans*-DOCO. *J. Chem. Phys.* **1993**, *99*, 47-55

(22) Chang, C. H.; Buckingham, G. T.; Nesbitt, D. J., Sub-Doppler Spectroscopy of the *trans*-HOCO Radical in the OH Stretching Mode. *J. Phys. Chem. A* **2013**, *117*, 13255-13264

(23) Weston, R. E.; Nguyen, T. L.; Stanton, J. F.; Barker, J. R., HO+CO Reaction Rates and H/D Kinetic Isotope Effects: Master Equation Models with *ab Initio* SCTST Rate Constants. *J. Phys. Chem. A* **2013**, *117*, 821-835

(24) Li, J.; Wang, Y. M.; Jiang, B.; Ma, J. Y.; Dawes, R.; Xie, D. Q.; Bowman, J. M.; Guo, H., Communication: A Chemically Accurate Global Potential Energy Surface for the HO+CO → H+CO_2 Reaction. *J. Chem. Phys.* **2012**, *136*, 4, 041103.

(25) Johnson, C. J.; Harding, M. E.; Poad, B. L. J.; Stanton, J. F.; Continetti, R. E., Electron Affinities, Well Depths, and Vibrational Spectroscopy of *cis*- and *trans*-HOCO. *J. Am. Chem. Soc.* **2011**, *133*, 19606-19609

(26) Milligan, D. E.; Jacox, M. E., Infrared Spectrum and Structure of Intermediates in Reaction of OH with CO. *J. Chem. Phys.* **1971**, *54*, 927-&

(27) Jacox, M. E., The Vibrational-Spectrum of the *t*-HOCO Free-Radical Trapped in Solid Argon. *J. Chem. Phys.* **1988**, *88*, 4598-4607

(28) Forney, D.; Jacox, M. E.; Thompson, W. E., Infrared Spectra of *trans*-HOCO, $HCOOH^+$, and HCO_2^- Trapped in Solid Neon. *J. Chem. Phys.* **2003**, *119*, 10814-10823

(29) Lester, M. I.; Pond, B. V.; Anderson, D. T.; Harding, L. B.; Wagner, A. F., Exploring the OH plus CO Reaction Coordinate *via* Infrared Spectroscopy of the OH-CO Reactant Complex. *J. Chem. Phys.* **2000**, *113*, 9889-9892

(30) Lester, M. I.; Pond, B. V.; Marshall, M. D.; Anderson, D. T.; Harding, L. B.; Wagner, A. F., Mapping the OH+CO → HOCO Reaction Pathway through IR Spectroscopy of the OH-CO Reactant Complex. *Faraday Discuss.* **2001**, *118*, 373-385

(31) Greenslade, M. E.; Tsiouris, M.; Bonn, R. T.; Lester, M. I., Electronic Spectroscopy of the OH-CO Reactant Complex. *Chem. Phys. Lett.* **2002**, *354*, 203-209

(32) Marshall, M. D.; Pond, B. V.; Lester, M. I., Intermolecular Vibrations of the Hydrogen Bonded OH-CO Reactant Complex. *J. Chem. Phys.* **2003**, *118*, 1196-1205

(33) Pollack, I. B.; Tsiouris, M.; Leung, H. O.; Lester, M. I., Infrared Action Spectroscopy and Time-Resolved Dynamics of the OD-CO Reactant Complex. *J. Chem. Phys.* **2003**, *119*, 118-130

(34) Pond, B. V.; Lester, M. I., Decay Dynamics of the Vibrationally Activated OH-CO Reactant Complex. *J. Chem. Phys.* **2003**, *118*, 2223-2234

(35) Lehman, J. H.; Lester, M. I.; Yarkony, D. R., Reactive Quenching of OH A $^2\sum^+$ by O_2 and CO: Experimental and Nonadiabatic Theoretical Studies of H- and O-Atom Product Channels. *J. Chem. Phys.* **2012**, *137*, 14, 094312.

(36) Hartmann, M.; Miller, R. E.; Toennies, J. P.; Vilesov, A., Rotationally Resolved Spectroscopy of SF_6 in Liquid-Helium Clusters - A Molecular Probe of Cluster Temperature. *Phys. Rev. Lett.* **1995**, *75*, 1566-1569

(37) Choi, M. Y.; Douberly, G. E.; Falconer, T. M.; Lewis, W. K.; Lindsay, C. M.; Merritt, J. M.; Stiles, P. L.; Miller, R. E., Infrared Spectroscopy of Helium Nanodroplets: Novel Methods for Physics and Chemistry. *Int. Rev. Phys. Chem.* **2006**, *25*, 15-75

(38) Toennies, J. P.; Vilesov, A. F., Superfluid Helium Droplets: A Uniquely Cold Nanomatrix for Molecules and Molecular Complexes. *Angew. Chem., Int. Ed.* **2004**, *43*, 2622-2648

(39) Stienkemeier, F.; Lehmann, K. K., Spectroscopy and Dynamics in Helium Nanodroplets. *J. Phys. B: At., Mol. Opt. Phys.* **2006**, *39*, R127-R166

(40) Lindinger, A.; Toennies, J. P.; Vilesov, A. F., High Resolution Vibronic Spectra of the Amino Acids Tryptophan and Tyrosine in 0.38 K Cold Helium Droplets. *J. Chem. Phys.* **1999**, *110*, 1429-1436

(41) Choi, M. Y.; Miller, R. E., Four Tautomers of Isolated Guanine from Infrared Laser Spectroscopy in Helium Nanodroplets. *J. Am. Chem. Soc.* **2006**, *128*, 7320-7328

(42) Skvortsov, D. S.; Vilesov, A. F., Using He Droplets for Measurements of Interconversion Enthalpy of Conformers in 2-Chloroethanol. *J. Chem. Phys.* **2009**, *130*, 4, 151101.

(43) Leavitt, C. M.; Moore, K. B.; Raston, P. L.; Agarwal, J.; Moody, G. H.; Shirley, C. C.; Schaefer, H. F.; Douberly, G. E., Liquid Hot NAGMA Cooled to 0.4 K: Benchmark Thermochemistry of a Gas-Phase Peptide. *J. Phys. Chem. A* **2014**, *118*, 9692-9700

(44) Nauta, K.; Miller, R. E., Formation of Cyclic Water Hexamer in Liquid Helium: The Smallest Piece of Ice. *Science* **2000**, *287*, 293-295

(45) Douberly, G. E.; Miller, R. E., The Growth of HF Polymers in Helium Nanodroplets: Probing the Barriers to Ring Insertion. *J. Phys. Chem. B* **2003**, *107*, 4500-4507

(46) Merritt, J. M.; Kupper, J.; Miller, R. E., A High-Resolution Infrared Spectroscopic Investigation of the Halogen Atom-HCN Entrance Channel Complexes Solvated in Superfluid Helium Droplets. *Phys. Chem. Chem. Phys.* **2007**, *9*, 401-416

(47) Merritt, J. M.; Douberly, G. E.; Stiles, P. L.; Miller, R. E., Infrared Spectroscopy of Prereactive Aluminum-, Gallium-, And Indium-HCN Entrance Channel Complexes Solvated in Helium Nanodroplets. *J. Phys. Chem. A* **2007**, *111*, 12304-12316

(48) Liang, T.; Flynn, S. D.; Morrison, A. M.; Douberly, G. E., Quantum Cascade Laser Spectroscopy and Photoinduced Chemistry of Al-$(CO)_n$ Clusters in Helium Nanodroplets. *J. Phys. Chem. A* **2011**, *115*, 7437-7447

(49) Raston, P. L.; Liang, T.; Douberly, G. E., Infrared Spectroscopy of HOOO and DOOO in ^{4}He Nanodroplets. *J. Chem. Phys.* **2012**, *137*, 184302

(50) Morrison, A. M.; Liang, T.; Douberly, G. E., Automation of an "Aculight" Continuous-Wave Optical Parametric Oscillator. *Rev. Sci. Instrum.* **2013**, *84*, 013102.

(51) Raston, P. L.; Liang, T.; Douberly, G. E., Anomalous Lambda-Doubling in the Infrared Spectrum of the Hydroxyl Radical in Helium Nanodroplets. *J. Phys. Chem. A* **2013**, *117*, 8103-8110

(52) Raston, P. L.; Liang, T.; Douberly, G. E., Observation of the Q(3/2) Lambda-Doublet Transitions for $X^2\prod_{3/2}$ OD in Helium Nanodroplets. *Mol. Phys.* **2014**, *112*, 301-303

(53) Liang, T.; Magers, D. B.; Raston, P. L.; Allen, W. D.; Douberly, G. E., Dipole Moment of the HOOO Radical: Resolution of a Structural Enigma. *J. Phys. Chem. Lett.* **2013**, *4*, 3584-3589

(54) Stiles, P. L.; Nauta, K.; Miller, R. E., Dipole Moments of Molecules Solvated in Helium Nanodroplets. *Phys. Rev. Lett.* **2003**, *90*, 4, 135301.

(55) Stanton, J. F., et al. *CFOUR, Coupled-Cluster Techniques for Computational Chemistry*, Version 1.2; Institut für Physikalische Chemie: Universität Mainz, 2010.

(56) Dunning, T. H., Gaussian-Basis Sets for Use in Correlated Molecular Calculations. I. The Atoms Boron through Neon and Hydrogen. *J. Chem. Phys.* **1989**, *90*, 1007-1023

(57) Colbert, D. T.; Miller, W. H., A Novel Discrete Variable Representation for Quantum-Mechanical Reactive Scattering via the S-Matrix Kohn Method. *J. Chem. Phys.* **1992**, *96*, 1982-1991

(58) Bacic, Z.; Light, J. C., Theoretical Methods for Rovibrational States of Floppy Molecules. *Annu. Rev. Phys. Chem.* **1989**, *40*, 469-498

(59) McCoy, A. B., Potential Energy Surfaces and Properties of ICN^- and ICN. *Int. J. Quantum Chem* **2013**, *113*, 366-374

(60) Raston, P. L.; Knapp, C. J.; Jager, W., Rotovibrational Spectroscopy of Hydrogen Peroxide Embedded in Superfluid Helium Nanodroplets. *Phys. Chem. Chem. Phys.* **2011**, *13*, 18789-18798

(61) Chang, C.-H.; Buckingham, G. T.; Nesbitt, D. J., Sub-Doppler Spectroscopy of the trans-HOCO Radical in the OH Stretching Mode. *The Journal of Physical Chemistry A* **2013**, *117*, 13255-13264

(62) Brown, J. M.; Carrington, A., *Rotational Spectroscopy of Diatomic Molecules*; Cambridge University Press: Cambridge, U.K. ; New York, 2003.

(63) Lehmann, K. K., Rotation in Liquid ^{4}He: Lessons from a Highly Simplified Model. *J. Chem. Phys.* **2001**, *114*, 4643-4648

(64) Paolini, S.; Fantoni, S.; Moroni, S.; Baroni, S., Computational Spectroscopy of Helium-Solvated Molecules: Effective Inertia, from Small He Clusters toward the Nanodroplet Regime. *J. Chem. Phys.* **2005**, *123*, 9, 114306.

(65) Fulle, D.; Hamann, H. F.; Hippler, H.; Troe, J., High Pressure Range of Addition Reactions of HO. II. Temperature and Pressure Dependence of The Reaction HO+CO ↔ HOCO → H+CO_2. *J. Chem. Phys.* **1996**, *105*, 983-1000

(66) Golden, D. M.; Smith, G. P.; McEwen, A. B.; Yu, C. L.; Eiteneer, B.; Frenklach, M.; Vaghjiani, G. L.; Ravishankara, A. R.; Tully, F. P., OH(OD)+CO: Measurements and an Optimized RRKM Fit. *J. Phys. Chem. A* **1998**, *102*, 8598-8606

(67) Nauta, K.; Miller, R. E., Nonequilibrium Self-Assembly of Long Chains of Polar Molecules in Superfluid Helium. *Science* **1999**, *283*, 1895-1897

(68) Lehmann, K. K., Potential of a Neutral Impurity in a Large ^{4}He Cluster. *Mol. Phys.* **1999**, *97*, 645-666

(69) Nauta, K.; Miller, R. E., Stark Spectroscopy of Polar Molecules Solvated in Liquid Helium Droplets. *Phys. Rev. Lett.* **1999**, *82*, 4480-4483

(70) Callegari, C.; Conjusteau, A.; Reinhard, I.; Lehmann, K. K.; Scoles, G., First Overtone Helium Nanodroplet Isolation Spectroscopy of Molecules Bearing the Acetylenic CH Chromophore. *J. Chem. Phys.* **2000**, *113*, 10535-10550

(71) Callegari, C.; Reinhard, I.; Lehmann, K. K.; Scoles, G.; Nauta, K.; Miller, R. E., Finite Size Effects and Rotational Relaxation in Superfluid Helium Nanodroplets: Microwave-Infrared Double-Resonance Spectroscopy of Cyanoacetylene. *J. Chem. Phys.* **2000**, *113*, 4636-4646

(72) Dick, B.; Slenczka, A., Inhomogeneous Line Shape Theory of Electronic Transitions for Molecules Embedded in Superfluid Helium Droplets. *J. Chem. Phys.* **2001**, *115*, 10206-10213

(73) Slenczka, A.; Dick, B.; Hartmann, M.; Toennies, J. P., Inhomogeneous Broadening of the Zero Phonon Line of Phthalocyanine in Superfluid Helium Droplets. *J. Chem. Phys.* **2001**, *115*, 10199-10205

(74) Merritt, J. M.; Douberly, G. E.; Miller, R. E., Infrared-Infrared-Double Resonance Spectroscopy of Cyanoacetylene in Helium Nanodroplets. *J. Chem. Phys.* **2004**, *121*, 1309-1316

(75) Ravi, A.; Kuma, S.; Yearwood, C.; Kahlon, B.; Mustafa, M.; Al-Basheer, W.; Enomoto, K.; Momose, T., ν_4 Band of CH_4 in Helium Nanodroplets: A Probe of the Dynamical Response of a Superfluid. *Phys. Rev. A* **2011**, *84*, 4, 020502.

(76) Lehnig, R.; Blinov, N. V.; Jager, W., Evidence for an Energy Level Substructure of Molecular States in Helium Droplets. *J. Chem. Phys.* **2007**, *127*, 4, 241101.

(77) Douberly, G. E.; Stiles, P. L.; Miller, R. E.; Schmied, R.; Lehmann, K. K., $(HCN)_m$-M_n (M = K, Ca, Sr): Vibrational Excitation Induced Solvation and Desolvation of Dopants in and on Helium Nanodroplets. *J. Phys. Chem. A* **2010**, *114*, 3391-3402

(78) Stiles, P. L.; Miller, R. E., High-Resolution Infrared Spectroscopy of HCN-Ag_n (n=1-4) Complexes Solvated in Superfluid Helium Droplets. *J. Phys. Chem. A* **2007**, *111*, 7382-7390

(79) Stiles, P. L.; Miller, R. E., Structures and Bonding Nature of Small Monoligated Copper Clusters (HCN-Cu_n, n=1-3) through High-Resolution Infrared Spectroscopy and Theory. *J. Phys. Chem. A* **2006**, *110*, 10225-10235

CHAPTER 5

INFRARED ZEEMAN SPECTROSCOPY OF COMPLEXES IN HELIUM DROPLETS: ANOMALOUS DROPLET EFFECTS?

The hydroxyl radical and its two van der Waals complexes with carbon monoxide and acetylene are interrogated with infrared Zeeman spectroscopy through the O–H stretch. A variational treatment is used to simulate and analyze spectra collected. The OH–CO complex is well characterized by an effective Hamiltonian based on a gas phase Zeeman effect, and corroborates the magnitude of the magnetic field of 0.425(2) T. In contrast, the hydroxyl radical exhibits about 21% larger Zeeman splitting than is expected. Moreover, the OH–C_2H_2 complex exhibits additional orbital angular momentum quenching when in the Zeeman field, with an increase in the magnitude of the quenching parameter of 30 cm^{-1} which indicates a separation between the low-lying electronic states of an additional 24 cm^{-1}. It is unclear what is influencing the effective Zeeman interaction within the helium droplet environment and it will require further investigation into droplet-dopant interactions.

5.1 Introduction

The application of the Zeeman effect to spectroscopy makes use of the interaction between an externally applied magnetic field and atomic or intramolecular magnetic moments. These interactions mix the rovibronic states within a system and as a result, the spectral signature of the system shifts. To a great approximation, the Zeeman effect is a

linear interaction, indicating that the shifting of states is directly correlated with the strength of the applied magnetic field.[1] However, when the strength of the Zeeman effect reaches the energy of the spin-orbit coupling in the system, it can begin to uncouple the spin and orbital angular momenta. At this point, the interaction is deemed to have passed into the Paschen-Back regime.[2] The understanding of molecular interactions within magnetic fields has led to the extensive use of the Zeeman and Paschen-Back effects to measure the magnetic field strengths in sun spots, dense interstellar clouds, and stars. Magnetic fields are purported to have a major impact on the formation of stars.[2-4] It has even been postulated that the navigation of birds utilizes the Zeeman effect in radical-pair reactions within the retina.[5-6]

Due to its ubiquitous use in interrogating the star forming regions of the universe,[4] the majority of research on the Zeeman effect of open-shell radicals is for diatomics, and it has found very little application to the spectroscopy of small nonlinear open-shell radicals and complexes with radicals. However, it can be a very useful tool in understanding molecular structure and intermolecular interactions within small systems. The Zeeman effect can be used to identify the absolute direction of a dipole moment, measure the magnitude of the quadrupole moment, and identify the ground electronic structure of a molecule.[7]

The understanding of the Zeeman effect for linear radicals is thorough and well cataloged, both from a perturbation theory approach as well as with the variational method.[1] As far as we are aware, there has been one attempt to apply the Zeeman effect for non-linear systems through a variational method approach,[8] though the system was derived in a Hund's case (b) basis. Additionally, perturbation theory corrections have

been applied with good success.[7] Admittedly, the Zeeman effect in non-linear molecules is usually applied in microwave spectroscopy which affords much higher resolution than infrared spectroscopy in helium droplets. This limited resolution makes it impossible to use this technique to measure hyperfine interactions, such as nuclear spin angular momentum, as these contributions to the Zeeman effect are weak and therefore impossible to observe. Nevertheless, $\mu \cdot B$ affects the rotational fine structure of vibrational transitions, which is observable at the level of resolution afforded by ^{4}He droplet infrared spectroscopy. We present here, a variational approach to the study of the Zeeman effect in helium droplets for linear and non-linear open-shell radicals and complexes.

5.2 Experimental Methods

The helium droplet apparatus has been well described in the literature,[9-11] however this article will detail the implementation of a modification that facilitates the collection of Zeeman spectroscopy in helium droplets. The three test cases used in this investigation have all been interrogated previously in helium droplets,[12-15] and thus further experimental parameters relevant to the production of these species can be obtained from the literature directly. Helium nanodroplets are generated by expansion of ultrapure (99.9999%) ^{4}He gas through a 5 μm orifice maintained between 15 and 18 K. The expansion is skimmed into a beam using a 400 μm skimmer cone situated approximately 1 cm downstream from the orifice. The droplets formed in this manner cool through helium atom evaporation to a final temperature of ~0.4 K. Evaporation of a helium atom from the surface of the droplet carries with it ~5 cm^{-1} of energy. The beam

passes into a series of differentially pumped "pick-up" cells which facilitate gas phase collisions with the beam that embed molecular species of interest, and these species are quickly thermalized with the droplet via helium atom evaporation. After the doping process, the beam is allowed to interact with the tunable idler of a continuous wave infrared optical parametric oscillator (cw-IR-OPO).[10] As used previously,[16] the multipass cell arrangement will be used to contain the laser-droplet interaction region entirely within the magnetic field of the Zeeman cell. When the idler is resonant with a transition of a species contained in the droplet, the absorption of a photon induces helium atom evaporation as the molecule transfers the energy to the surrounding bath. This reduces the electron ionization cross-section of a droplet and hence presents itself as a reduction in current measured on a particular mass signal in the mass spectrometer that corresponds to the charge transfer ionization of the species within.

The Zeeman cell is shown on the right in Figure 5.1. It comprises two Nd rare-earth magnets, each 4 in. x 2 in. x 0.5 in. and with a field strength of approximately 1 T. The magnetic field direction is along the shortest dimension (i.e. 0.5 in.). The magnets are separated by 0.75 in. with opposing poles facing. The inner poles are "capped" with a 0.125 in. steel plate intended to homogenize the field contained within. The outward facing poles of the magnets are attached to 0.5 in. thick steel bars, which have themselves been connected via a steel crossbar to form a rectangular horseshoe shape. The crossbar has a 10 mm diameter hole through which the droplet beam continues into the mass spectrometer chamber. Finally, an aluminum support has been added opposite the crossbar to ensure the magnets do not detach themselves from the steel bars, as they are only affixed magnetically. This design was chosen to provide an approximate field

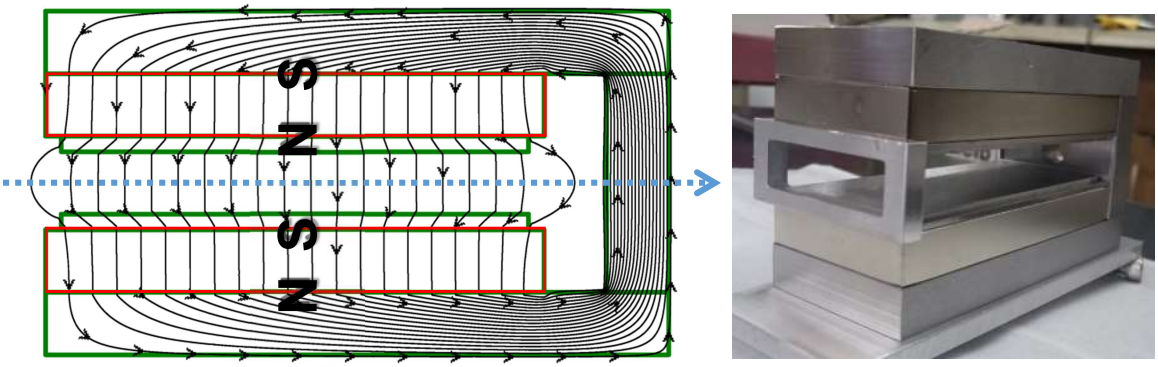

Figure 5.1: (Left) Vizimag simulations of the magnetic field lines in the Zeeman cell. The red rectangles represent Neodymium rare-earth permanent magnets (~1 Tesla each), and the green rectangles represent high-permeability iron. The thin iron caps attached to the magnets improved the field homogeneity in the droplet beam (blue arrow) laser interaction zone. The laser light passes through the static magnetic field at nearly right angles by reflection between two ~15 cm long rectangular gold-coated mirrors, which are oriented perpendicular to the Zeeman cell. The Zeeman field was calibrated with a commercial, hand-held, high-precision Hall probe (0.425(2) Tesla). The error bar in the field measurement is derived from the standard deviation of many successive measurements by multiple humans. (Right) Photograph of the Zeeman cell. An aluminum spacer provides support so that the magnets don't crash into each other. A 5 mm diameter hole is drilled in the iron circuit to allow the droplet beam to pass towards the mass spectrometer detector.

strength of 0.5 T along the centerline of the cell. When measured experimentally with a commercially available high-precision Hall probe, the field strength was determined to be 0.425(2) T. Error in field strength was calculated from averaging several measurements. A Vizimag simulation is provided in the left panel of Figure 5.1, which showcases the favorable effect the steel frame has on the design. Figure 5.2 shows the cell in relation to the multipass mirrors.

5.3 Simulation Methodology

To appropriately simulate spectra collected, it is necessary to derive an appropriate Zeeman effective Hamiltonian for use in a variational treatment of the interacting states. The most dominant interactions within the Zeeman effect involve the molecular magnetic dipole (μ_m) interacting with the magnetic field (B):

$$H_{Zeeman} = -\mu_m \cdot B \tag{5.1}$$

The molecular magnetic dipole is a vector quantity with contributions that derive from interactions such as electron orbital and spin angular momenta. Indeed, these aforementioned contributions dominate the dipolar Zeeman effect, with other contributions like rotational magnetic and nuclear spin magnetic momenta having much smaller magnitude.[1] With the appropriate model for the effective Zeeman Hamiltonian, we may write Eq. 5.1 as

$$H_{Zeeman} = -\mu_B(g_L L + g_s S) \cdot B \tag{5.2}$$

where L and S are the orbital and spin angular momentum operators, μ_B is the Bohr magneton, and the g's are the g-factors for both orbital and spin angular momenta respectively. These have a value of $g_L = 1$ and $g_S = 2.0023$. We will use tensor algebra[1] to

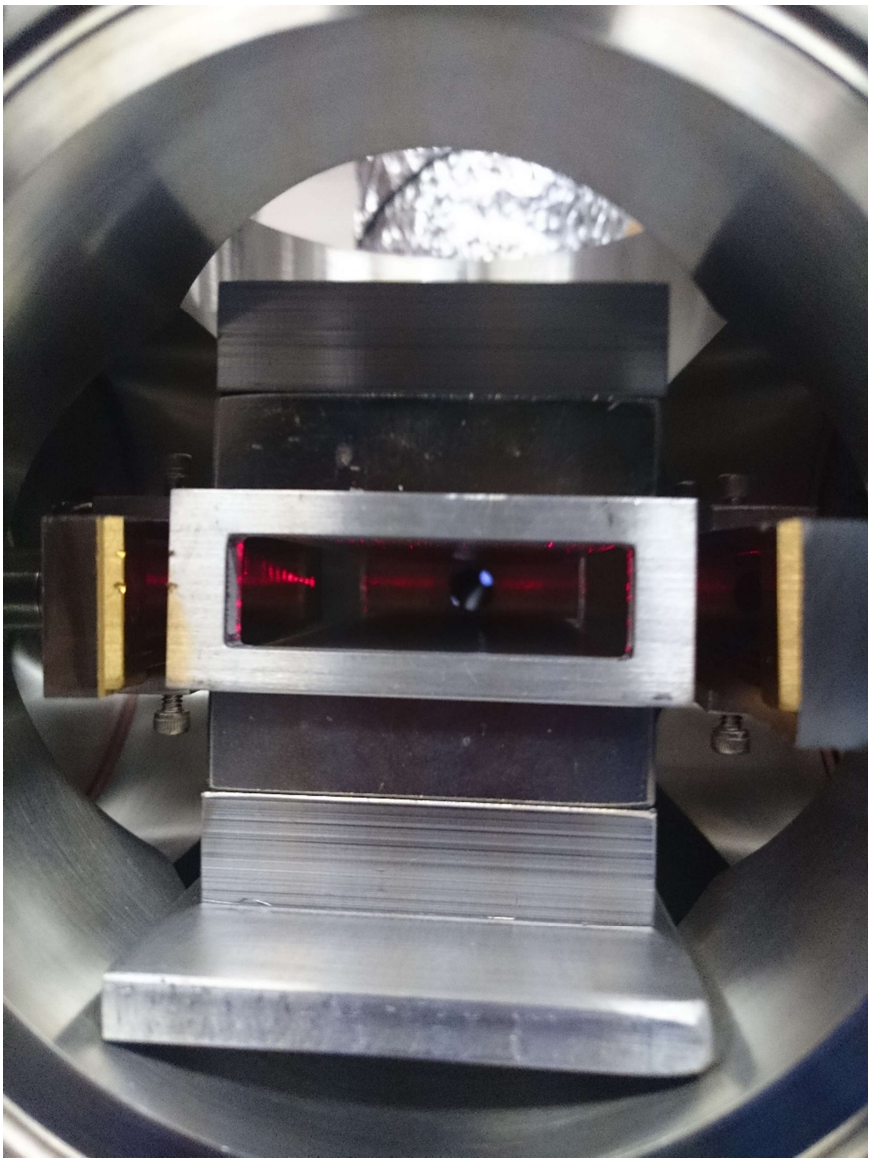

Figure 5.2: Image of Zeeman Cell situated between the plane mirrors that constitute the multipass cell. A HeNe laser shows the trajectory of light when incident correctly on the mirrors.

further derive the expressions for the effective Hamiltonian as it contains a simple expression for the transformation between lab fixed and molecule fixed axes. Equation 5.2 in tensor form is

$$\begin{aligned} H_{Zeeman} &= -\left(g_L T^1(\boldsymbol{L}) + g_S T^1(\boldsymbol{S})\right)\mu_B \cdot T^1(\boldsymbol{B}) \\ &= -g_L \mu_B T^1(\boldsymbol{B}) \cdot T^1(\boldsymbol{L}) - g_S \mu_B T^1(\boldsymbol{B}) \cdot T^1(\boldsymbol{S}) \end{aligned} \tag{5.3}$$

where the tensor products are taken between all combinations of the axes. Since we will define the magnetic field to lie along the lab-fixed Z axis, we will omit $p = \pm 1$ terms from $T^1(\boldsymbol{B})$ and represent $\boldsymbol{L}$ and $\boldsymbol{S}$ relative to the molecular axis frame to obtain

$$\begin{aligned} H_{Zeeman} &= -g_L \mu_B T^1(\boldsymbol{B}) \cdot T^1(\boldsymbol{L}) - g_S \mu_B T^1(\boldsymbol{B}) \cdot T^1(\boldsymbol{S}) \\ &= -\mu_B \sum_{q=-1}^{1} T_0^1(\boldsymbol{B}) \mathfrak{D}_{0q}^{(1)*} \left[g_L T_q^1(\boldsymbol{L}) + g_S T_q^1(\boldsymbol{S})\right] \end{aligned} \tag{5.4}$$

and q can take the values {-1,0,1}, which are related to the three molecule-fixed axes. We simplify completely to

$$\begin{aligned} H_{Zeeman} &= -\mu_B \sum_{q=-1}^{1} T_0^1(\boldsymbol{B}) \mathfrak{D}_{0q}^{(1)*} \left[g_L T_q^1(\boldsymbol{L}) + g_S T_q^1(\boldsymbol{S})\right] \\ &= -\mu_B B_z \sum_{q=-1}^{1} g_L \mathfrak{D}_{0q}^{(1)*} T_q^1(\boldsymbol{L}) + g_S \mathfrak{D}_{0q}^{(1)*} T_q^1(\boldsymbol{S}) \end{aligned} \tag{5.5}$$

The experiments presented herein will involve linear and T-shaped complexes, which will each have unique matrix elements as they will be simulated with different basis sets. In the case of the linear complexes, the matrix elements will be calculated using primitive Hund's case (a) basis functions, while for T-shaped complexes, the parity conserving Hund's case (a) basis functions will be used. The primitive Hund's case (a) basis functions have the form

$$\left|\eta, \Lambda; S, \Sigma; J, M_J, \Omega\right\rangle \tag{5.6}$$

where η, S, and J represent the orbital, spin, and total angular momenta, with their respective projections on the cylindrical axis, Λ, Σ, and Ω. M_J represents the projection of

the total angular momentum on the lab fixed Z axis. In the case of the parity conserving case (a) basis, the complexation spoils the cylindrical symmetry of the hydroxyl radical, leading to a descent in symmetry. Thus, we use the non-linear labels for the primitive basis which is used to build the parity conserving basis:

$$\left|J, p, M_J, \lambda, \sigma\right\rangle \tag{5.7}$$

with the λ and σ retaining their previous meaning, and p replacing Ω for the projection of the total angular momentum on the symmetry a-axis in the molecule fixed representation. We further omit η and s for clarity. The parity conserving basis is derived from the primitives in the following manner[17]

$$\left|J, |p|, M_J, \lambda, \sigma, \epsilon\right\rangle = \frac{1}{\sqrt{2}}\left[\left|J, |p|, M_J, \lambda, \sigma\right\rangle + \epsilon(-1)^{J-\frac{1}{2}}\left|J, -|p|, M_J, -\lambda, -\sigma\right\rangle\right] \tag{5.8}$$

where ε is given a value of either 1 or -1.

We begin deriving from Eq. 5.5 using the basis set of Eq. 5.6.

$$\begin{aligned}&\left\langle \eta, \Lambda; S, \Sigma; J, M_J, \Omega\right|H_{Zeeman}\left|\eta', \Lambda'; S', \Sigma'; J', M_J', \Omega'\right\rangle = \\ &-\mu_B B_z \sum_{q=-1}^{1}\left(\left\langle \eta, \Lambda; S, \Sigma; J, M_J, \Omega\right|g_L \mathfrak{D}_{0q}^{(1)*} T_q^1(\boldsymbol{L})\left|\eta', \Lambda'; S', \Sigma'; J', M_J', \Omega'\right\rangle\right. \\ &\qquad\left. + \left\langle \eta, \Lambda; S, \Sigma; J, M_J, \Omega\right|g_S \mathfrak{D}_{0q}^{(1)*} T_q^1(\boldsymbol{S})\left|\eta', \Lambda'; S', \Sigma'; J', M_J', \Omega'\right\rangle\right)\end{aligned} \tag{5.9}$$

Using the Wigner-Eckart Theorem[1],

$$\begin{aligned}&\left\langle -\left|g_L \mathfrak{D}_{0q}^{(1)*} T_q^1(\boldsymbol{L})\right|-'\right\rangle \\ &\qquad = \; g_L \langle J, M_J, \Omega|\mathfrak{D}_{0q}^{(1)*}|J', M_J', \Omega'\rangle\langle \eta, \Lambda|T_q^1(\boldsymbol{L})|\eta', \Lambda'\rangle\langle S, \Sigma|S', \Sigma'\rangle\end{aligned} \tag{5.10}$$

$$\begin{aligned}&\left\langle -\left|g_L \mathfrak{D}_{0q}^{(1)*} T_q^1(\boldsymbol{L})\right|-'\right\rangle \\ &\qquad = \; g_L\left\{(-1)^{M-\Omega}[(2J'+1)(2J+1)]^{\frac{1}{2}}\right. \\ &\qquad \left.\times \begin{pmatrix} J & 1 & J' \\ -M & 0 & M' \end{pmatrix}\begin{pmatrix} J & 1 & J' \\ -\Omega & 0 & \Omega' \end{pmatrix}\right\}\langle \eta, \Lambda|T_q^1(\boldsymbol{L})|\eta', \Lambda'\rangle \delta_{S,S'}\delta_{\Sigma,\Sigma'}\end{aligned} \tag{5.11}$$

$T_q^1(S)$ is derived exactly as Eq. 5.11. We note here that specifically in the case of $\langle \eta, \Lambda | T_q^1(\boldsymbol{L}) | \eta', \Lambda' \rangle$, we will not resolve effects due to coupling between states of different Λ, therefore $q = 0$ (molecular z-axis) is the only term with which we will concern ourselves. This leaves us with the spherical tensor operator $\boldsymbol{L}_z$, which has the eigenvalue

$$\langle \eta, \Lambda | L_z | \eta', \Lambda' \rangle = \Lambda \delta_{\eta,\eta'} \delta_{\Lambda,\Lambda'} \tag{5.12}$$

Plugging this into Eq. 5.11 we obtain

$$\begin{aligned} \left\langle - \left| g_L \mathfrak{D}_{0q}^{(1)*} T_q^1(\boldsymbol{L}) \right| - ' \right\rangle \\ = \; g_L \Lambda \Bigg\{ (-1)^{M-\Omega} [(2J+1)(2J'+1)]^{\frac{1}{2}} \\ \times \begin{pmatrix} J & 1 & J' \\ -M & 0 & M' \end{pmatrix} \begin{pmatrix} J & 1 & J' \\ -\Omega & 0 & \Omega' \end{pmatrix} \Bigg\} \delta_{\eta,\eta'} \delta_{\Lambda,\Lambda'} \delta_{S,S'} \delta_{\Sigma,\Sigma'} \end{aligned} \tag{5.13}$$

Substituting the two matrix elements (Eq. 5.13 and its equivalent for $T_q^1(S)$) into Eq. 5.9, we obtain

$$\begin{aligned} & \langle - | H_{Zeeman} | - ' \rangle \\ & = \; \mu_B B_Z (-1)^{M-\Omega} [(2J+1)(2J'+1)]^{\frac{1}{2}} \\ & \times \begin{pmatrix} J & 1 & J' \\ -M & 0 & M' \end{pmatrix} \Bigg\{ g_L \Lambda \begin{pmatrix} J & 1 & J' \\ -\Omega & 0 & \Omega' \end{pmatrix} \delta_{\Sigma'\Sigma} \\ & + \left(\frac{3}{2}\right)^{\frac{1}{2}} g_S (-1)^{S-\Sigma} \sum_{q=-1}^{1} \begin{pmatrix} J & 1 & J' \\ -\Omega & q & \Omega' \end{pmatrix} \begin{pmatrix} S & 1 & S' \\ -\Sigma & q & \Sigma' \end{pmatrix} \Bigg\} \delta_{\Lambda'\Lambda} \delta_{\eta'\eta} \delta_{S'S} \end{aligned} \tag{5.14}$$

This is the matrix element for the primitive case (a) basis. To obtain a similar result for the parity conserving case (a) basis, we need the matrix elements

$$\left\langle J, |p|, M_J, \lambda, \sigma, \epsilon \left| H_{Zeeman} \right| J', |p'|, M_J', \lambda', \sigma', \epsilon' \right\rangle \tag{5.15}$$

which involve combinations of the primitives

$$\frac{1}{\sqrt{2}} \left[\langle \oplus | + \epsilon (-1)^{J-\frac{1}{2}} \langle \ominus | \right] \frac{1}{\sqrt{2}} \left[| \oplus \rangle + \epsilon' (-1)^{J'-\frac{1}{2}} | \ominus \rangle \right] \tag{5.16}$$

$$\frac{1}{2}\Big[\langle\oplus\mid\oplus\rangle+\epsilon(-1)^{J-\frac{1}{2}}\langle\ominus\mid\oplus\rangle+\epsilon'(-1)^{J'-\frac{1}{2}}\langle\oplus\mid\ominus\rangle + \epsilon\epsilon'(-1)^{J+J'-1}\langle\ominus\mid\ominus\rangle\Big] \tag{5.17}$$

where H_{Zeeman} has been omitted for clarity and the quantum numbers are defined as follows

$$\oplus = (J, |p|, M_J, \lambda, \sigma) \tag{5.18}$$
$$\ominus = (J, -|p|, M_J, -\lambda, -\sigma) \tag{5.19}$$

Working through the tensor algebra, and applying a similar constraint to Eq. 5.12, we learn that the only two allowed combinations from Eq. 5.17 are

$$\frac{1}{2}\big[\langle\oplus\mid\oplus\rangle+\epsilon\epsilon'(-1)^{J+J'-1}\langle\ominus\mid\ominus\rangle\big] \tag{5.20}$$

As J and J' are half integer in this case, the quantity $J + J' - 1$ will always be even, and hence we have

$$\frac{1}{2}[\langle\oplus\,|H_{Zeeman}|\,\oplus\rangle+\epsilon\epsilon'\langle\ominus\,|H_{Zeeman}|\,\ominus\rangle] \tag{5.21}$$

This result gives the following matrix element

$$\begin{aligned}\langle -|H_{Zeeman}|-'\rangle &= \mu_B B_z(-1)^{M+P}[(2J+1)(2J'+1)]^{1/2} \\ &\times \begin{pmatrix} J & 1 & J' \\ -M & 0 & M' \end{pmatrix}\begin{pmatrix} J & 1 & J' \\ -P & 0 & P' \end{pmatrix} \\ &\times \Big\{g_L(-1)^{\ell+\lambda}[\ell(\ell+1)(2\ell+1)]^{1/2}\begin{pmatrix} \ell & 1 & \ell' \\ -\lambda & 0 & \lambda' \end{pmatrix} \\ &+ g_S(-1)^{S+\sigma}[S(S+1)(2S+1)]^{1/2}\begin{pmatrix} S & 1 & S' \\ -\sigma & 0 & \sigma' \end{pmatrix}\Big\} \\ &\times \delta_{P,P'}\delta_{M,M'}\delta_{\lambda,\lambda'}\delta_{\sigma,\sigma'}\delta_{\epsilon,\epsilon'}\end{aligned} \tag{5.22}$$

5.4 Results

The hydroxyl radical stretch of the OH-CO van der Waals complex has been studied previously,[15] and therefore serves as a simple probe to investigate the Zeeman effect within helium droplets. The Zeeman spectra collected for the OH-CO complex in

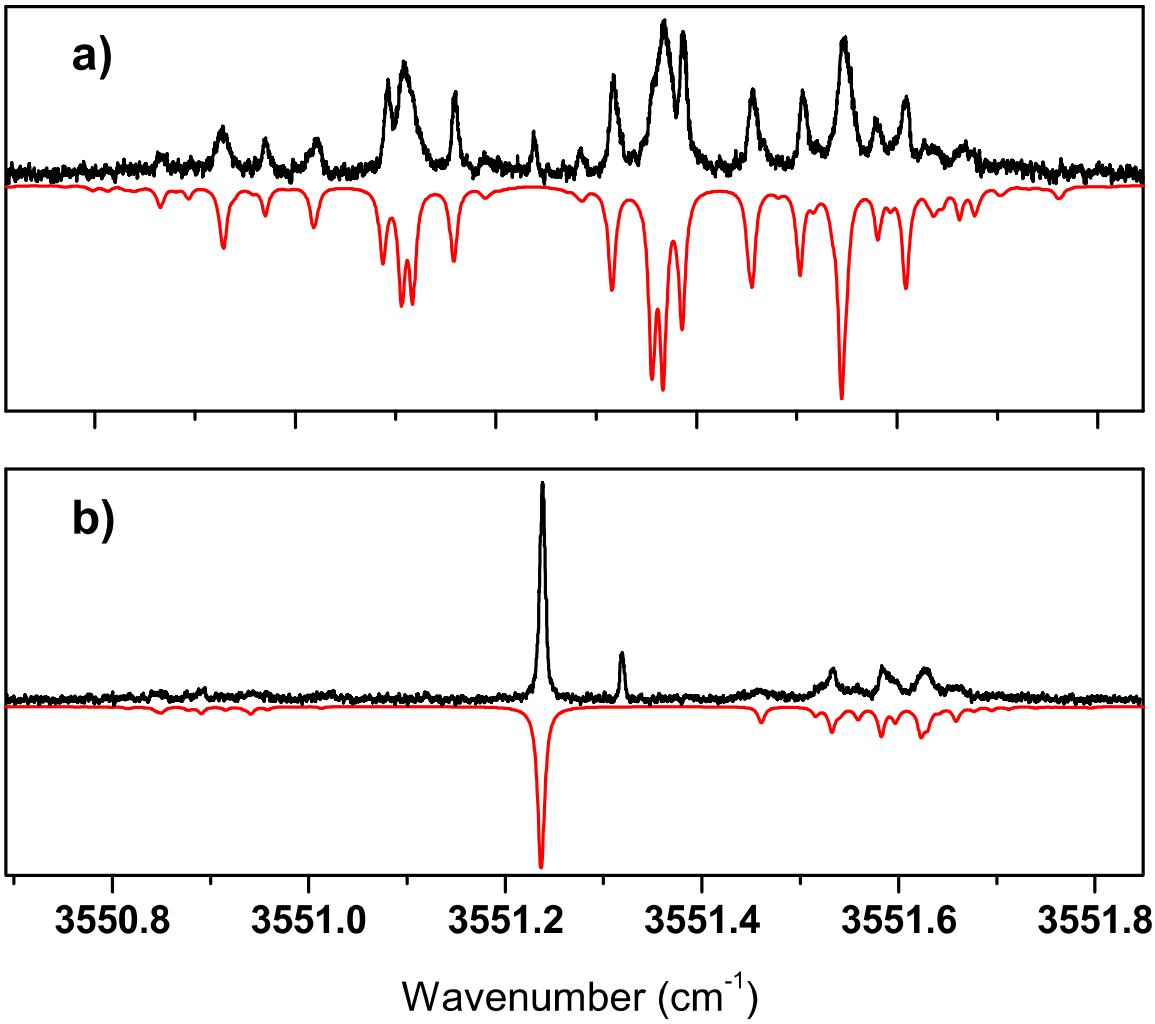

Figure 5.3: Infrared Zeeman spectra of the OH stretch band of the linear OH−CO hydrogen bonded complex. Zeeman spectra were obtained with both (a) perpendicular and (b) parallel laser polarization configurations. The red traces are simulations using the effective Hamiltonian model described in the text and a field strength of 0.425(2) Tesla.

helium droplets is shown in Figure 5.3. Simulations using the variational treatment are provided in red below their corresponding experimental traces. The simulation uses constants from the complex determined by previous zero-field and Stark measurements. As such, when 0.425 T is used to simulate the hydroxyl stretch in the complex within the magnetic field, there are no adjustable parameters in the system. Despite the rigid simulation, agreement in Figure 5.3 is surprisingly excellent, and provides another positive confirmation that the chosen effective Hamiltonian and derived matrix elements appear to be accurate.

Figure 5.4 presents the perpendicular and parallel Zeeman spectra of the hydroxyl radical. The Zeeman mixing in the first term of the summation only mixes *J* levels, while the second matrix term is responsible for mixing the different spin-orbit levels, $\langle J \pm 1; S \pm 1; \Omega \pm 0,1; \Sigma \pm 0,1 | J, S, \Omega, \Sigma \rangle$, within the radical. As noted in Figure 5.4 with the dashed lines, the magnitude of the splitting in the perpendicular spectrum is identical for both the *e*←*f* and *f*←*e* zero-field transitions, at 0.19 cm^{-1}. The parallel spectrum is missing this particular splitting due to the mixing constraint imposed by the multiplicative 3-*j* symbol $\begin{pmatrix} J & 1 & J' \\ -M & 0 & M' \end{pmatrix}$ in Eq. 5.14. This term prevents coupling between states of different *M*. Therefore, in the parallel spectrum, the selection rule ΔM = 0 does not allow transitions between states that have not been mixed (i.e. initial and final states were shifted equivalently), leading to identical transition frequencies as found in the zero-field spectrum.[12]

Simulations of the Zeeman perpendicular spectrum using the variational treatment described in Section 5.3 underestimate the observed splitting, with a predicted value of about 0.157 cm^{-1}. The increased splitting implies a stronger Zeeman

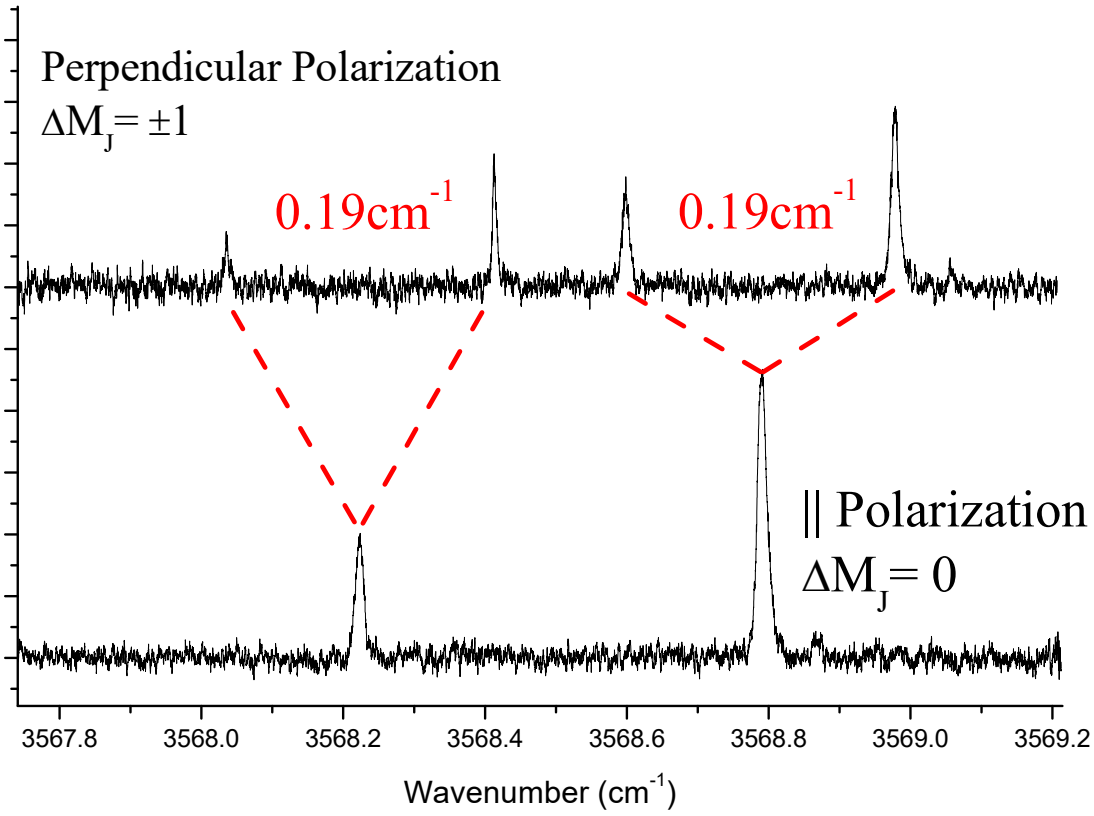

Figure 5.4: Zeeman Spectra for OH radical in helium droplets. Note that the parallel spectrum mimics the zero-field spectrum,[12] and the dashed lines are a visual aid to illuminate the identical nature of the splittings observed.

interaction by about 21%. To diagnose the discrepancy as an issue with the derived Zeeman Hamiltonian matrix elements, a perturbation theory approach was employed, as the Paschen-Back effect for the ground electronic state of OH is known to be several orders of magnitude larger than those used in this experiment.[2] Perturbation theory predicts the Zeeman interaction energy for a good case (a) molecule according to the following formula[1]

$$\Delta E_{Zeeman} = \mu_B B_Z m_j g_j \tag{5.23}$$

where,

$$g_j = \frac{(\Lambda + \Sigma)(\Lambda + g_s\Sigma)}{J(J+1)} \tag{5.24}$$

For the ground rovibronic state of OH, $^2\Pi_{3/2}$, $\Lambda = 1$, $\Sigma = 1/2$, $J = 3/2$, and $g_s = 2.00232$. Using the value of the Bohr magneton[18] in GHz T^{-1}, with a $B_Z = 0.425$ T and an $m_j = 3/2$, the result of the perturbation theory calculation is

$$\begin{aligned}\Delta E_{Zeeman} &= (13.996)0.425\frac{\left(1+\frac{1}{2}\right)\left(1+\left(2.00232*\frac{1}{2}\right)\right)}{\left(\frac{3}{2}\right)\left(\frac{3}{2}+1\right)} \\ &= 4.66\ \text{GHz}\end{aligned} \tag{5.25}$$

which is 0.155 cm^{-1}. This is nearly equivalent to the value obtained by the variational calculation, indicating the discrepancy did not arise from the effective Hamiltonian or the derived matrix elements.

Non-linear complexation of the hydroxyl radical results in orbital angular momentum quenching, which adds complexity to the molecular Zeeman effect. The effective Hamiltonian now includes a quenching parameter as derived by Marshall and Lester.[19] This has been previously applied to hydroxyl radical systems in helium droplets quite successfully,[13-15] including non-linear complexes. The T-shaped complex of

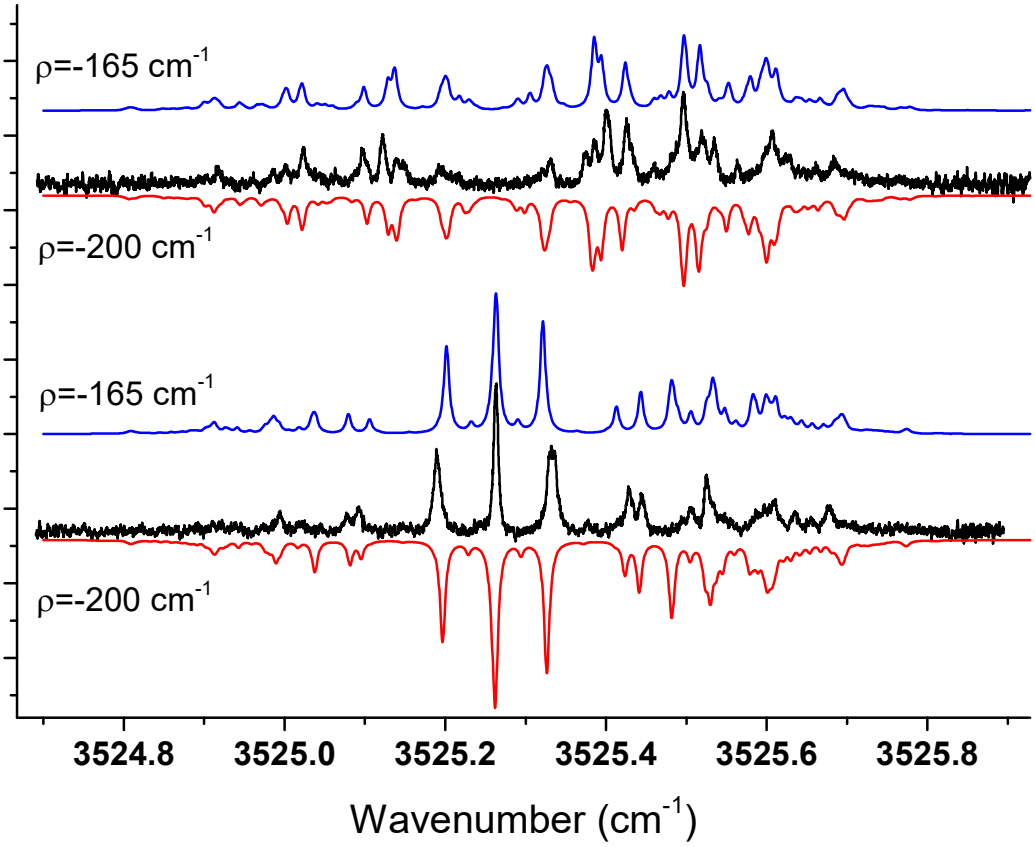

Figure 5.5: Experimental trace in black. Blue traces use parameters fixed with zero-field values. Red traces use a modified value of ρ to fit the experimental spectrum.

$OH\text{-}C_2H_2$ is the final test case for the Zeeman interactions, as it provides the most general case thus far investigated. Zero-field parameters for the complex in helium droplets were determined by Douberly *et al.*[13] and were used for simulation of the Zeeman spectra.

Zeeman spectra of the $OH\text{-}C_2H_2$ complex measured in helium droplets is shown in Figure 5.5. Simulations implemented with the T-shaped matrix elements from Section 5.3 were used in a variational treatment of the complex. In a manner similar to the OH-CO complex, parameters were fixed for the simulation. The results of this simulation can be found in Figure 5.5, underneath the corresponding experimental spectrum. It is interesting to note that in this case, agreement is not even qualitative. In contrast to the OH-CO complex effective Hamiltonian, the new Hamiltonian has an additional parameter, which in theory need not be constrained in order to remain consistent with previous results. The magnitude of the quenching parameter ρ, when increased relative the zero-field value, provides a nearly satisfying agreement with the measured spectra. One might argue that due to complexation, the value of the associated orbital angular momentum *g*-factor would deviate from its nominal value of 1. While this does provide a method of bringing simulation in agreement with experiment, it was impossible to choose a value of g_L such that simulations agreed satisfactorily with both perpendicular and parallel spectra simultaneously. Furthermore, the deviation was quite large, about 50%, for parallel spectrum, which seems unphysical at present. The new value of the quenching parameter ρ which provided the greatest agreement was -195 cm^{-1}. Simulations compared to experiment for the new value of ρ are presented in Figure 5.6.

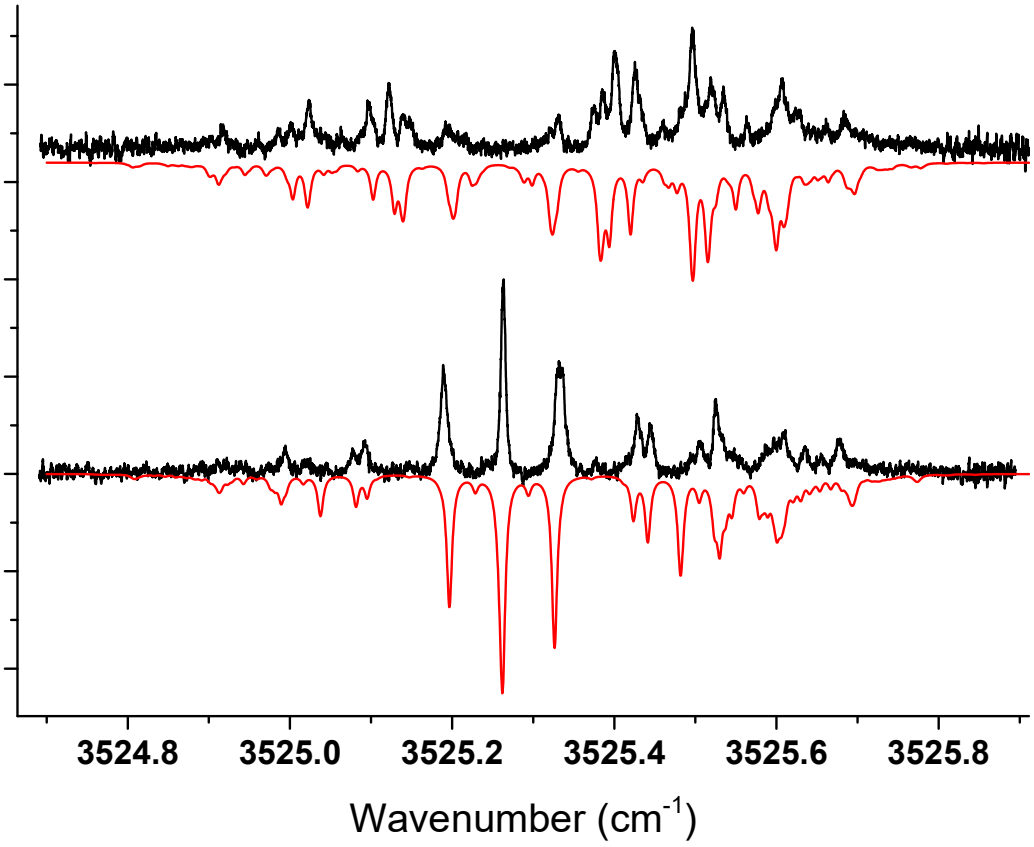

Figure 5.6: Simulation from Figure 5.5 recomputed using ρ = -195 cm^{-1}. Agreement between simulation and experiment motivate an assessment of the splitting between the two states may actually be around 240 cm^{-1}, especially when juxtaposed to the rigid simulation in Figure 5.5.

5.5 Discussion

The Zeeman spectra of the OH-CO complex unequivocally identify the ground electronic state as $^2\Pi_{3/2}$. Although perhaps an expected result, it does confirm that the application of the Zeeman effect within a helium droplet environment can be straight-forward. Additionally, this system confirmed the magnetic field strength of the Zeeman cell spectroscopically, providing a sensitive investigation of the effect the droplet may have on the effective field strength experienced by molecular dopants. It is interesting to note that the Zeeman field had a similar effect as the Stark field for the OH-CO complex. As mentioned in Section 4.5, the Stark field removed inhomogeneous broadening observed in the zero-field measurement, which has been attributed to anisotropic interaction potential between the droplet and the dopant. Likewise, the Zeeman field removes this inhomogeneous broadening, but just like the Stark effect, this result is not well understood.

The OH-C_2H_2 complex is a very interesting deviation from the simplistic case of OH-CO. The angular momentum quenching in zero-field helium droplets is already larger than that of the gas phase values measured by Marshall and coworkers.[20] This quenching is indicative of the separation between two low lying electronic states in the complex: $^2B_1$ and $^2B_2$.[13] The increase in the zero-field splitting of these two states in helium droplets is attributed to differing free solvation energies of the two states. Rather unexpectedly, interaction of the complex with a magnetic field appears to have increased the coupling between the states, suggesting an even larger electronic separation. Currently there is no mechanism in the Zeeman matrix elements to account for this result, and the easiest way to account for such an interaction is via the parameter ρ. Figure 5.7

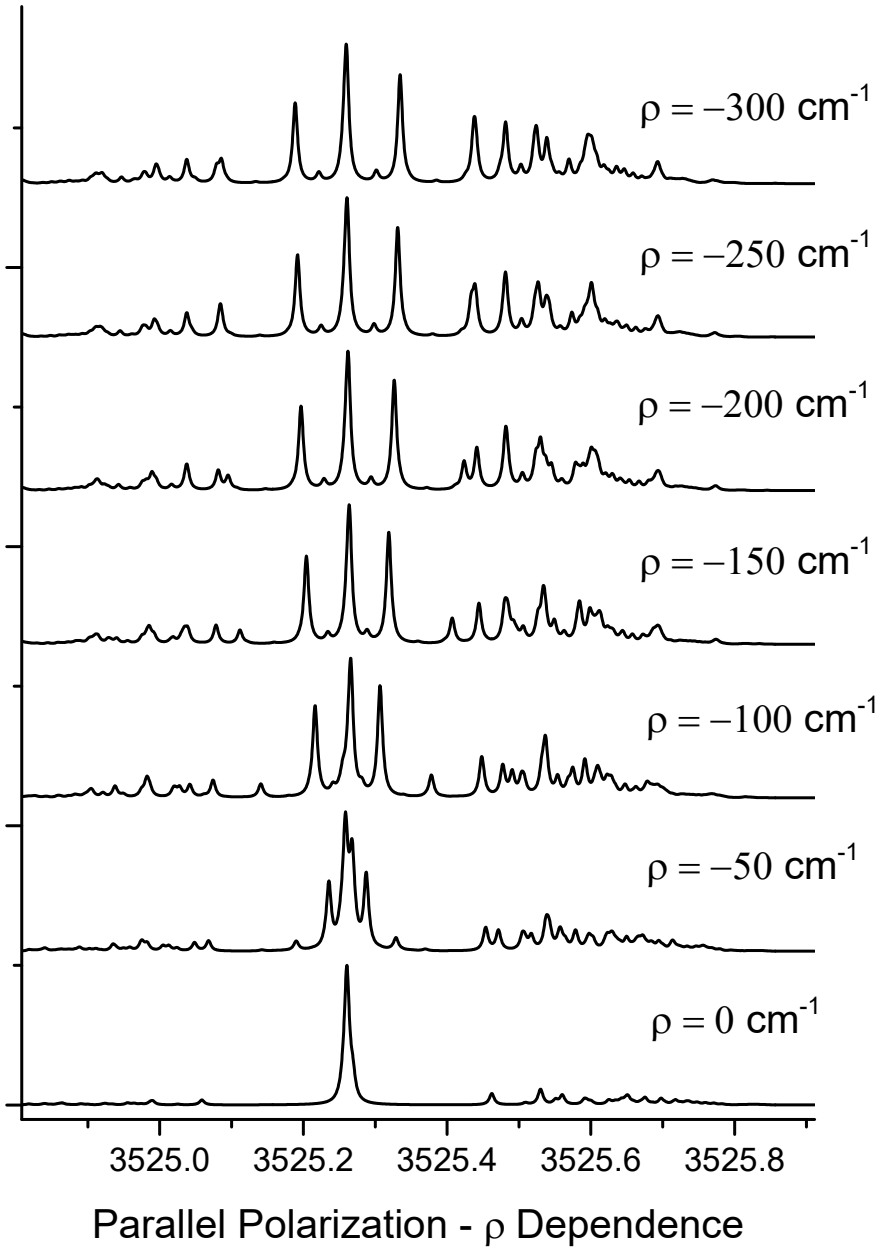

Figure 5.7: Simulation from Figure 5.6 recomputed using different values of the quenching parameter, ρ. The sensitivity of the rotational fine structure to the quenching parameter, especially that farthest from the band origin, largely motivates it as a sensitive probe of not only the electronic separation between low lying states, but also the extent to which they are coupled through the addition of the Zeeman interaction.

illustrates how sensitive the rotational substructure of the Zeeman spectrum is to the quenching of the orbital angular momentum. This strongly motivates the use of this parameter to achieve the best agreement between simulation and experiment.

The largest interactions of the Zeeman effect act through the dipolar interaction, which is a first rank tensor. The angular momentum quenching operator from Ref. 13 is reproduced in Eq. 5.26

$$\boldsymbol{H}_q = \frac{\rho}{\ell(\ell+1)}\left[T_2^2(\boldsymbol{L}) + T_{-2}^2(\boldsymbol{L})\right] \tag{5.26}$$

This second rank tensor formulation allows for the coupling between the two, low lying electronic states via the matrix element Kronecker delta term $\delta_{\lambda,-\lambda'}$. To couple these two electronic states would require a second rank Zeeman tensor. Such second-rank Zeeman terms would need to come from the magnetic susceptibility interaction.[1] These interactions are already very weak and unlikely to cause an interaction of this magnitude. Therefore, it is unlikely that improving the effective Hamiltonian in such a way will improve the theoretical results.

Although it was shown that the matrix elements in the linear case were accurate to the order of the experimental error, the matrix elements used to simulate the C_{2V} spectra are formulated using a modified parity conserving basis set. Without another system to corroborate the derived matrix elements, the accuracy of these elements cannot be confirmed. These matrix elements could be derived again in two alternate methods. In the first, one assumes the quenching is complete and "unquenches" the angular momentum, using the Hund's case (b) primitive basis as a starting point. While a good exercise to confirm that the derived matrix elements agree from both starting cases, it would require extensive re-derivation of the zero-field and quenching simulations in addition to the

Zeeman elements. The second, perhaps more straight-forward, approach involves using the primitive case (a) basis. Elements derived for the linear case could be easily extended into the C_{2V} framework. Once the appropriate primitive Hamiltonian was generated, it could be transformed into the parity conserving basis from Eq. 5.8 and used to simulate spectra. This method would provide a secondary check for the matrix elements without requiring extensive re-derivation. At this time, neither method has been attempted, though the latter of the suggested methods is the most promising. It seems prudent to note at this juncture, while the agreement simulated for this complex is qualitatively satisfying, both simulations generate extra features that are not present in the experimental spectra. It is unclear from what these simulated features derive, but it is expected these are extraneous features of the simulation and not a consequence of droplet effects such as those that have been seen for other molecules and complexes previously.[21-22]

Much like the unexpected behavior of the hydroxyl–acetylene complex, the hydroxyl radical exhibits inconsistent Zeeman splitting. In this case, the Zeeman interaction is ~21% stronger in helium droplets than when compared to gas phase predictions. As the OH–CO system confirmed the validity of the effective Hamiltonian and the variational treatment, we are left to speculate on the origin of the increased splitting. The Zeeman splitting could increase due to a reduction in the spin-orbit coupling constant, which would bring the two spin-orbit manifolds closer together increasing the interaction. However, this is in direct contrast to previous work,[12] which has found that in helium, the differing solvation effects lead to a larger separation of these states, increasing the overall spin-orbit coupling constant. Furthermore, it is well

accepted[1] that additional terms truncated from the current effective Hamiltonian are much smaller in magnitude than $\boldsymbol{B(L+S)}$, and we would not expect their addition to improve the agreement to more than an extra percent at best. It is in this anomalous result that we are completely without future direction. Likely, some possible manifestation of angular momentum in the helium bath is generating an additional magnetic effect which is expressed as an increase in the Zeeman interaction. However, postulating and identifying such interactions are well beyond the scope of this work.

5.6 Summary

The Zeeman spectra of three van der Waals complexes were collected *via* sequential capture and association along their respective ground vibronic surface in helium droplets. A variational treatment was developed to simulate and assign the features of the spectra. Due to the experimental linewidths, only terms involving the electron spin and orbital angular momentum interacting with the magnetic field were included in the effective Hamiltonian, as other terms such as rotational and nuclear spin angular momenta are much less intense.[1] The Zeeman effect in the OH–CO van der Waals complex confirmed the validity of the Hamiltonian treatment as well as the applicability of measuring such spectra within a superfluid helium bath. The Zeeman spectra were readily simulated without the need for adjustable parameters in the theoretical treatment. Furthermore, it confirmed the accuracy of the laboratory measurements of the magnetic field of the Zeeman cell, which were performed using a commercial Hall probe.

Zeeman spectra of the hydroxyl radical–acetylene complex were complicated by the quenching of orbital angular momentum upon complexation. Derivation of the matrix in a C_{2V} parity conserving basis led to extraneous simulated transitions that were not observed in the experimental spectra. Furthermore, simulations required the modification of zero-field parameters, unlike the OH-CO complex. The magnitude of quenching parameter, ρ, increased by approximately 25% upon application of the Zeeman field. A larger quenching parameter indicates a larger separation of the two low-lying electronic states in the Zeeman field relative to zero-field and even Stark field measurements. It is not inherently apparent what induces the increased separation, however, at this time we cannot eliminate the simulation as the origin in the discrepancy between Zeeman and zero-field parameters.

The Zeeman spectra of the hydroxyl radical in helium droplets presents another puzzling result. Zeeman splitting calculated in two different ways – through perturbation theory equations given in the literature[1] and a variational treatment – agree on the magnitude of the expected splitting. Experimental spectra show a splitting that is ~21% larger than simulations predict. Much like the unexpected behavior in the OH-C_2H_2 Zeeman spectra, there is very little that can be rationalized to compensate for such a large deviation. We leave this anomalous results as a call to the community at large to investigate and identify the potential causes of such interactions between the droplet environment and the dopants.

5.7 References

(1) Brown, J. M.; Carrington, A., *Rotational Spectroscopy of Diatomic Molecules*; Cambridge University Press: Cambridge, U.K. ; New York, 2003.

(2) Ramos, A. A.; Trujillo Bueno, J., Theory and Modeling of the Zeeman and Paschen-Back Effects in Molecular Lines. *Astrophys. J.* **2006**, *636*, 548-563.

(3) Berdyugina, S. V.; Solanki, S. K., The Molecular Zeeman Effect and Diagnostics of Solar and Stellar Magnetic Fields - I. Theoretical Spectral Patterns in the Zeeman Regime. *Astron. Astrophys.* **2002**, *385*, 701-715.

(4) Crutcher, R. M., Observation of Magnetic Fields in Molecular Clouds: Testing Star Formation Theory. In *Magnetic Fields in Diffuse Media*, Lazarian, A.; Pino, E. M. d. G. D.; Melioli, C., Eds. Springer-Verlag: Berlin, 2015; Vol. 407, pp 445-457.

(5) Rodgers, C. T.; Hore, P. J., Chemical Magnetoreception in Birds: The Radical Pair Mechanism. *Proc. Natl. Acad. Sci. U.S.A.* **2009**, *106*, 353-360.

(6) Thalau, P.; Ritz, T.; Burda, H.; Wegner, R. E.; Wiltschko, R., The Magnetic Compass Mechanisms of Birds and Rodents Are Based on Different Physical Principles. *J. R. Soc., Interface* **2006**, *3*, 583-587.

(7) Mack, K. M.; Muenter, J. S., Stark and Zeeman Properties of Ozone from Molecular-Beam Spectroscopy. *J. Chem. Phys.* **1977**, *66*, 5278-5283.

(8) Bowater, I. C.; Brown, J. M.; Carrington, A., Microwave Spectroscopy of Nonlinear Free-Radicals .1. General Theory and Application to Zeeman Effect in HCO. *Proc. R. Soc. London, Ser. A* **1973**, *333*, 265-288.

(9) Choi, M. Y.; Douberly, G. E.; Falconer, T. M.; Lewis, W. K.; Lindsay, C. M.; Merritt, J. M.; Stiles, P. L.; Miller, R. E., Infrared Spectroscopy of Helium Nanodroplets: Novel Methods for Physics and Chemistry. *Int. Rev. Phys. Chem.* **2006**, *25*, 15-75.

(10) Morrison, A. M.; Liang, T.; Douberly, G. E., Automation of an "Aculight" Continuous-Wave Optical Parametric Oscillator. *Rev. Sci. Instrum.* **2013**, *84*, 013102.

(11) Liang, T.; Flynn, S. D.; Morrison, A. M.; Douberly, G. E., Quantum Cascade Laser Spectroscopy and Photoinduced Chemistry of Al-$(CO)_n$ Clusters in Helium Nanodroplets. *J. Phys. Chem. A* **2011**, *115*, 7437-7447.

(12) Raston, P. L.; Liang, T.; Douberly, G. E., Anomalous Lambda-Doubling in the Infrared Spectrum of the Hydroxyl Radical in Helium Nanodroplets. *J. Phys. Chem. A* **2013**, *117*, 8103-8110.

(13) Douberly, G. E.; Raston, P. L.; Liang, T.; Marshall, M. D., Infrared Rovibrational Spectroscopy of OH-C_2H_2 in ^{4}He Nanodroplets: Parity Splitting Due to Partially Quenched Electronic Angular Momentum. *J. Chem. Phys.* **2015**, *142*, 134306.

(14) Moradi, C. P.; Douberly, G. E., On the Stark effect in open shell complexes exhibiting partially quenched electronic angular momentum: Infrared laser Stark spectroscopy of OH-C2H2, OH-C2H4, and OH-H2O. *J. Mol. Spectrosc.* **2015**, *314*, 54-62.

(15) Brice, J. T.; Liang, T.; Raston, P. L.; McCoy, A. B.; Douberly, G. E., Infrared Stark and Zeeman Spectroscopy of OH-CO: The Entrance Channel Complex along the OH + CO → *trans*-HOCO Reaction Pathway. *J. Chem. Phys.* **2016**, *145*, 10, 124310.

(16) Broderick, B. M.; McCaslin, L.; Moradi, C. P.; Stanton, J. F.; Douberly, G. E., Reactive Intermediates in ^{4}He Nanodroplets: Infrared Laser Stark Spectroscopy of Dihydroxycarbene. *J. Chem. Phys.* **2015**, *142*, 144309.

(17) Marshall, M. D.; Lester, M. I., Spectroscopic Implications of Partially Quenched Orbital Angular Momentum in the OH−Water Complex†. *J. Phys. Chem. B* **2005**, *109*, 8400-8406.

(18) Mohr, P. J.; Newell, D. B.; Taylor, B. N., CODATA Recommended Values of the Fundamental Physical Constants: 2014. *J. Phys. Chem. Ref. Data* **2016**, *45*.

(19) Marshall, M. D.; Lester, M. I., Spectroscopic implications of the coupling of unquenched angular momentum to rotation in OH-containing complexes. *J. Chem. Phys.* **2004**, *121*, 3019-3029.

(20) Brauer, C. S.; Sedo, G.; Dahlke, E.; Wu, S. H.; Grumstrup, E. M.; Leopold, K. R.; Marshall, M. D.; Leung, H. O.; Truhlar, D. G., Effects of ^{18}O Isotopic Substitution on the Rotational Spectra and Potential Splitting in the OH-OH_2 Complex: Improved Measurements for ^{16}OH-$^{16}OH_2$ and ^{18}OH-$^{18}OH_2$, New Measurements for the Mixed Isotopic Forms, and *ab Initio* Calculations of the ^{2}A' - ^{2}A" Energy Separation. *J. Chem. Phys.* **2008**, *129*, 104304.

(21) Morrison, A. M.; Raston, P. L.; Douberly, G. E., Rotational Dynamics of the Methyl Radical in Superfluid He-4 Nanodroplets. *J. Phys. Chem. A* **2013**, *117*, 11640-11647.

(22) Moradi, C. P.; Xie, C. J.; Kaufmann, M.; Guo, H.; Douberly, G. E., Two-Center Three-Electron Bonding in $ClNH_3$ Revealed *via* Helium Droplet Infrared Laser Stark Spectroscopy: Entrance Channel Complex along the Cl + NH_3 → $ClNH_2$ + H Reaction. *J. Chem. Phys.* **2016**, *144*, 8, 164301.

CHAPTER 6

CONCLUSION AND OUTLOOK

As demonstrated in the previous three chapters, helium nanodroplets are a versatile tool to interrogate fundamental molecular interactions. This dissertation has presented three investigations of the intermolecular interactions of van der Waals complexes formed from sequential doping in helium droplets. These studies employed the Stark and Zeeman effects to enhance understanding of these systems as well as droplet-dopant interactions.

Triplet atomic oxygen was generated through a commercial thermal catalytic cracker and successfully doped inside helium droplets. The association of $O(^3P)$ and HCN along the ground vibronic surface formed a weakly bound complex, which was interrogated via infrared Stark spectroscopy. The rotational substructure of a band centered at 3285 cm^{-1} is consistent with a linear O–HCN complex with a $^3\Sigma$ ground state. The observed complex demonstrates the feasibility of studying interactions of $O(^3P)$ with other unsaturated closed shell species. Furthermore, highly branched unsaturated alkenes have a submerged barrier to reaction, thus association with $O(^3P)$ could have interesting results. It is still somewhat unclear how quickly the helium bath is capable of removing translational energy from dopants, and thus it is within the realm of possibility that a highly saturated alkene could react even at 0.4 K.

The fate of the reaction between the hydroxyl radical and carbon monoxide was investigated within the cold environment of a helium droplet. It was expected that the barrier to reaction would be too high to proceed to products, and a stretching band near 3551 cm^{-1} confirms a complexation induced frequency shift of the hydroxyl stretch. The rotational constant of the complex in helium is consistent with a reduction relative to the gas phase value due to helium solvation increasing the inertia on the molecular axes. The complex exhibits a dipole moment, of 1.852 D, which is smaller than the equilibrium dipole moment calculated at the CCSD(T) /aug-cc-pVQZ level of theory. This experimental dipole is reduced as a consequence of large amplitude motion in the O-H-C bending angle, which accounts for 80% of the discrepancy when the motion is included in the theoretical calculation.

Molecular Zeeman spectroscopy was employed for the first time in helium droplets to clarify what role, if any, the helium bath has on the resulting spectra. It was predicted, based on Stark Spectroscopy in helium droplets, that the implementation would be facile and straight-forward. The Zeeman spectra for the OH-CO van der Waals complex was easily modeled using a rigid Hamiltonian with no fitting parameters. However, when moving to other systems, the Hamiltonian and variational treatment were insufficient to adequately model the interactions. These anomalous results were quite puzzling and most likely derive from a dopant-droplet effect that is not well understood. That is why we call the droplet community to start investigating these interactions so we can better understand the way in which this cryogenic matrix behaves.

The ability for Zeeman spectroscopy to extract information about the electronic states of a molecule offer a very enticing way of interrogating species inside helium

droplets. Cooled near absolute zero, the simplified spectra evolve within the magnetic field according to the electronic structure of the state being interrogated, which if modeled correctly, could allow for extraction of that information from the spectra. Future directions for such spectroscopic investigations could be the ethynyl radical or the methoxy radical. Both have very complicated low-lying excited states which will behave uniquely within the confines of a helium droplet. The information extracted can only serve to better understand the fundamental interactions and quantum mechanics behind chemistry.